`

A STUDY ON MICROSTRUCTURAL AND MECHANICAL PROPERTIES OF ALUMINIUM ALLOYS JOINT FABRICATED BY CMT WELDING PROCESS

THESIS

submitted to

DELHI TECHNOLOGICAL UNIVERSITY

For the award of the degree of

DOCTOR OF PHILOSOPHY

IN

MECHANICAL ENGINEERING

By

SATYAVEER SINGH

(2K18/Ph.D/ME/41)

Under the supervision of

Dr. N. Yuvaraj
(Department of Mechanical Engineering, DTU)

Prof. Reeta Wattal
(Department of Mechanical Engineering, DTU)

DEPARTMENT OF MECHANICAL ENGINEERING

DELHI TECHNOLOGICAL UNIVERSITY

(Formerly Delhi College of Engineering)

Main Bawana Road, Shahabad Daulatpur, Delhi - 110042, India

2025

`

CERTIFICATE

This is to certify that the thesis entitled "**A study on microstructural and mechanical properties of Aluminium alloys joint fabricated by CMT welding process**" submitted to the Delhi Technological University, Delhi -110042, is fulfillment of the requirements for the award of degree of Doctorate in Philosophy in Mechanical Engineering embodies the original research work carried out by **Mr. SATYAVEER SINGH**, Enrollment No: 2K18/Ph.D/ME/41 under my supervision. This work has not been submitted in part or full for any other degree or diploma of this or any other University.

DR. N. YUVARAJ
Department of Mechanical Engineering
Delhi Technological University, Delhi.

PROF. REETA WATTAL
Department of Mechanical Engineering
Delhi Technological University, Delhi.

`

DECLARATION

I certify that the work which is being presented in this thesis entitled "**A study on microstructural and mechanical properties of Aluminium alloys joint fabricated by CMT welding process**" in the partial fulfillment of requirement for the award of degree of Doctorate in Philosophy submitted in the Department of Mechanical Engineering at Delhi Technological University, is an authentic record of my own work carried out during a period from August 2018 to February 2025, under the supervision of **DR. N. YUVARAJ** and **PROF. REETA WATTAL**, Department of Mechanical Engineering, Delhi Technological University, Delhi. The matter presented in this thesis has not been submitted in any other University/Institute for the award of any degree or diploma.

(SATYAVEER SINGH)
Roll No: 2K18/Ph.D/ME/41

ACKNOWLEDGEMENT

I am greatly indebted to my supervisor **Dr. N. Yuvaraj** and **Prof. Reeta Wattal**, Department of Mechanical Engineering, Delhi Technological University, Delhi, for his invaluable guidance, constant inspiration, numerous suggestions and continued support throughout this research work. I am profoundly grateful to them with reverence for helping me with necessary information and equipment & materials as well.

With great humbleness, I sincerely thank **Prof. B.B. Arora,** Head, Mechanical, Production & Industrial, and Automobile Engineering, for his insightful comments and constant encouragement. SRC Committee members and faculty members of the Department of Mechanical Engineering, Delhi Technological University for their suggestions and support throughout the research work.

I would also like to thank with much appreciation the people whose help and support were a great asset: the technical staff at DTU, namely, Mr. Net Ram, Mr. Lalan Kumar Sinha, and Mr. Girish Anand, who provided great help for conducting the experiments and material characterization; Mr. Sandeep for their help in conducting the XRD studies; and Mr. Tek Chand for his help in revealing the microstructures.

Finally, I dedicate my work to my parents. My sincere thanks to my late father, Mr. Mahilal Singh, and my mother, Mrs. Rajvati Devi, for their support and blessings that greatly helped me carry out this research work.

SATYAVEER SINGH

ABSTRACT

The 2xxx series alloys are regarded as difficult to join because of softening due to precipitate dissolution, and their welding is challenging. Third-generation Al-Li-based alloys are preferred over traditional Al alloys due to their superior mechanical properties, including high toughness, stiffness, and specific strength, making them ideal for aircraft, automotive, and construction applications. This study explores optimizing welding parameters for AA2099-T86 alloy using Cold Metal Transfer (CMT) and Pulsed Metal Inert Gas (Pulse MIG) welding through CRITIC and ROV methods. Experiments with varying welding currents, speeds, and contact tip-to-workpiece distances focused on bead geometry, including weld penetration, dilution, and heat input. The L9 Taguchi orthogonal array identified optimal parameters, with CRITIC and ROV methods used to consolidate multiple responses. Optimal settings were $I_3S_3D_2$ for CMT and $I_1S_3D_2$ for pulse MIG. ANOVA assessed parameter impact on weld bead geometry, and confirmation tests validated the optimal settings. The study found welding current to be the most influential parameter, followed by welding speed and CTWD, for defect-free CMT welds.

Weld bead characteristics such as penetration (P), reinforcement (R), and width (W) were analyzed across various process parameters. Mechanical properties, including tensile strength and microhardness, were evaluated for different heat inputs. Microstructural analysis of the parent metal (PM), fusion line (FL), and weld metal (WM) was performed; with tensile fracture surfaces examined using FESEM and EDX. Using Taguchi L9 design, butt joints were created to optimize tensile strength and microhardness. ANOVA assessed the effects of process parameters, revealing that welding current was the most significant factor. The optimal parameters identified were a welding current of 180 A, a speed of 8 mm/sec, and a contact tip-to-workpiece distance of 4 mm, yielding a tensile strength of 302 MPa and microhardness of 118 HV. Modern industries

use ultrasonic vibration to enhance material flow and grain growth during welding processes. This study investigates the fabrication of CMT-welded joints from AA2099-T86 under various conditions, with current, travel speed, and contact tip-to-workpiece distance as variable parameters. Gas flow rate, ultrasonic frequency, and vibration amplitude were kept constant at 16 liters/min, 20 kHz, and 60 µm, respectively. Microstructural analysis of the welds was conducted using a field emission scanning electron microscope (FESEM). Butt joints were fabricated under three different environments, i.e., conventional (C-CMT), liquid nitrogen (LN-CMT), and ultrasonic vibration welding (U-CMT). Results revealed that ultrasonic vibration during CMT welding significantly improved ultimate tensile strength (UTS), reaching 252 MPa—a 10.52% increase over C-CMT and a 2.02% increase over LN-CMT. This improvement is attributed to the smaller grain size in the U-CMT sample (42.88 µm), compared to 53.48 µm for C-CMT and 47.71 µm for LN-CMT. Microhardness values were higher for U-CMT (115.96 HV) compared to C-CMT (106.14 HV) and LN-CMT (110.91 HV), with the base metal having a hardness of 106 HV. The increased microhardness in U-CMT is linked to finer precipitates and reduced grain size. U-CMT samples showed a 9.25% and 4.55% increase in microhardness over C-CMT and LN-CMT samples, respectively. The U-CMT joint displayed a columnar grain structure, while C-CMT joints had elongated grains. The use of liquid nitrogen cooling decreased the grain size to 47.71 µm, demonstrating its effectiveness in managing grain structure.

TABLE OF CONTENTS

LIST OF FIGURES

LIST OF TABLES

NOMENCLATURE

AA	Aluminium Association
ANOVA	Analysis of variance
ASTM	American Society for Testing Materials
BM	Base Metal
CMT	Cold Metal Transfer
N_2	Nitrogen
CO_2	Carbon Di-Oxide
CSC	Conventional Short Circuit
CTWD	Contact Tip To Workpiece Distance
DCEP	Direct Current Electrode Positive
DCEN	Direct Current Electrode Negative
DOE	Design of Experiments
EDM	Electrical Discharge Machine
EDS	Energy Dispersive Spectrometer
EDX	Energy Dispersive X-ray
EMF	Electromotive Force
FESEM	Field Emission Scanning Electron Microscope
FL	Fusion Line
FSW	Friction Stir Welding
FZ	Fusion Zone
GMAW	Gas Metal Arc Welding
GTAW	Gas Tungsten Arc Welding
HAZ	Heat Affected Zone
HR-XRD	High-Resolution X-ray Diffraction
IMC	Inter-Metallic Compounds
Mg	Magnesium
MIG	Metal Inert Gas
NDT	Non-Destructive Testing

`

OCV	Open Circuit Voltage
PCP	Peak Current Phase
PDC	Pulse Dynamic Correction
PWHT	Post Weld Heat Treatment
RSM	Response Surface Methodology
RT	Radiography Technique
SEM	Scanning Electron Microscope
SMAW	Shielded Metal Arc Welding
THI	Thermal Heat Input
TIG	Tungsten Inert Gas
U-CMT	Ultrasonic Assisted Cold Metal Transfer
UTM	Universal Testing Machine
VHN	Vickers Hardness Number
UTS	Ultimate Tensile Strength
XRD	X-Ray Diffraction
WM	Weld Metal

CHAPTER 1: INTRODUCTION

1.1 INTRODUCTION

In the manufacturing realm of diverse industrial sectors encompassing automotive, defense, aerospace, power generation, shipbuilding, construction, and chemical processing, among others, fusion welding processes prevail as the predominant method of joining materials. This technique, vital for the creation of intricate components and structures, involves the fusion of base metals at high temperatures, ensuring robust and durable bonds. A plethora of fusion welding methodologies, including gas metal arc welding (GMAW), gas tungsten arc welding (GTAW), and submerged arc welding (SAW), among others, are meticulously employed to seamlessly unite a broad spectrum of materials, ranging from ferrous to non-ferrous alloys, steels, and exotic metals, facilitating the production of complex industrial apparatus with precision and reliability [Satyanarayana et al., 2005].

Among the aforementioned welding methodologies, GMAW welding emerges as a versatile and adaptable process, extensively employed for the fusion of both ferrous and non-ferrous metals. Its versatility stems from its ability to facilitate superior weldments, characterized by enhanced structural integrity and mechanical properties. The GMAW method offers a comprehensive solution for welding a diverse array of materials, catering to the exacting demands of various industrial applications [Ibrahim et al., 2012]. GMAW technique initiated by an arc formed between a consumable electrode and the targeted metal. The consumable electrode, typically a solid wire, is perpetually fed and propelled through the arc, undergoing controlled droplet transfer into the molten pool, where it solidifies as deposited metal. Renowned for its exceptional metal deposition rate, GMAW stands as a quintessential choice for industrial-scale

manufacturing processes. Its intrinsic efficiency makes it a prime candidate for robotic welding applications, where precision and consistency are paramount [Chacon-Fernandez et al., 2005]. Short-circuit GMAW is commonly employed for efficiently welding thin steel sheets and for positional welding of thicker steel sections. Advances in power sources with modern inverter technology have improved control over the arc current waveform and dynamic wire feeding, effectively mitigating issues such as burn-through and distortion in sheet metal welding.

Cold Metal Transfer (CMT) represents an advancement in welding technology derived from the conventional short-circuiting transfer process inherent to GMAW. This innovative method originated from research conducted by 'Fronius of Austria' [Kumar et al., 2016; Evangeline et al., 2019]. The term "cold" in CMT indicates its unique characteristic of low heat input resulting from a very low non-zero current during the fusion welding process. Through the incorporation of a sophisticated wire feeding system alongside rapid digital monitoring capabilities, CMT facilitates a precisely controlled approach to material deposition while maintaining a low heat input [Pickin et al., 2011; Irizalp et al., 2016]. In CMT welding, approximately one-fourth of the total welding time occurs during a short-circuit phase, where the current magnitude nearly reaches zero. This substantial reduction in current usage leads to significant cost and energy savings, typically ranging from 30% to 40%. In contrast to traditional short-circuiting methods used in GMAW, CMT significantly manages the detachment of liquid droplets from the filler wire. While short-circuiting methods rely on Lorentz forces for droplet detachment, CMT uses wire retraction to achieve this. This distinctive technique allows CMT to weld thin sheets without causing deformation due to its remarkably low thermal heat input, which results from the minimal, non-zero current used [Kumar et al., 2018]. Unlike conventional arc welding methods, CMT operates at very low currents, where short circuits occur. Consequently, it demands

minimal heat input and generates no spatter. Its suitability for joining thin sheets, plates, and materials stems from its characteristic of lower heat volume [Meena et al., 2018]. **Figure 1.1** illustrates the cycle of the current-voltage waveform in CMT. This cycle comprises three distinct phases:

1. **Peak current phase:** This phase initiates with a surge in current, triggered by arc ignition, which heats the electrode wire, leading to droplet formation. Throughout this phase, the arc voltage remains steady.
2. **Background current phase:** Following the peak current phase, there is a transition to a lower current level. The droplet formed during the peak current phase remains at the electrode tip, hindering globular transfer due to the minimized current. Consequently, spattering formation is significantly reduced, resulting in improved bead aesthetics. This phase, characterized by a non-zero current level, ensures minimal heat input, thereby preventing distortion even during the welding of thin sheets. It is typically longer and persists until the onset of the next short-circuiting step.
3. **Short-circuiting phase:** During the short-circuiting phase, which follows the background time phase, the arc voltage diminishes to zero. This prompts the electrode wire to make direct contact with the molten weld pool, resulting in a short circuit. Simultaneously, the digital process control mechanism initiates a reverse force on the electrode wire via its return signal. This action facilitates the transfer of metal from the wire in droplet form to the molten pool, facilitated by the fracture of the liquid bridge. Consequently, the wire retracts, signaling the initiation of the subsequent cycle.

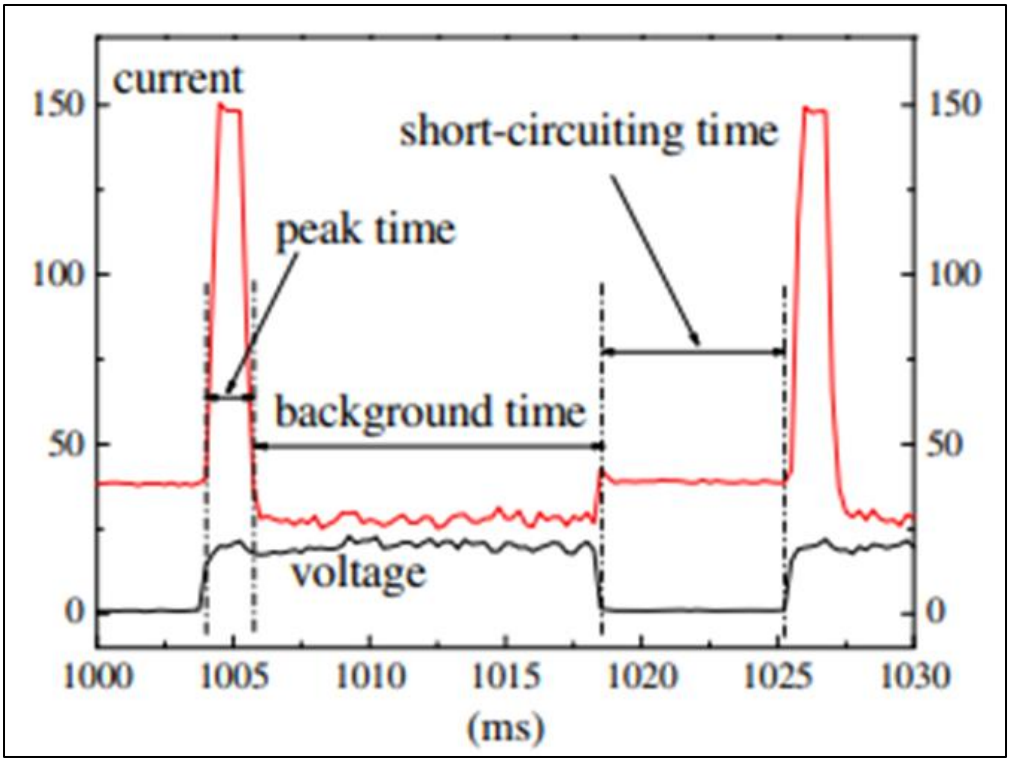

Figure 1.1 Waveform of current and voltage of CMT process [Feng et al., 2009]

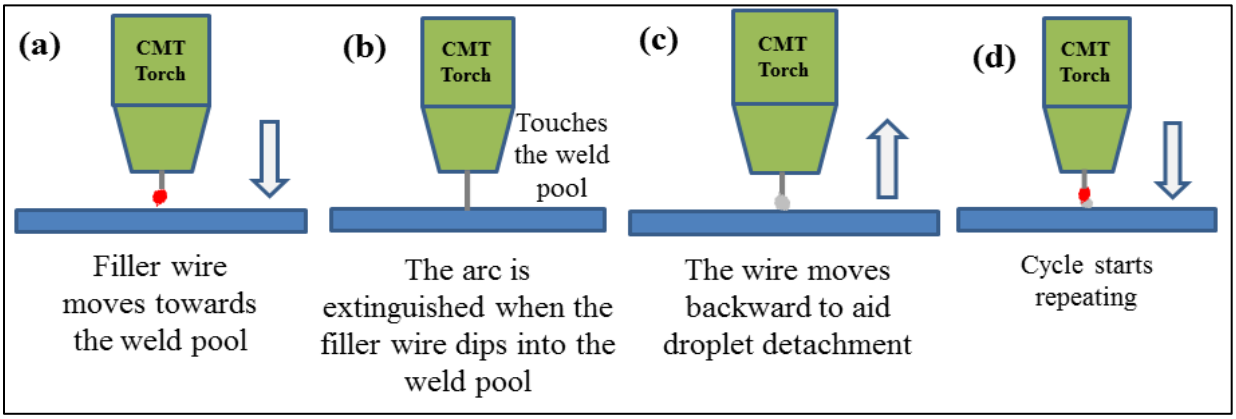

Figure 1. 2 Demonstration of CMT welding arc

CMT functions as a dynamic process, alternating between hot and cold phases. At the start, during the arcing phase, the electrode filler approaches the molten pool (**Figure 1.2 (a)**), initiating the hot phase as the arc is established (**Figure 1.2 (b)**). Following this, the filler wire immerses into the molten pool while the arc retracts completely, transitioning into the cold phase, where the welding current drops substantially to a near-zero level. As the wire retracts in a

reverse motion, it forms a droplet, which is detached during the short circuit mode at a lower current (**Figure 1.2 (c)**), constituting another cold phase. Finally, the wire motion reverses again through a digital mechanism, initiating the process anew (**Figure 1.2(d)**), thus reverting to the hot phase.

1.2 MOTIVATION

Currently, recent developments in welding techniques are supplanting traditional methods in advanced engineering and industrial settings. Among these advancements, CMT, an evolved form of GMAW welding, has gained global acceptance due to its superior bead aesthetics, minimal spatter production, and notably reduced heat input. These attributes distinguish CMT and render it uniquely suited for a variety of applications. Aluminium alloys have found extensive application in the aerospace sector since the 1920s, gradually displacing wood in various aircraft components [Prasad et al., 2013; Ma et al., 2015]. Auto manufacturers have increasingly adopted aluminium alloys for fabricating various vehicle components and bodies, following their widespread use in the aerospace industry.

Over the past few decades, there has been a steady rise in the utilization of these alloys, with high-end vehicles now incorporating them to replace steel and iron in up to 90% of applications. The appeal of aluminium alloys lies in their lightweight nature, resistance to corrosion, and remarkable thermal and electrical conductivity, surpassing traditional iron-based alloys in performance [De Sousa Araujo et al., 2018; Alexopoulos et al., 2016]. These qualities, coupled with the ability of certain alloys to be initially shaped in a soft state and then undergo heat treatment to achieve strength akin to structural steel, render them highly sought-after materials. Recent studies have investigated 3rd generation Al-Cu-Li alloys, such as AA2099-T86, as

potential replacements for AA2024 alloy in aerospace applications due to their excellent mechanical properties [Warner et al., 2006].

To begin with, lithium stands out as one of the lightest metallic elements, boasting an exceptionally low density of 534 kg/m³. When combined with aluminium, which has a density of 2700 kg/m³, lithium effectively reduces the overall density of the resulting alloy. Adding 1 wt. % of lithium to aluminum results in a density reduction of about 3%, which is approximately 80 kg/m³. Moreover, lithium uniquely enhances the elastic modulus of aluminium by nearly 6% per 1% of lithium added, distinguishing it as the sole metal capable of such a significant increase [Buchheit et al., 1994; Prasad et al., 2003].

For better efficiency, manufacturers these days are more interested in using lightweight materials that not only reduce the overall weight of the structure but also enable the use of the latest technology. Al-Li alloys find widespread application in the manufacturing of lightweight metal components across various industries, including automotive and aerospace, due to their commendable mechanical characteristics and superb weldability. lightweight metal components across various industries, including automotive and aerospace, due to their commendable mechanical characteristics and superb weldability.

Traditionally, in various industrial sectors, aluminium alloys have been predominantly joined using the fusion welding method, particularly GMAW. In GMAW, an electric arc is established between a consumable electrode and the workpiece, providing the higher heat input required to melt both the workpieces and the filler material. However, this process often involves significant heat input, which can compromise joint strength and result in pore formation within the welds. To address these issues, the CMT process employs a low-heat input technique, ensuring the creation of robust welded joints.

1.3 OVERVIEW OF THE THESIS

Chapter 1 introduces the Cold Metal Transfer (CMT) technique and examines why it is being adopted as an alternative to the GMAW method.

Chapter 2 encompasses a comprehensive review of literature concerning cold metal transfer (CMT), as well as its variants such as ultrasonic vibration-assisted CMT (U-CMT) and liquid nitrogen CMT (LN-CMT). This section critically evaluates the findings of researchers regarding the application of these processes in joining different materials while also identifying existing research gaps. Additionally, the chapter outlines the research objectives and presents a flow diagram detailing the experimental methodology.

Chapter 3 delves into the intricacies of the Cold Metal Transfer (CMT) mechanism, materials methodologies, and experimentation. It elaborates on the setup developed for bead-on-plate butt joining of 2099-T86 aluminum alloys using various techniques, such as ultrasonic-assisted CMT (U-CMT) and liquid nitrogen assisted CMT (LN-CMT). This section meticulously explores the working principles of CMT welding and delves into the advancements involving the integration of ultrasonic vibrations during the welding process. Furthermore, it provides detailed insights into the experimental input parameters and procedures employed in welding. Additionally, it furnishes information concerning the microstructure, microhardness, and tensile testing conducted as part of the experimentation. The chapter also covered the various machines used in the experiments, providing detailed descriptions. The procedures for determining mechanical properties, including tensile and microhardness tests, were discussed. Metallurgical characterization methods, such as microstructure analysis, phase analysis, and elemental composition using field emission scanning electron microscopy, optical microscopy, and X-ray diffraction, were illustrated.

Chapter 4 provides a comprehensive overview of the results obtained from the beads-on-plate experiments. The experimentation involves utilizing AA2099-T86 as the base plate for conducting bead-on-plate trials. Detailed discussions are presented on the impact of various process parameters on factors such as dilution, heat input, and penetration. Bead-on-plate experiments were conducted separately using pulsed metal inert gas welding and CMT processes on age-hardened aerospace aluminum alloy AA2099-T86 plates. To determine the optimal input parameter settings, the L9 orthogonal array of Taguchi's approach was employed. The combined use of the "Criteria Importance through Inter Criteria Correlation (CRITIC)" and "Range of Value" methods facilitated the derivation of a single index for multiple responses. The optimal parameters were identified, and confirmation tests were conducted to validate the findings.

Chapter 5 This chapter examines the CMT butt joining of AA2099-T86 alloy with uniform thickness across various welding input parameters. It discusses weld bead dimensions, including reinforcement, width, and penetration. Key input parameters selected for evaluating mechanical properties were welding current, speed, and contact tip-to-work distance, optimized using the Taguchi L9 method. The chapter also features microstructural analysis and compares butt joints fabricated under three environmental conditions: conventional, liquid nitrogen, and ultrasonic vibration welding. Results showed that joints created in the ultrasonic vibration environment displayed enhanced mechanical properties and notable grain refinement.

Chapter 6 presents the conclusions derived from this research, highlights the key contributions, and discusses potential directions for future studies.

1.4 SUMMARY

This chapter provides a concise overview of joining AA2099-T86 alloys using CMT welding techniques. It examines both the advantages and limitations of the GMAW welding process. Furthermore, the chapter delves into the mechanism of CMT welding and highlights the benefits it offers over traditional GMAW processes, along with its practical applications. Additionally, it outlines the rationale behind adopting CMT as a replacement for GMAW. Lastly, the thesis outlines its organizational structure.

CHAPTER 2 : LITERATURE REVIEW

2.1 INTRODUCTION

This chapter reviews the literature on cold metal transfer (CMT) and its variants of various materials. It identifies research gaps and objectives based on the review and outlines a plan for fabricating the welded joints. The discussion of the literature review is organized as follows:

- CMT welding of aluminium alloys
- CMT welding of dissimilar materials
- Ultrasonic vibration-assisted CMT welding

2.2 COLD METAL TRANSFER WELDING (CMT)

2.2.1 CMT welding of aluminium alloys

Pinto et al. (2006) studied the microstructure and residual stress in CMT, pulse MIG, and laser-hybrid welds of AlMg3 welded joints and found similar microstructure across all welding techniques. It was found that all three welding methods created microstructures with dendrites and more precipitates between the dendrites. This made the weld seams harder than the base material. Residual stresses were found to be compressive in the weld seam and tensile in the parent material due to pretensioning during clamping. CMT welds displayed slightly lower residual stresses than MIG welds, particularly on the underside, due to the reduced heat input of the CMT process.

Wilhelm et al. (2010) examined the arc dynamics during the high-current phase of CMT welding utilizing various welding gases. They discovered that CO2 gas effectively cools the arc in the outer region and can create a pronounced temperature gradient. In contrast, argon and mixtures

with a high molar fraction of argon exhibit considerably lower specific heat across the entire temperature range, leading to less efficient cooling of the arc edge.

Gungor et al. (2014) studied the mechanical properties of robotic CMT-welded 5083-H111 and 6082-T651 aluminum alloys. They reported that CMT's minimal heat input and elevated wire melting rate, in contrast to the pulsed MIG technique, enabled a fast welding speed (400 mm/min) and minimal distortion. Microhardness results across weldments were similar, with hardness drops close to the base metal.

Babu et al. (2015) compared the microstructure and mechanical properties of fusion (GTAW) and solid-state (FSW) welded AA5059 aluminum alloy joints. Their findings indicated that while both FSW and GTAW joints had lower tensile strength compared to the base metal, FSW joints had slightly higher tensile strength than GTAW joints. The FSW joints contained fine, equiaxed grains due to dynamic recrystallization, while the weld zone of GTAW joints had a dendritic structure caused by rapid heating and cooling from the welding arc.

Dutra et al. (2015) analyzed the metallurgical characteristics of 5083-H116 aluminum alloy welded with the CMT process using two filler wires (5183 and 5087). The 5087 filler wire enhanced the weld quality, exhibiting superior mechanical performance in tensile tests compared to the 5183 filler wire. Microhardness tests showed comparable properties between the welding metal and the HAZ. While visual inspection and scanning electron microscopy (SEM) revealed a higher number of pores with the 5183 filler wire

Cornacchia et al. (2017) investigated the microstructural and mechanical properties, such as hardness and tensile strength, of welded joints made from 6005A-T6 aluminum using CMT, LASER-MIG, and fiber LASER-MIG techniques. They utilized SEM and EDS to conduct

fractographic studies after welding. Their results indicated that both CMT and fiber laser-MIG hybrid joints of AA6005 aluminum alloy had superior mechanical properties compared to those made with MIG welding. Although all three techniques produced similar microstructures with dendritic structures, the fiber laser-MIG hybrid joint displayed epitaxial growth from partially melted grains and columnar-dendritic grains, likely due to dynamic recrystallization during the welding process.

Afolalu et al. (2019) compared the performance of TIG, MIG, and friction stir welding on aluminum and steel alloy weld joints. They discovered that factors such as gas flow rate, welding speed, and welding current were essential for achieving accurate and consistent welds. The selection of these parameters was influenced by the type of material, desired strength, and specifications of the welding equipment. The study emphasized how various welding techniques affected the durability of welded joints, observing that higher process temperatures reduced tensile stress but led to increased diffusion of particles into the central region of the weld.

Yin et al. (2019) used deep learning to predict weld formation in 5083 aluminum alloy using twin-wire CMT welding. They found that the accuracy of predictions was primarily determined by the number of neurons in hidden layers, the number of training iterations, and the learning rate, with optimal settings for these parameters identified. The deep neural network exhibited excellent learning and generalization capabilities, greatly enhancing the comprehension of how welding parameters relate quantitatively to the microstructure, strength, and toughness of welded joints. The predicted values for weld penetration, width, and reinforcement closely matched the experimental values, showing excellent fitting and generalization.

Cornacchia et al. (2020) analyzed the welding of EN AW 6181/6082-T6 and EN AC 42100-T6 aluminum alloys for structural applications using MIG, CMT, and Fiber Laser-MIG Hybrid

techniques. They identified common aluminum welding defects, including porosity and incomplete penetration, particularly in frame welds. Cracks were noted exclusively in frame joints and were probably caused by difficulties in heat dissipation associated with thicker and more complex geometries. The fiber laser joint showed higher-quality macrostructures. The fusion zone, partially melted zone, and HAZ microstructures were similar across all joints, with welding seams featuring fine dendrites. Hardness tests indicated that partially melted zones and HAZ had better mechanical properties with innovative techniques due to less microstructural change compared to MIG welding.

Huan et al. (2020) examined the impact of wire composition on the microstructure and mechanical properties of 6063 aluminum alloy welded with hybrid synchronous pulse CMT-process using ER4047 and ER5183 wires. Their study revealed that the molten pool's thermal conductivity was higher in the ER4047 joint, resulting in increased porosity. The cooling speed and surface tension differences led to larger pore sizes and wider fusion zones in the ER4047 joint. Microstructural analysis showed finer grain sizes in the ER4047 weld, with distinct eutectic compositions affecting mechanical properties. Ultimately, the ER4047 joint demonstrated significantly lower tensile strength compared to the ER5183 joint.

Koli et al. (2020) developed a multi-response mathematical model to predict the weld bead geometry of AA6061-T6 using response surface methodology. They found that higher current and lower welding speeds resulted in deeper penetration and higher dilution with increased heat input. CMT exhibited higher dilution and penetration with reduced heat input compared to both MIG pulse synergic and standard MIG welding, and it also demonstrated higher consistency. The optimal settings were found to be 92.518 A and 7.50 mm/s for CMT, 109.418 A and 10.873 mm/s for MIG pulse, and 110.847 A and 11.527 mm/s for standard MIG, with desirability

indices of 61.11%, 68.80%, and 72.6%, respectively. The predicted results closely aligned with the actual outcomes, confirming the accuracy of the regression model. Effective joint efficiency is achieved through good penetration and dilution with minimal heat input.

Pramod et al. (2020) studied CMT welding of aluminum alloy 6061-T6 using ER 4043, focusing on optimizing welding parameters for a 3.5-mm thick pressure vessel. Their findings confirmed defect-free joints through radiographic testing, achieving a joint efficiency of 66.61% and a microhardness of 59.78 HV. They noted grain coarsening in the HAZ due to thermal gradients and a reduction in mechanical properties from the loss of strengthening elements like Si and Mg. X-ray diffraction revealed the presence of Al-Si and Fe-Si intermetallic compounds in the welding zone, while fractography indicated ductile failure in the tensile samples.

Chen et al. (2024) investigated the effects of different shielding gases on the CMT welding of 5083 aluminum alloy using ER5356 wire. They observed that, despite significantly reducing porosity, increasing the amount of helium in the shielding gas enhanced weld penetration and width. The tensile strength of the deposited metal increased from 220 MPa to 270 MPa, representing a 22.7% improvement, and exhibited a typical ductile fracture. Hardness also rose from 64.2 HV to 68.4 HV. Microhardness measurements were highest at the weld center, decreased in the heat-affected zone, and were lowest in the base material zone. The peak hardness of 68.4 HV was achieved with 100% helium, compared to the lowest hardness of 64.2 HV with 100% argon. As per findings by Hwang et al. (2001), when welding aluminum, the vaporization of alloys within the weld pool can lead to the depletion of alloy elements, with magnesium commonly evaporating from the upper region of the pool. Consequently, the presence of magnesium for precipitation reactions within the molten pool tends to be minimal,

despite the ample availability of silicon, which is several times higher in the filler wire compared to the base metal.

Escribano Garcia et al. (2022) utilized the Response Surface Methodology technique (RSM) combined with the finite element method for studying the temperature variations and distortions during CMT welding of steel sheets. The RSM optimization technique is more reliable and faster than traditional trial-and-error procedures. De Paula et al. (2022) reported that academic and corporate persons might explore the CRITIC-MOORA-3N method to find the best alternatives. Akram et al. (2024) found that the CRITIC-REGIME methodology enables efficient criteria selection and supports the selection of the best possible decision alternatives. Kumari et al. (2022) employed the CRITIC-CODAS multicriteria decision-making method to find the best machining technique for the machining of titanium alloy.

Khan et al. (2022) utilized Taguchi's entropy-based ROV method to optimize the heat and fluid flow conditions. Khan et al., (2023) employed the Taguchi-CRITIC-WASPAS multicriteria decision-making method for finding the effect of the input parameters on the thermal and hydrodynamic performance of the nanofluids inside a vertical annulus. Lee et al. (2023) reported that the ROV-RL method is beneficial in solving problems related to economic and environmental metrics.

Prajapati et al. (2020) reported that the gray relation with fuzzy interface technique is an effective method for finding the optimum parameters for multiple responses of HAZ, depth of penetration, bead width, and regulated metal deposition of MIG welding of low alloy steel. Vinoth et al. (2021) fabricated TIG welding of 3mm 316 stainless sheets using Taguchi-based grey relational analysis to find the optimum process parameters for combined maximum tensile strength and impact strength and minimum corrosion rate responses. Similarly, the Grey-based

Taguchi methodology was used for process parameter optimization on MIG welding of 316 SS by Ghosh et al. (2016) and MIG welding of AISI 1018 steel by Kumar et al. (2018). Saeheaw (2022) introduced the CRITIC-GRA multicriteria decision-making technique to provide the best optimal from six input parameters to achieve simultaneous higher weld strength and lower weld width of laser welded blanks. The summary of CMT welding of aluminium alloys is exhibitted in Table 2.1.

Table 2.1 Major conclusions on CMT welding of Aluminium alloys

Researcher Name	**Material Investigated & Filler wire diameter**	**Shielding Gas & Flow rate**	**Welding Parameters**	**Prominent Results**
Gungor et al., (2014)	AA5083-H111 (6 mm thick), AA6082-T651 (6 mm thick), ER 5183 (1.2 mm dia.)	Pure argon (15 L/min)	Current (194 ± 5 A), Voltage (19.5 ± 1 V), Welding speed (0.4 m/min), Wire feed speed (11 ± 0.2 m/min)	The CMT process, characterized by its very low thermal heat input and higher wire melting coefficient compared to pulsed MIG welding, achieved at a welding speed of 400 mm/min with minimal distortion on the welded plates. The welding efficiency was 65% for AA5083 and 62% for AA6082 alloy.

A. Elrefaey, (2015)	AA7075-T6 (6 mm thick), AA7075-T6 (6 mm thick), ER 5356 (1.2 mm dia.)	Pure argon (15 L/min)	Current (93 A), Voltage (15.1 V), Welding speed (15 mm/sec), Wire feed speed (5.5 m/min), Heat input (84.2 J/mm)	The CMT welding process produces joints with superior mechanical properties compared to conventional MIG processes. The joint had mechanical property coefficients of 77%, 60% and 69% for yield strength, ultimate tensile strength and elongation, respectively. CMT welding yielded flawless 7075-T6 joints, completely free from spatter, cracks, and with minimal porosity.
Xie et al., (2018)	Al5.5Zn2.5Mg2.2Cu aluminium alloy plate (3 mm thick), Al5.5Zn2.5Mg2.2Cu aluminium alloy plate (3 mm thick), ER 4043	Argon (15 L/min)	Current (95 A), Voltage (14.5 V), Welding speed (7 mm/sec), Wire feed speed (5.5 m/min), Arc length correction	The mechanical properties of the welded joint depend on the microstructure and weld metal composition. The weld zone has the lowest microhardness (96 HV) and tensile strength (340 MPa) due to coarsely equiaxed grains and particles. In the HAZ, coarsened precipitates and a wider precipitate-free zone reduce hardness (135 HV), yield strength, and tensile strength (505 MPa), but increase elongation (16.8%) compared to the base metal.

	(1.2 mm dia.)		(25%)	
Wang et al., (2019)	AA2198-T8 (2 mm thick), AA2198-T8 (2 mm thick), ER 4043 (1.2 mm dia.)	Argon (20 L/min)	Current (85 A), Pulse current (30 A), Welding speed (70 cm/min)	Increasing the current frequency with reduced electrical conductivity, resulting in a shorter distance for sustaining the arc from the wire tip to the base metal. As the pulse current frequencies rose from 20 to 50 kHz, droplet diameter decreased and droplet length increased. The pinch effect became more pronounced at higher pulse current frequencies because the current density through the droplet increased over time. Within the range of 60 to 80 kHz, both the arc diameter and droplet length stayed within an ideal range.
Koli et al., (2019)	AA6061-T6 (3.18 mm thick), AA6061-T6 (3.18 mm thick), ER 4043	Argon (15 L/min)	Current (80-120 A), Welding speed (7.5-13.5 mm/sec), CTWD (10	CMT has lower penetration than MIG pulse synergic and MIG manual at the same current and welding speeds, making it ideal for thin sheets. Proper penetration and dilution with low heat input are crucial for optimal joint efficiency. High heat input and rapid cooling create

	(1.2 mm dia.)		mm)	residual stresses, causing surface cracks on the bead and reducing joint strength.
Comez et al., (2020)	AA5754 (2 mm thick), AA7075 (6 mm thick), ER 5356 (1.2 mm dia.)	Argon (15 L/min)	Current (87-120 A), Voltage (11.6-14.6 V), Heat input (94.61-108.99 J/mm), Welding speed (0.5-1 mm/s)	As heat input increased, the corrosion rate decreased due to the overaging of AA7075 base metal, which had a beneficial effect against corrosion. Additionally, pore formation was noted in the HAZ of the AA7075 alloy as a result of zinc vaporization.
Girinath et al., (2020)	AA5052 (6 mm thick), AA5052 (6 mm thick), ER 4043 (1.2 mm dia.)	Argon (15 L/min)	Current (70-110 A), Welding speed (600-1200 mm/min), Drag angle (10 & 90^0), Push angle (10^0)	The orientation of the torch relative to the welding direction has a considerable effect on the microstructure, tensile strength, bending properties, hardness, and formability of 2 mm AA5052 blanks welded using the CMT process. Without arc pre-heating, the tensile strength of the welded blank achieved with a push angle is about 92.85% of that of the base metal.

Pramod et al., (2020)	AA6061-T6 (3.5 mm thick), AA6061-T6 (3.5 mm thick), ER 4043 (1.2 mm dia.)	Argon (15 L/min)	Current (110 A), Voltage (19.4 V), Welding speed (7.5 mm/s), Wire feed speed (4.9 m/min)	The weld joint efficiency was 66.6% for with reinforcement and 75.58% for without reinforcement tensile specimens. The weld metal had lower tensile strength and elongation than the base metal. Without reinforcement, tensile specimens fractured in the weld zone, while with reinforcement, specimens fractured in the base metal.
S.T. Selvamani, (2021)	AA 6061-T6 (3 mm thick), AA6061-T6 (3 mm thick), ER 4043 (1.2 mm dia.)		Current (100 A), Voltage (13.9 V), Arc length correction (1.4 mm), Wire feed speed (0.35 m/min)	CMT-welded AA6061-T6 alloy joints exhibit transgranular crack propagation under varying heat input (170-260 J/mm) conditions. Metallographic analysis of the welded joints revealed a distinctive dendritic structure in the fusion zone and improved grain boundaries, indicating excellent integrity and enhanced metallurgical properties. The cracking mechanism is identified as anodic with transgranular crack propagation.

Chen et al., (2022)	2A12 Al alloy plate (8 mm thick), 2A12 Al alloy plate (8 mm thick), ER2319 (1.2 mm dia.)	Argon (15 L/min)	Current (145-165 A), Voltage (10.2-15.8 V), Welding speed (2-8 mm/s), Heat input (884.875-1303.5 J/mm)	The microstructure in the front weld seam was finer compared to the back weld seam, attributed to the effects of the secondary thermal cycle. Additionally, the microstructure size in the weld joint increased with higher heat input. The base metal had a tensile strength of 300 MPa and 16% elongation. The welded joint's strength coefficient is approximately 70%, and it exhibited a ductile fracture mode.
Wang et al., (2022)	AA 6063-T6 (3 mm thick), AA 6063-T6 (3 mm thick), ER 4047 (1.2 mm dia.)	Argon (15 L/min)	Welding speeds (55-75 cm/min), Wire feeding speed (5.2 m/min)	As welding speed increases, weld porosity rises sharply from 0.1% to 3.9%, with large pores (341.1 μm) forming. At welding speeds of 65 and 55 cm/min, pore sizes are about 87.8 μm and 20.6 μm, respectively. The primary factor influencing the mechanical properties of the welded joints is the softening of the HAZ.
Shanker et al., (2023)	AA7475-T7351 (3 mm thick),	Pure argon (13.8	Current (95-80 A), Voltage	The base metal is the hardest at 170 HV, significantly higher than the weld metal and HAZ. The weld metal has the lowest

	AA7475-T7351 (3 mm thick) ER 4043 (1 mm dia.)	L/min) for GMAW, (15 L/min)	(18.9-19.1 V), Welding speed (3.08-4.06 mm/s), Wire feed speed (3.9-4.5 m/min)	hardness in both CMT and GMAW samples. CMT samples show slightly better hardness in the weld metal and HAZ compared to GMAW samples. CMT samples demonstrated superior yield strength, tensile strength, and elongation values compared to GMAW samples.
Chen et al., (2024)	AA5083-H111 (10 mm thick), AA5083-H111 (20 mm thick), ER5356 (1.2 mm dia.)	100%Ar, 75% Ar +25% He, 50% Ar +50% He, 100% He, (20 L/min)	Current (185 A), Voltage (22 V), Welding speed (8.5 mm/s), Wire feed speed (10 m/min)	Increasing the helium in the shielding gas enhanced weld penetration and width, reduced porosity, refined the microstructure from coarse dendrites to fine equiaxed crystals, and improved tensile strength from 220 MPa to 270 MPa (22.7% increase). The tensile fracture exhibited a quintessential ductile fracture, and hardness increased from 64.2 HV to 68.4 HV.
Nagasai et al., (2024)	AA6061 (3 mm thick), AA6061 (3 mm thick), ER4043	Argon (15 L/min)	Welding speed (280 mm/min), Wire feed speed (4700	The tensile strength (TS) and weld metal hardness values of dissimilar Al/Mg connections produced with a wire feed speed of 4700 mm/min, a welding speed of 280 mm/min, and an arc length correction

	(1.2 mm dia.)		mm/min), Bevel angle (60°)	of 10% showed higher values, measuring 33 MPa and 95.8 HV, respectively.

2.2.2 CMT welding of dissimilar materials

Shanglu Yang et al. (2013) performed the CMT of aluminum alloy to zinc coated steel. It was observed that the presence of erratic zinc-vapor generated during the cold metal transfer welding resulted in an unstable welding process as it interacted with the arc and the molten filler wire. It was observed that keeping a predetermined gap allowed zinc vapor to escape from the weld zone, which helped stabilize the welding process.

Kang & Kim (2015) employed both Al-Si alloy and Al-Mg alloy filler wires to join Al5052 alloy with hot-dip aluminized (Al-coated) steel sheets using the CMT method. They found that the silicon (Si) composition in the filler metal played a significant role in determining the thickness of the intermetallic compound (Imc) layer. When using Al-Si filler wires such as ER 4043 and ER 4047, the thickness of the Imc layer was generally uniform along the interface, ranging from 2μm to 3μm. In contrast, with Al-Mg filler wires like Al 5356 and 5183, the Imc layer thickness varied, being thickest at the center of the interface and tapering off towards the ends (root and toe). Researchers found it challenging to control the IMC layer formation with Al-Mg filler wires and noted that increasing the silicon content in the filler wire led to a reduction in the IMC layer thickness.

Cao et al. (2013) utilized three distinct aluminum wires—4043, 4047, and 5356—as filler materials to weld 6061 aluminum alloy with galvanized mild steel (Q235) through the CMT welding technique. The strength of the resulting welds was found to hinge upon two primary

factors: the thickness of the intermetallic layer, which is regulated to approximately 5µm (which falls below the critical value of 10µm), and the softening of the aluminum at HAZ. The failures typically start at the Al side HAZ rather than at the weld-brazed interface. The hardness of the aluminium side HAZ was lower compared to the base metal, suggesting that shrinkage mainly occurred in the aluminum HAZ during loading, which weakened the joint. Therefore, reducing heat input could narrow the width of the aluminum HAZ and improve joint strength. Among the process parameters, the type of wire was found to be the most significant, contributing 48.92% to the overall effect, while welding speed, wire feed speed, and their interaction accounted for 13.13%, 19.35%, and 23.82%, respectively.

Babu et al. (2019) worked on the joining of AA 2219 and austenitic stainless steel by using the CMT welding method with AA4047 filler wire, and they found that as the thickness of the aluminum coating increased from 0.3 to 1.2 mm, the thickness of the intermetallic layer decreased significantly from 5 µm to 400 nm. This reduction in intermetallic layer thickness proved beneficial in addressing the challenge of inadequate wetting of liquid aluminum on stainless steel during CMT welding.

Lin et al. (2013) demonstrated the impact of varying the thickness of a low-carbon steel substrate on the shear strength of joints. When joining 0.7 mm thick low-carbon steel with aluminum using ER4043 filler material, a lower shear strength of 2.1 kN was observed, with failure occurring at the interface. In contrast, CMT braze lap joints with 1.2 mm thick low-carbon steel demonstrated higher shear strength, exceeding 2.5 kN, and failure happened along the fusion line. Similarly, CMT braze lap joints between AA6061 and high-strength DP600 also exhibited shear strengths greater than 2.5 kN, with failures occurring along the fusion line.

Wang et al. (2017) utilized Variable Polarity Cold Metal Transfer (VP-CMT) to join AZ31B magnesium alloy and 6061 aluminum alloys using ER4043 filler wire. The VP-CMT process involved two distinct cycles: electrode positive cold metal transfer (EP-CMT) and electrode negative cold metal transfer (EN-CMT), each divided into three phases, namely pre-conditioning phase (PCP), stabilization and control phase (SCP), and ase condition phase (BCP), similar to the conventional CMT process. Polarity was reversed at the start of the SCP phase to maintain stable welding conditions. During the EP-CMT cycle, current and voltage were around 97.3 A and 13.2 V, respectively, which were notably higher compared to the EN-CMT cycle, where current and voltage were 62.8 A and 8.9 V. Although the EN-CMT cycle used a lower current, material deposition remained steady because the negative electrode was employed to generate maximum heat in the arc, effectively melting the wire. According to a comparative analysis conducted by Shang et al. (2012), it was determined that brittle fracture occurred within the Fusion Zone on the magnesium side, where the micro-hardness reached its peak. This brittle fracture was attributed to the presence of a substantial quantity of Cu2Mg intermetallic compounds.

Madhavan et al. (2017) employed Al-5% Si filler metal for welding AZ31B Mg and AA6061 using CMT welding. It was observed that the tensile strength reached its maximum value of 360 MPa at the highest heat input (205 J/mm). This implies that with higher heat input, tensile strength improves, which can be attributed to increased travel speeds. High travel speeds resulted in minimal HAZ creation. The Fusion Zone thickness was found to be directly proportional to heat input, increasing from 3 to 12 μm as heat input rose from 175 to 205 J/mm, significantly impacting the joint strength. The fusion zone near the magnesium showed the highest microhardness due to the diffusion of alloying elements, the formation of intermetallic compounds, and the presence of precipitates such as Mg_2Si and Al_6Mn. At a heat input of 185

J/mm, the formation of coarser dendrites and the coarsening of precipitates led to reduced microhardness in the fusion zone.

Slower welding speeds resulted in lower cooling rates, producing coarser dendrites. Since cooling rate is directly related to welding speed, reduced speeds resulted in slower cooling. A slight increase in microhardness at the weld zone was noted due to the solubility of alloying elements. At a heat input of 205 J/mm, higher micro-hardness was observed at both the fusion zone and the weld zone due to the increase in travel speed that allowed for quicker solidification of the weld bead. Cao et al. (2013) conducted CMT welding to magnesium AZ31B with AA6061-T6, employing E4047 as a filler wire. Their results suggest that the presence of substantial amounts of magnesium-rich intermetallic compounds, such as β-Al_3Mg_2 and γ-$Al_{12}Mg_{17}$, in the weld joint may reduce the overall strength of the welded joint.

In their study, Jing et al. (2013) utilized ER4043/AlSi5 as a filler wire for butt joint welding. They found that the microhardness on both sides of the substrates was approximately similar, measuring around 55.06 HV on the magnesium side and 35.69 HV on the aluminum side. Within the Fusion Zone of the Mg side, micro-hardness sharply increased to its peak value of 242.7 HV. On the other hand, the microhardness inside the weld zone decreased from the magnesium side toward the aluminum side due to a reduction in intermetallic compounds. This decrease happened because, while magnesium and aluminum are highly soluble in each other when molten, the solidification process causes a eutectic reaction that forms hard and brittle precipitates like γ($Mg_{17}Al_{12}$) and β(Mg_2Al_3).

Huan et al. (2023) employed ER4043 filler wire in the fabrication process of a joint between AA6061-T2 and Ti-Ni-Hf alloy using CMT welding. Their results show that with an increase in heat input, the thickness of the intermetallic compound also increases, leading to a reduction in

joint strength. The peak tensile strength observed was 122 MPa at a heat input of 553.6 J/mm. It was noted that the phase transition temperature slightly increased with the distance from the interface. Additionally, as the heat input rose from 553.6 to 648.0 J/mm, the tensile strength of the joint dropped from 122 MPa to 84 MPa. As a result, the joint strength was found to be 32% of the strength of the base aluminum alloy. Sun et al. (2017) utilized a hybrid CMT welding-brazing technique employing ER4043 filler metal to join pure titanium TA2 to AA6061-T6. They found that the electromotive force (EMF) affects the wettability and flow behavior of the filler wire on the Al-Ti surface, differing from traditional metal joints. This joint demonstrated greater reliability than conventional welding techniques due to an expanded bonding area and a lower wetting angle. Without EMF, there was a significant drop in microhardness from the Al substrate metal to the heat-affected zone (HAZ), which remained relatively stable through to the weld zone (WZ). In contrast, with EMF applied, microhardness consistently decreased from the Al substrate metal to the WZ. Additionally, the microhardness of both the WZ and HAZ increased with EMF application, unlike in traditional welding methods. This phenomenon is attributed to the influence of the magnetic field on the weld structure.

Cao et al. (2014) employed Mg AZ61 wire in the brazing process of titanium alloy and magnesium alloy using CMT. By optimizing welding parameters, they achieved higher tensile loads of 2.10 kN and 1.83 kN for the Mg-Ti and Ti-Mg joints, respectively. In the Mg-Ti joint, magnesium is the base material and titanium is the filler wire, while in the Ti-Mg joint, titanium serves as the base material and magnesium is the filler. The microhardness of the titanium sheet measured around 175 HV, while that of the Mg weld metal stood at about 55 HV. Interestingly, the brazing interface layer exhibited the highest micro-hardness value, reaching 212 HV.

Li et al. (2017) conducted a study examining the impact of wire feed speed on the weld appearance and tensile strength of joints between Al and Ti as well as between Ti and Al, fabricated through the cold metal transfer welding process using ER4043 filler wire. Their research revealed that the optimal joint strength for Al-Ti joints could reach 305.5 MPa, surpassing that of Ti-Al joints, which reached 168.2 MPa. Additionally, they observed that Al-Ti joints typically fractured within the weld metal with a plastic fracture mode, whereas Ti-Al joints tended to fracture at the joining interface. The major conclusions on CMT welding of dissimilar materials are exhibited in **Table 2.2**.

Table 2.2 Major conclusions on CMT welding of dissimilar materials

Researcher Name	**Material Investigated & Filler wire diameter**	**Shielding Gas & Flow rate**	**Welding Parameters**	**Prominent Results**
Shanglu Yang et al., (2013)	AA6061-T6 (2 mm thick), Zinc coated low carbon steel (1.2 mm thick), ER4043 (1.2 mm dia.)	Pure argon (16 L/min)	Torch angle (60^0), Travel speed (5 mm/min)	The presence of erratic zinc vapor generated during the CMT welding resulted in unstable welding as it interacted with the arc and the molten filler wire. Any decrease in weld strength caused by softening in the HAZ may be countered by applying a suitable post-weld heat treatment.

Lin et al., (2013)	AA6061 (2 mm thick), Low carbon steel (0.7 mm-1.2 mm thick), ER4043 (1.2 mm dia.)		Current (70 A), Voltage (11.5 V), Welding speed (0.7 m/min)	With an increase in steel sheet thickness and strength grade, CMT brazed joints become stronger due to improved heat dissipation.
Kang & Kim, (2015)	AA5052 (1 mm thick), Al-coated steel (1.2 mm thick), ER4043, ER4047, ER5356, ER5183 (1.2 mm dia.)	Argon (15 L/min)	Current (76 A), Voltage (12.3-12.5 V), Welding speed (0.5 m/min), Wire feeding speed (4.2-4.8 m/min)	Silicon (Si) composition in the filler metal played a significant role in determining the thickness of the Intermetallic Compound (Imc) layer. Using aluminum-plated steel led to a thinner Imc layer than that formed with galvanized steel. This is due to the Fex(AlSi)y IMC layer created during hot-dip aluminizing, which served as a barrier to reaction and diffusion between the brazed welds and the steel base material.

Cao et al., (2013)	AA6061, AA7075, & AA5183 (1 mm thick), Galvanized mild steel (1 mm thick), ER4043, ER4047, & ER5356, (1.2 mm dia.)	Argon (15 L/min)	Voltage (12–14V), Welding speed (6–8 mm/s), Wire feed speed (4-6 m/min), Heat input (100–200 J/mm)	The strength of CMT weld-brazed joints between 1.0 mm AA6061-T6 and 1.0 mm galvanized mild steel is influenced by the thickness of the intermetallic layer and the softening of the heat-affected zone in the aluminum. The type of wire is the most critical factor, accounting for 48.92% of the influence. This is followed by the interaction between wire-feed speed and welding speed, which contributes 23.82%, wire-feed speed alone at 19.35%, and welding speed at 13.13%.
Babu et al., (2019)	AA2219-T87 (3 mm thick), Stainless steel (3 mm thick), ER4047 (1.2	Argon (15 L/min)	Voltage (12.3-12.5 V), Current (70 A), Welding	The strategy of initially joining aluminum and stainless steel via friction surfacing followed by CMT welding, works well for joining incompatible metals.

	mm dia.)		speed (0.4 m/min),	Thicker aluminum coatings, ranging from 0.3 mm to 1.2 mm, led to a reduction in the thickness of the intermetallic layer, decreasing it from 5µm to 400 nm. This reduction proved beneficial in addressing the issue of inadequate wetting of liquid aluminum on stainless steel during CMT welding.
Wang et al., (2017)	AA6061 (2 mm thick), Mg alloy AZ31B (2 mm thick), AZ31 (1.2 mm dia.)	Pure argon (18 L/min)	Welding speed (10 mm/s), Wire feed speed (6.5 m/min), Groove angle (90^0)	The welded joint had a lower tensile strength of 38.4 MPa, primarily influenced by the weakest of the intermediate layers. The brittle fracture mainly took place in the thinnest Mg2Al3 layer next to the 6061 substrate, likely due to its high brittleness, rapid cooling rate, and low peak temperature.

Shang et al., (2012)	AA6061 (3 mm thick), Mg alloy AZ31B (3 mm thick), Pure copper (HS201) (1.2 mm dia.)		Current (114 - 134 A), Voltage (11.1 -12.4 V), Welding speed (0.45 - 0.66 m/min), Wire feed speed (5.1 - 5.9 m/min)	The joint achieved a bonding strength of 34.7 MPa, with failure occurring in the fusion zone on the Mg side, which exhibited the higher micro-hardness. The fracture displayed a brittle characteristic, attributed to the presence of a continuous distribution of Cu_2Mg intermetallic compounds within the fusion zone.
Madhavan et al., (2017)	AA6061-T6 (2 mm thick), Mg alloy AZ31B (3 mm thick), Al-5 %Si (1.2 mm dia.)	99.9% Pure argon (18 L/min),	Current (70 - 100 A), Voltage (12.2 -12.9 V), Welding speed (235-305 mm/min).	Higher welding speeds resulting from higher heat inputs enhanced tensile strength and reduced the heat-affected zone (HAZ).

Jing et al., (2013)	AA6061-T6 (3 mm thick), Mg alloy AZ31B (3 mm thick), ER4043 (1.2 mm dia.)		Current (77 A), Voltage (12.3 V), Welding speed (0.5 m/min), Wire feed speed (4.3 mm/s)	The micro-hardness profile decreases from the magnesium side to the aluminum side, and this drop in hardness is due to the presence of Mg_2Al_3 and $Mg_{17}Al_{12}$ intermetallic compounds, which contributes to the brittle fracture observed in the fusion zone on the magnesium side of the joint.
Huan et al., (2023)	AA6061-T2 (3 mm thick), Ti-Ni-Hf (4 mm thick), ER4043 (1.2 mm dia.)	Argon (15 L/min)	Current (80 - 90 A), Voltage (17.3 -18 V), Welding speed (150 mm/min), Heat input (553.6-648 J/mm)	As the heat input rose from 553.6 J/mm to 648.0 J/mm, the ultimate tensile strength of the joint reduced from 122 MPa to 84 MPa. The strength of the joint represents 32% of that of the AA6061-T2. Fracture initiation occurred at the interface between the thicker IMC and Ti-Ni-Hf in the upper region, followed by propagation along this interface.

Sun et al., (2017)	AA6061-T6 (2 mm thick), Pure Titanium TA2 (1 mm thick), ER4043 (1.2 mm dia.)	Argon (15 L/min)	Welding speed (0.6 m/min), Frequency (0-10 Hz)	Application of the external axial magnetic field resulted in grain refinement, a reduction in Al-Ti intermetallic compounds, and increased microhardness in both the HAZ and the weld zone. Because of the instability in the

2.3 ULTRASONIC VIBRATION-ASSISTED CMT WELDING (U-CMT)

Ultrasonic vibrations offer significant advantages in welding and various manufacturing processes; they improve material flow and homogeneous grain growth, leading to improved mechanical properties. The use of ultrasonic-assisted welding to improve the homogeneity between the filler material and the substrate and refine the grain structure of welded materials has drawn more attention recently. Tian et al., (2018) applied an ultrasonic peening system to the aluminum alloy workpiece with CMT welding, resulting in grain refinement and reduced porosity in the welded joints. Fattahi et al., (2020) explored the GMAW welding of aluminum alloy, incorporating nanoparticles and applying ultrasonic vibrations beneath the workpiece. Their findings revealed notable improvements in the mechanical properties of the welded joints.

In their review, Kumar et al., (2017) provided an overview of the applications of ultrasonic vibration in GMAW and GTAW. They highlighted that the mechanical energy from high-frequency vibrations can aid in the fusion welding process by converting into heat. According to Chen et al. (2016), the application of ultrasonic vibration on the workpiece surface, positioned 11

cm away from the weld joint line, stimulated heterogeneous nucleation within the weld zone. Furthermore, it induced a transformation of columnar grains around the fusion zone into equiaxed grains during gas tungsten arc welding of Al-Li alloy. CMT technology has the potential to yield high-quality weld bead shapes through the meticulous adjustment of process parameters. Various factors within the CMT process notably influence the size and shape of weld beads. Specifically, the welding current and welding speed play significant roles in determining bead width and dilution, while welding speed and gas flow rate notably influence bead height [Meena et al. (2024)].

Koli et al. (2021) studied the impact of ultrasonic vibration on the weld quality of dissimilar aluminum alloy joints using CMT welding. They noted that the application of ultrasonic vibrations led to larger weld bead dimensions while maintaining consistent welding parameters. Additionally, it enhanced tensile strength and microhardness and produced finer grain structures in comparison to samples welded without the use of ultrasonic vibrations.

Wang et al. (2024) found that ultrasonic vibration during laser welding of Beta Titanium Alloy refined the weld grains into fine, equiaxed grains, enhancing uniformity and reducing average grain size. At 20 μm amplitude, the weld's tensile strength increased by 907 MPa and elongation improved by 1.8 times, shifting the fracture location to the heat-affected zone. Ultrasonic vibration did not affect the phase composition.

In their review, Kumar et al., (2024) provided an overview of the applications of ultrasonic vibration in welding and metal processing. They highlighted that the mechanical energy from high-frequency vibrations can aid in the fusion welding process by converting into heat. Dai (2003) highlighted that ultrasonic vibration serves to refine grains and also enhances weld depth.

Xia et al. (2024) found that ultrasonic vibration during gas tungsten arc welding of Inconel 690 enhances penetration and weldability by refining grains from 145.6 µm to 60.4 µm and transforming large columnar grains into smaller ones. This reduces crack sensitivity in the welds. The major conclusions on the ultrasonic vibration-assisted welding process are exhibitted in Table 2.3.

Table 2.3 Major conclusions on ultrasonic vibration-assisted welding process (U-CMT)

Researcher Name	**Material Investigated**	**Welding type (Ultrasonic-vibration assisted)**	**Ultrasonic operating Parameters**	**Prominent Results**
Tian et al., (2018)	Al 6061-T6 and ER4043 filler wire	CMT	UV Frequency (20 kHz) Amplitude (35 µm)	Applying ultrasonic vibrations during the CMT welding process enhances weld depth and reinforcement while decreasing the contact angle. Ultrasonic vibration also improves the hardness and wear resistance of the welded joints.
Zhao et al.,	Ti-6Al-4V alloy	CMT	UV	Tensile characteristics are

(2020)	and Ti-6Al-4V alloy filler wire		Frequency (20 kHz) Amplitude (100 ± 5 μm)	improved by ultrasonic vibration in the molten pool, which prevents columnar crystal formation. Grain orientation is impacted, but phase composition is unaltered. Mixed ductile/brittle fracture mode was seen in tensile specimens that fractured in the weld zone.
Ilman et al., (2022)	Al 6061-T6 and ER5356 filler wire	MIG welding	UV Frequency (100 Hz, 300 Hz and 500 Hz) Amplitude (81 μm, 4 μm and 4 μm)	Introducing mechanical vibration during the welding of AA6061-T6 aluminum alloy improves the weld metal microstructure, resulting in a more equiaxed dendritic grain structure. Optimal grain refinement occurs at a vibration frequency of 300 Hz.
Kuang et al.,	Al 2219 and	Pulse MIG	UV	Integrating ultra-high

(2022)	ER2319 filler wire	welding	Frequency (10-100 kHz)	frequency pulse (UFP) current with traditional pulsed MIG enhances welded joint strength and ductility. Reduced welding porosity, refined grains, and minimized Cu element segregation in the eutectic contribute significantly to improved tensile properties in UFP-MIG joints.
He et al., (2023)	FeCrNiCoMnSi0.1 alloy	TIG welding	UV Frequency (40 kHz) Amplitude (10 μm)	The ultrasonic process refines coating grains, breaks large columnar grains into smaller irregular equiaxed ones. Higher frequencies boost cavitation and agitation, refining grain size by 74%. This enhances mechanical properties, corrosion resistance, and structural strength through sensitization.

Zhang et al., (2023)	6061-T6 aluminum alloy AZ31B magnesium alloy	Friction stir welding	UV Frequency (20 kHz) Amplitude (6 μm)	Additional ultrasonic vibration (UV) has a limited effect on the overall heat because it balances the increased plastic deformation heat in the shear layer with reduced heat at the interface. The improved material flow caused by UV enhances the movement of material around the tool and promotes better mixing of magnesium and aluminium.
Wang et al., (2024)	Beta titanium alloy	Laser welding	UV Frequency (28 kHz) Amplitude (0, 10 μm, 20 μm, and 25 μm)	Ultrasonic vibration reduces the grain size in the weld, diminishes {200} direction weaving in beta titanium alloy, and increases dislocation density. This improvement raises the tensile strength of the welded joint by 907 MPa compared to the base material and increases elongation by a factor of 1.8 relative to laser-

				welded joints without assistance, resulting in fractures shifting from the weld center to the HAZ.
Xia et al., (2024)	Inconel 690 alloy	TIG welding	UV Frequency (35 kHz) Amplitude (29 μm)	Ultrasonic vibration during TIG welding of Inconel 690 enhances penetration and weldability by refining grains from 145.6 to 60.4 μm and transforming large columnar grains into smaller ones. This reduces crack sensitivity in the welds.
Guo et al., (2024)	Titanium Ti6Al4V alloy	Laser welding	UV Frequency (0 to 40 kHz) Amplitude (29 μm)	Ultrasonic vibration improved tensile strength and impact toughness, with the best performance at 0.2A showing ductile fracture. Excessive ultrasonics led to brittle fractures and uneven grain size.

Xiang et al., (2024)	AA2195-T6	Friction stir welding	UV Frequency (20 kHz) Amplitude (40 μm)	Ultrasonic vibration in FSW improves recrystallization and hardness in AA2195 joints, and increases elongation compared to standard FSW.

2.4 RESEARCH GAPS

It is clear from the above literature studies that:

- Literature reviews reveal that significant research has been conducted on welding aluminum alloys and other alloys using gas metal arc welding (GMAW) and various other welding techniques. Limited work has been studied for Al alloys used for light weight applications using the CMT process, so there is a need to investigate further in this area.
- While some researchers have examined the impact of factors such as workpiece material, filler metal composition, welding parameters, and shielding gases at various flow rates on bead geometry, microstructure, and mechanical properties. Less work has been exported on the combined effects of these different parameters.
- Aluminium alloys have not been welded using the standard CMT welding process under different environmental conditions.
- The literature review indicates that research focusing on industrial applications has been relatively limited.

2.5 RESEARCH OBJECTIVES

1. To study the mechanical and microstructural properties of Aluminium alloy joints produced by the CMT welding process for light-weight applications.
2. To study weld on bead geometry of the joint fabricated by standard CMT and pulse MIG.
3. To optimize CMT process parameters to obtain a sound welded joint.
4. To study and compare various mechanical properties of welded joints fabricated under different environmental conditions.

FLOW CHART FOR PRESENT WORK

The flow chart provides a summary of the detailed work. Figure 2.1 illustrates the flow chart for this project, outlining the step-by-step procedure and methodology used.

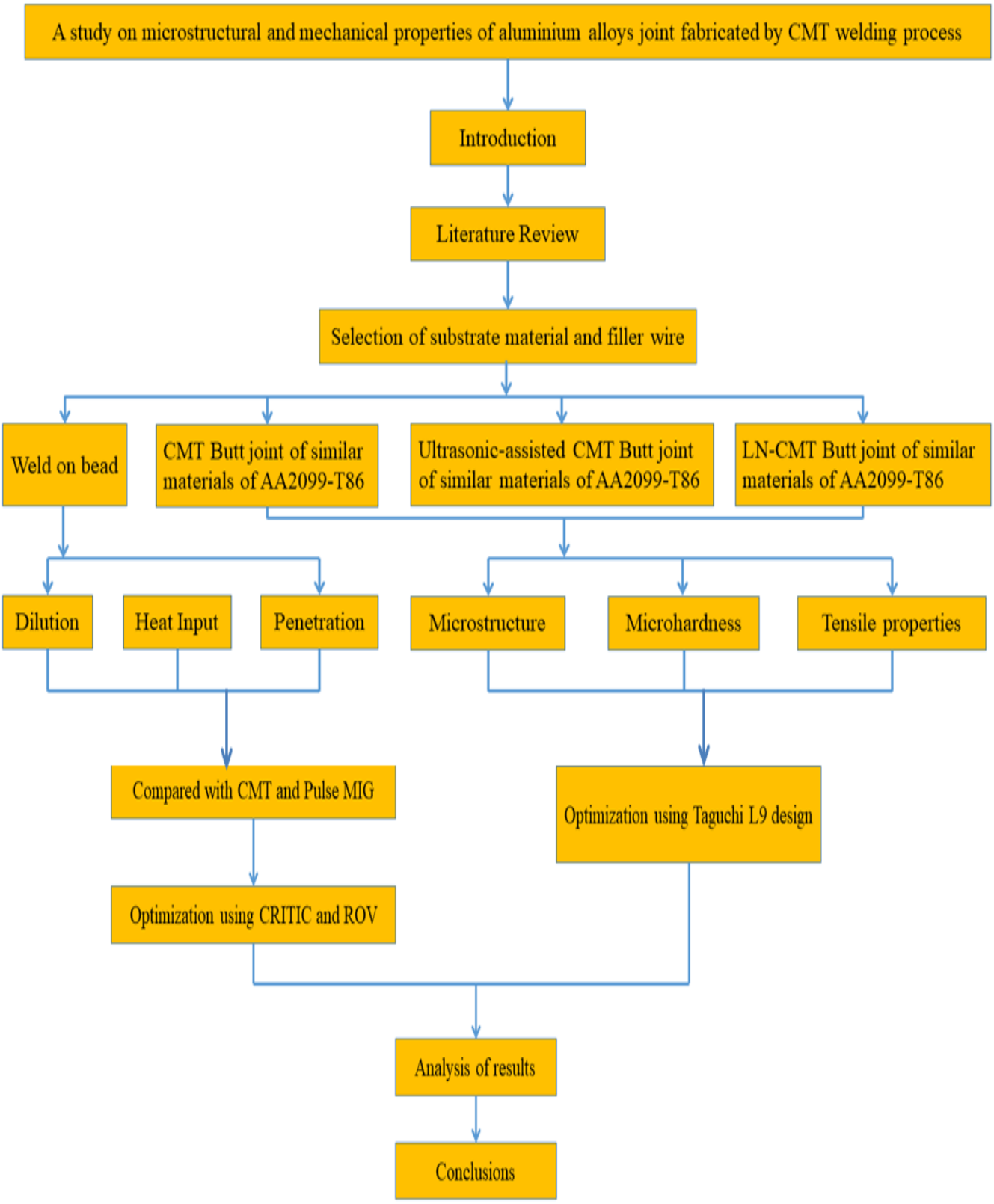

Figure 2.1 Flow chart of present research work

2.7 SUMMARY

This chapter provides an in-depth review of joining similar and dissimilar materials or alloys using CMT welding, focusing on welding parameters. It highlights key conclusions for joining dissimilar materials and aluminum alloys with the CMT process. Various CMT methods, process parameters, and combinations of welding materials and filler wires, along with mechanical and microstructural studies by numerous researchers, are discussed. The research gaps and objectives have been defined, and a flow chart outlining the existing work is provided. The key findings of this study are as follows:

- During the short-circuiting phase, the retraction of the filler wire plays a critical role in reducing stress, which contributes to the production of high-quality welded joints.
- Optimal process parameters depend on the base material, filler metals, environmental conditions, and shielding gases.
- Heat input is affected by the wire feed rate, welding current, and welding speed. Increasing the wire feed rate and welding current while reducing the travel speed raises the heat input, whereas the opposite adjustments lower it.
- Ultrasonic vibration assistance during welding enhances the strength properties of the weld.

CHAPTER 3: EXPERIMENTAL SETUP & PROCEDURE

3.1 MATERIAL SELECTION

3.1.1 Base material and filler material

AA2099-T86 plate, measuring 100 mm x 60 mm x 5 mm, serves as the base material. A 1.2 mm-diameter ER 4047 filler wire is used for the weld on the bead and joining process. This filler wire is compatible with 2XXX aluminium alloys. Chen, D. et al. 2021; Chen, X. et al. 2019; Han, B. et al. 2017. Table 3.1 presents the chemical compositions (by weight percentage) of both the AA2099-T86 base material and the ER 4047 filler wire. Figures 3.1(a) and (b) present detailed optical microscope images of the substrate material. In Figure 3.1(c), the tensile properties of the substrate material are illustrated, showcasing a tensile strength of 316.8 MPa and an overall elongation of 14.9%. Vickers microhardness testing further reveals that the average microhardness of the substrate material is 106 HV.

Table 3.1 Chemical composition (wt.%) of AA2099-T86 and filler wire

Elements details	Al	Si	Cu	Mg	Li	Ti	Zn	Fe	Mn
AA2099-T86	94.3	0.04	2.96	0.27	1.75	0.04	0.87	0.05	0.34
ER4047 filler wire	Bal.	12	0.3	0.1	-	0.14	0.2	0.8	0.15

Table 3.2 Mechanical properties of base material (AA2099-T86)

Mechanical properties	TS (MPa)	YS (MPa)	Elongation (%)	Microhardness (HV)
AA2099-T86	316.8	301.6	14.9	106
TS-Tensile strength; YS-Yield strength; HV-Vicker's microhardness				

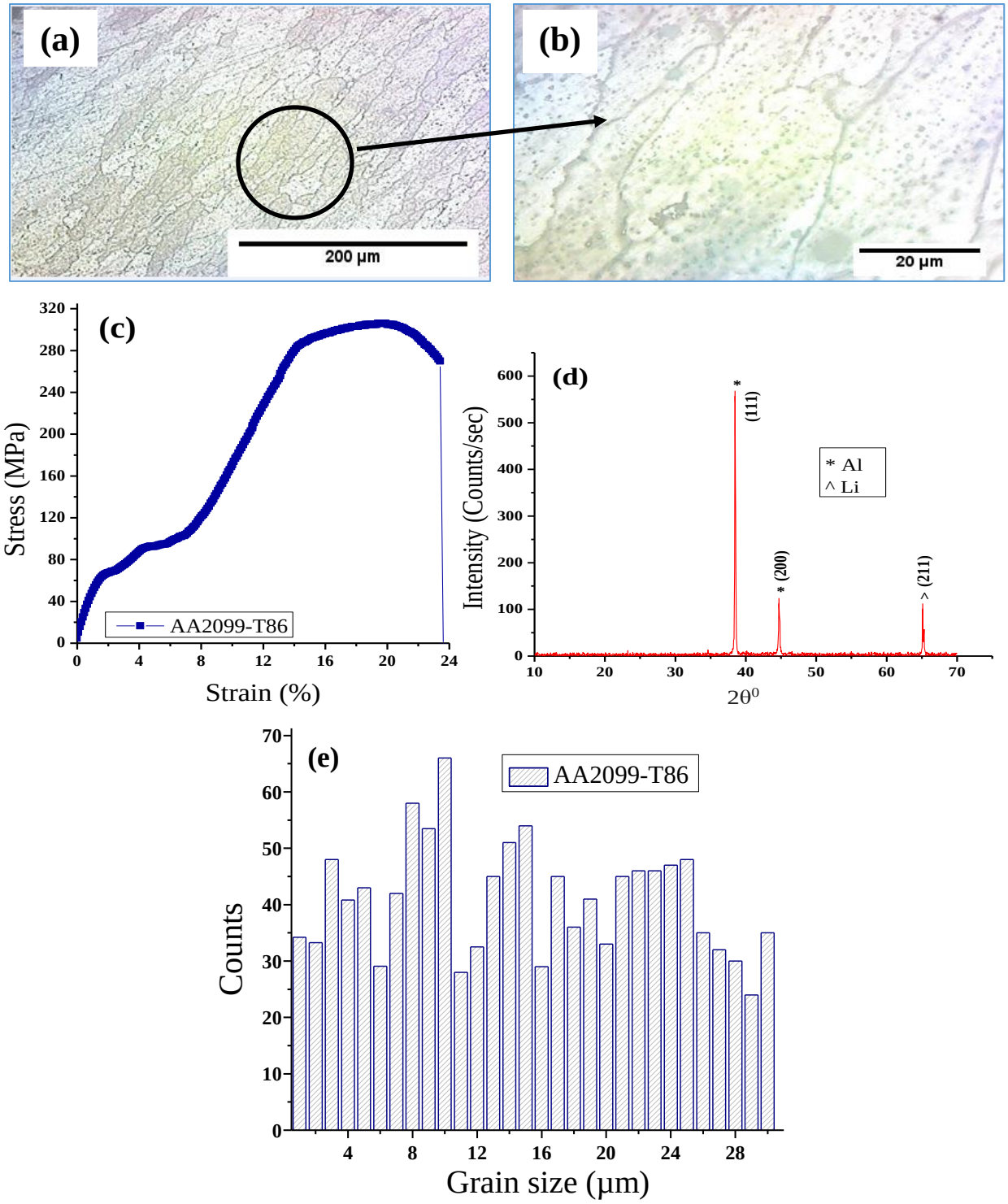

Figure 3.1 Substrate material (AA2099-T86), comprising microscope images at (a) lower magnification (b) higher magnification, (c) stress-strain plot, (d) XRD plot, and (e) measurements of grain size

Figure 3.1(d) provides an XRD plot of the substrate material, where the primary elements, aluminum (Al) and lithium (Li), are identified at various peaks with differing intensities, indicating their presence and distribution within the material. Additionally, the histogram in Figure 3.1(e) depicts the average grain size of the parent material, which is measured to be 67 μm. This comprehensive set of figures provides a thorough understanding of the microstructural and mechanical characteristics of the substrate material.

3.2 SAMPLE PREPARATION

3.2.1 Macrostructure Characterization

The macrostructure of the weld bead dimensions provides insights into the depth of metal penetration, which is crucial for evaluating the weld's strength and quality. To conduct the analysis, specimens were prepared by cutting out a 10 x 10 mm square section from the weld bead. The cross-sectional surface of the weld bead was carefully polished with emery paper of different grits, ranging from 320 to 2000. This polishing process, which included both dry and wet techniques, was performed to clearly expose the macrostructure of the weld bead.

3.2.2 Microstructure Characterization

Microstructure characterization involves examining grain structure, boundaries, and size, which is performed using an Olympus GX41 inverted metallurgical microscope. Microstructure specimens were prepared by cutting a 10 mm x 10 mm section from the weld bead, which was then embedded in bakelite powder using a hot press at 135°C for 20 minutes and allowed to cool for 15 to 20 minutes. The cross-sectional surface was first dry-polished with various grades of emery paper, then wet-polished with velvet cloth and alumina powder. After polishing, the

specimens were dried with a hot air blower. For detailed microstructure analysis, Keller's reagent (consisting of 3 mL HCl, 20 mL HNO3, and 2 mL HF in 175 mL H2O) was used to segment, polish, and etch the joints, ensuring a thorough examination of weld quality.

3.2.3 Microhardness

The hardness of the HAZ and fusion region of the weld bead samples was estimated using a Vickers microhardness tester (Struers ApS DURAMIN-40 M1). An applied load of 300 grams was maintained for 20 seconds during the testing. Prior to testing, the samples were mounted with bakelite powder in a mounting press to ensure proper preparation and handling. The samples were carefully polished with emery paper up to a 1200 grit level and then finished with alumina polishing to obtain a smooth surface. A diamond pyramid indenter was employed to create indentations on the samples. For accuracy, three indentations were made laterally on each sample. The hardness values from these measurements were averaged to obtain a reliable measure of hardness for the fusion region and HAZ in all the samples. This comprehensive preparation and testing process is crucial for accurately assessing the hardness properties of the weld bead.

3.2.4 Tensile Testing

The tensile tests were performed using a Universal Testing Machine (UTM) (Tinius Olsen H50KS) with a 50 kN capacity, operating at a cross-head speed of 3 mm per minute. The specimens were prepared according to ASTM-E8M standards, with a gauge length of 30 mm, as shown in Figure 3.2. During testing, both the Ultimate Tensile Strength (UTS) and the percentage of elongation were precisely measured for each specimen. To ensure result reliability,

three samples were tested, and the average values were computed and reported. This thorough preparation and testing process allows for precise measurement of the tensile properties, providing a clear understanding of the material's performance under tensile stress.

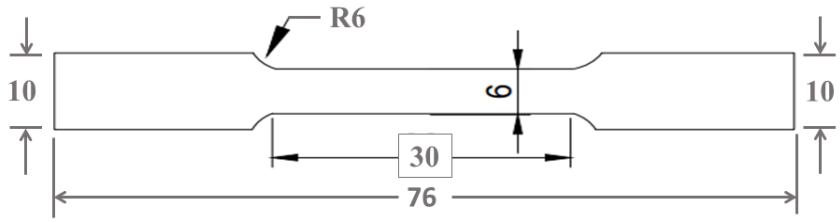

Figure 3.2 Dimensions of tensile specimen as per ASTM-E8M standard

3.3 EXPERIMENTAL MACHINES

3.3.1 CMT machine

A CMT welding machine is a state-of-the-art device known for its compact size and versatility, integrating CMT technology to achieve exceptional welding quality. In this research, the TPS400i welding machine is utilized as shown in Figure 3.3. This machine excels in a wide array of applications, making it suitable for welding materials such as steel, stainless steel, and aluminum. The TPS400i's CMT welding machine optimizes the welding process by precisely controlling the oscillation and melting behavior of the welding wire. This refined control results in reduced heat input and minimal spatter, thus improving the overall quality of the weld.

The machine is capable of handling both thin and thick materials, providing a high level of efficiency and performance. Compared to traditional welding machines, it significantly reduces energy consumption by approximately 30% to 40%, thanks to its advanced technology. Specifically, during the short-circuit phase of the welding process, the machine reduces welding time to just a quarter of that required by conventional methods, where the current is nearly zero. This advancement leads to substantial cost savings in both welding operations and energy usage.

The machine features a sophisticated control system that enables precise adjustment of welding parameters, which enhances the consistency and quality of the welds produced. It is equipped with integrated sensors and feedback mechanisms that ensure optimal performance throughout the welding process. The user interface includes an intuitive control panel and display, allowing for straightforward operation and parameter adjustments. Designed with a compact and lightweight profile, the machine is easily transportable and adaptable to various workspaces. Its construction is robust, ensuring durability and reliability in demanding industrial environments. The machine also supports connectivity options for data transfer and integration with welding management systems, which enhances its versatility.

Safety is a priority with built-in features that protect both the machine and the user, including safeguards against overheating and fault detection. The machine operates on standard industrial power supplies (e.g., 400V, 50/60 Hz) and offers a wide range of output currents to accommodate different welding tasks. Its design supports high-duty cycles, making it reliable for continuous operations. The complete specification of this machine is given in Table 3.3. Ideal for manufacturing and fabrication in sectors such as automotive, aerospace, and construction, the Fronius TPS400i CMT welding machine stands out for its innovative Cold Metal Transfer technology. It provides precise control, high efficiency, and versatility, making it a robust and user-friendly choice for professional welding applications that demand high-quality and consistent results.

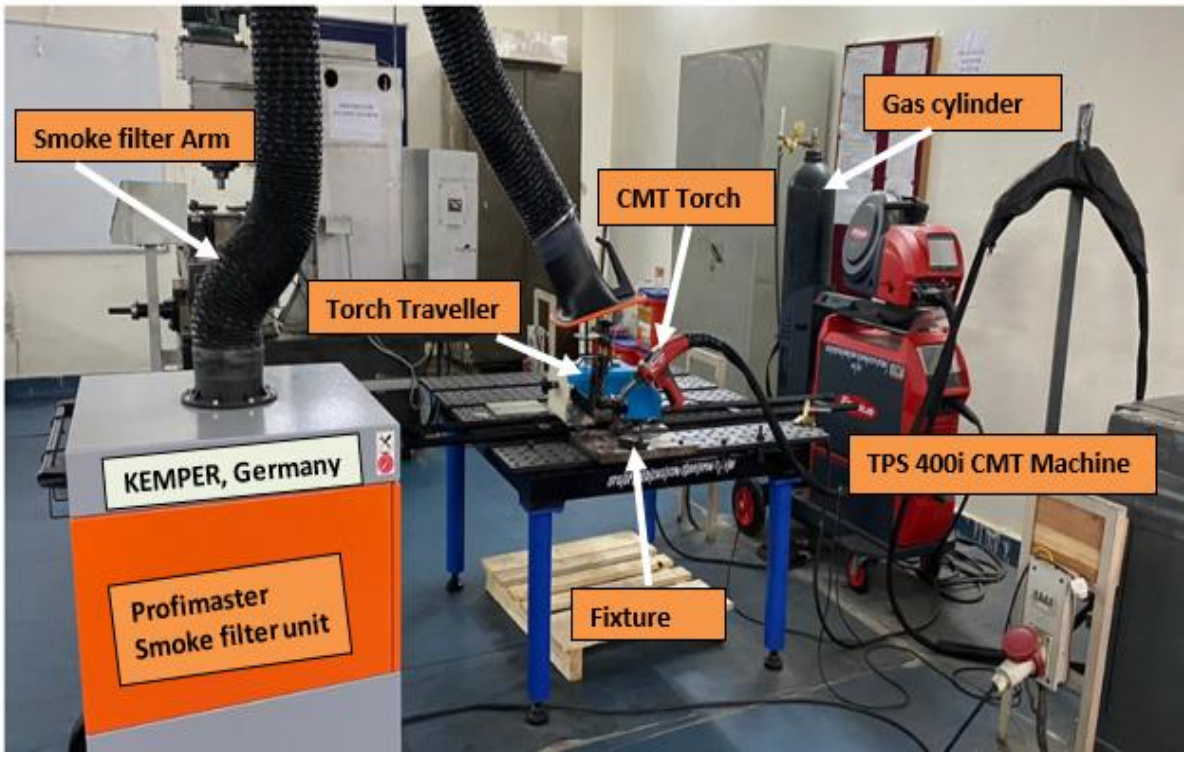

Figure 3.3 TPS400i CMT machine

Table 3.3 Specification of CMT machine (TPS 400i)

Specifications	Range	Units
Mains voltage	3 x 460	V
Maximum welding current	400	A
Minimum welding current	3	A
Welding current / Duty cycle [10 min/40°C]	400 / 40	A / %
Welding current / Duty cycle [10 min/40°C]	360 / 60	A / %
Welding current / Duty cycle [10 min/40°C]	320 / 100	A / %
Operating voltage	14, 2-34, 0	V
Open circuit voltage (OCV)	73	V
Mains frequency	50-60	Hz
Dimension / L	706	mm
Dimension / W	300	mm
Dimension / H	300	mm

3.3.2 Tensile Testing Machine

In engineering, selecting the appropriate materials for various applications largely depends on their mechanical properties, like tensile strength and elongation. These properties are assessed through a process called tensile testing, which is essential for evaluating the performance of new materials and comparing them to existing alternatives in the market. Several critical factors, like composition of materials, temperature, and molecular configuration, can affect the ultimate tensile strength of a material.

- **Material composition:** It determines its molecular arrangement and the nature of molecular bonding, which in turn influences its ultimate tensile strength. Different compositions lead to variations in molecular binding and structural integrity.
- **Temperature:** The ultimate tensile strength of a material generally increases with rising temperature up to a certain threshold. Beyond this optimal temperature range, however, the tensile strength can start to decline.
- **Molecular configuration:** The arrangement of molecules within a material has a profound effect on its tensile strength. Even slight alterations in the molecular configuration can lead to significant changes in how the material responds to tensile forces.

To precisely determine ultimate tensile strength, materials are tested using a Universal Testing Machine (UTM). This study utilizes the Tinius Olsen H50KS to conduct tensile testing, as illustrated in Figure 3.4, with its specifications detailed in Table 3.4. The tensile test specimens are prepared in accordance with ASTM-E8M standards. Wire Electrical Discharge Machining is used to cut out the tensile specimens from the butt-welded plates. During the tensile test, which

is conducted at room temperature, the specimen is subjected to a controlled cross-head speed of 3 mm/min, ensuring accurate and consistent measurement of tensile properties.

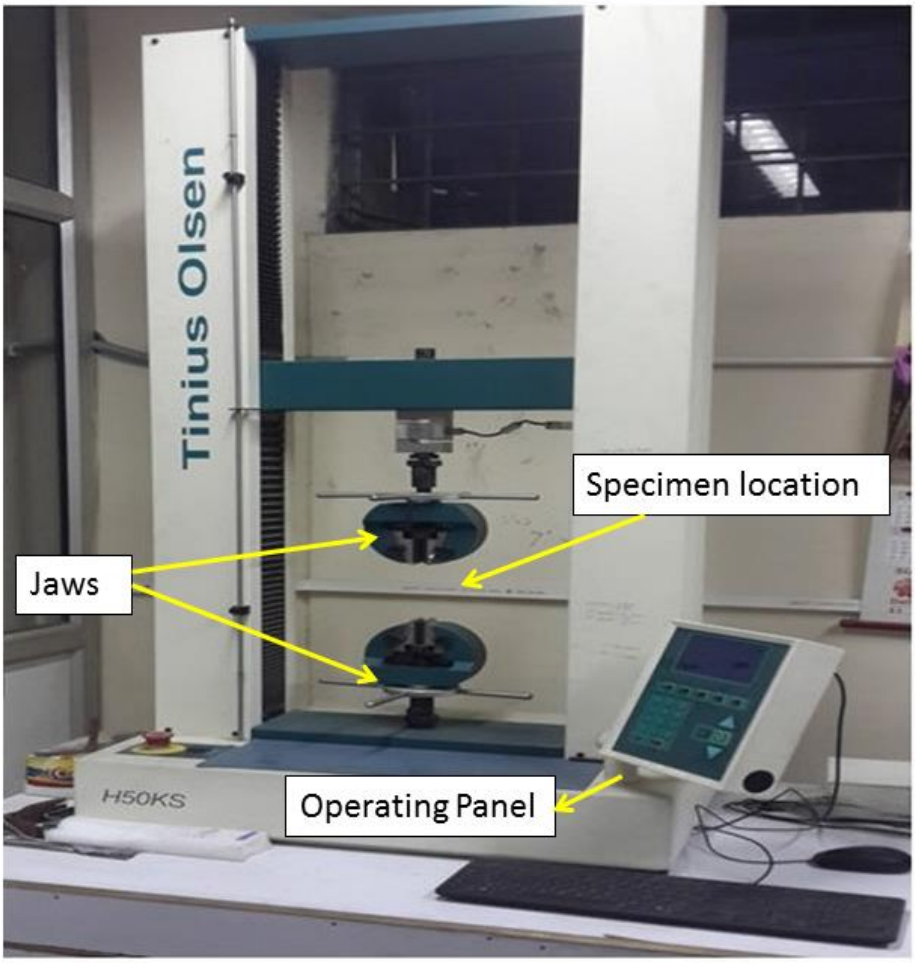

Figure 3.4 Tensile testing machine (Model: Tinius Olsen H50KS)

Table 3.4 Tensile testing machine specifications

Capacity	50/5000	kN/Kg
Clearance between columns	405	mm
Load cells	Rapid change, low profile Z type load cells with digital encoading for automatic recogonition.	-
Maximum crosshead travel	1100	mm
Testing speed range	0.001-500	mm/min
Capacity at maximum speed	25	kN
Maximum speed at capacity	250	mm/min
Jog speed	0.001-500	mm/min
Return speed	0.001-500	mm/min
Dimensions (H x W x D)	1613 x 720 x 500	mm
Weight	140	Kg

3.3.3 Microhardness Testing Machine

In this study, microhardness measurements are conducted using the Struers Duramin-40 testing machine that offers high accuracy for such analyses, as illustrated in Figure 3.5 and detailed in Table 3.5. During the microhardness test, a Vickers diamond indenter is employed. This indenter, which is diamond-tipped and shaped like a square pyramid, is pressed into the material's surface under a controlled load of 300 grams. Applying this load results in an indentation, leading to a permanent deformation on the material’s surface that mirrors the shape of the indenter.

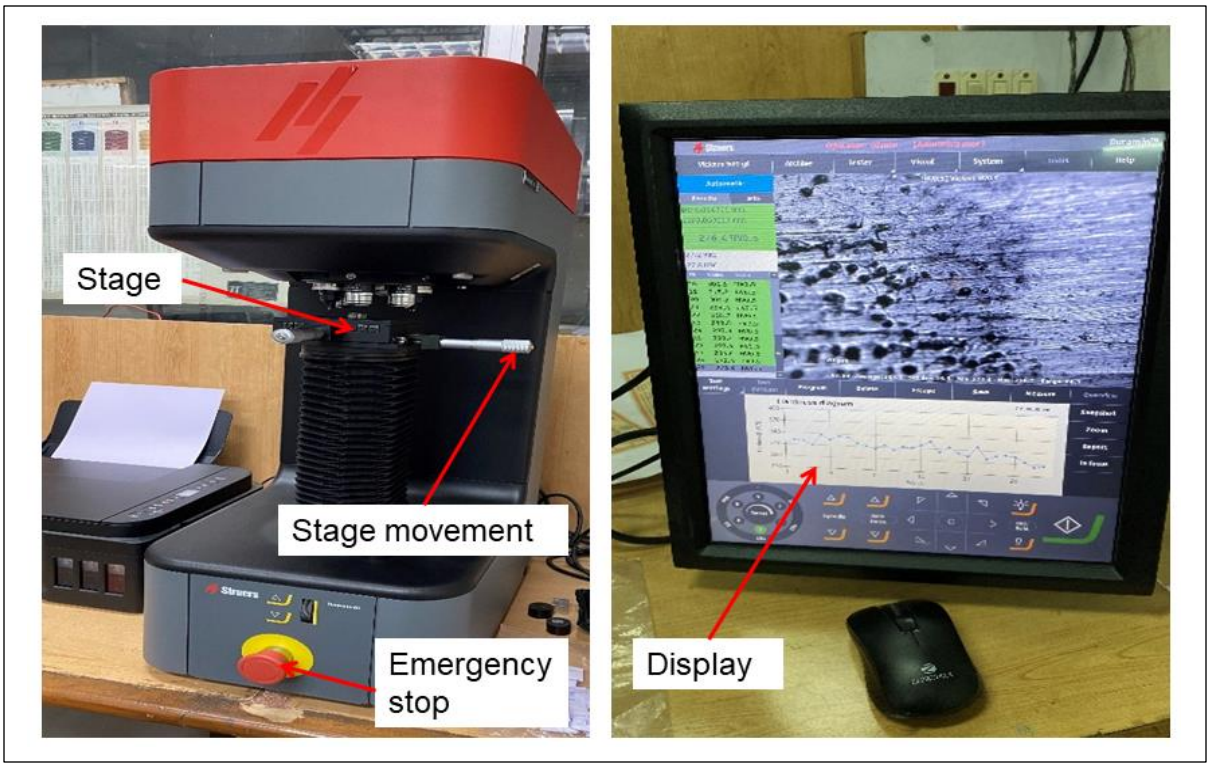

Figure 3.5 Microhardness testing machine (Model: Struers Duramin-40)

Table 3.5 Microhardness testing machine specifications

Specification	Details
Model	Struers Duramin-40M1
Testing Methods	Vickers (HV), Knoop (HK) (optional for other methods)
Load Range	Typically from 10 gf to 10 kgf
Indentation Types	Diamond pyramid (Vickers), Knoop
Dwell Time	Adjustable, typically up to 60 seconds
Optical System	High-quality optical microscope with variable magnification
Measurement Accuracy	High precision, typically within 1%
Control System	Touchscreen interface with programmable settings
Data Management	Advanced software for analysis, reporting, and data export
Environmental Conditions	Operates under standard laboratory conditions
Power Supply	Typically operates on 220V, 50/60 Hz
Connectivity Options	Data transfer via USB or network
Sample Preparation Requirements	High-quality surface finish for accurate results
Software Capabilities	Includes statistical analysis, graphical representation, and customizable reports
Weight	101 Kg

3.3.4 Optical Microscopy

Optical microscopy is performed using the Olympus GX41 compact inverted metallurgical microscope, as shown in Figure 3.6 and described in Table 3.6. This advanced microscope is

designed for efficient and precise characterization of specimens to ensure they meet metallurgical standards. Its compact and lightweight design enhances portability, making it suitable for both laboratory and on-site inspections. Key features of the GX41 include its mobility, ergonomic design, and superior imaging capabilities. The microscope's compact form allows it to be easily positioned in constrained spaces and moved as needed. Ergonomically, the tilting binocular observation tube allows for comfortable eyepoint adjustment, accommodating both standing and seated users, thus enhancing user comfort and reducing strain. The GX41 excels in delivering high image quality and resolution with its brightfield and polarized illumination capabilities. Its infinity-corrected UIS2 optics ensure exceptionally clear and bright images across the entire field of view, with objective magnifications ranging from 5x to 100x. This ensures high-clarity observations, whether in brightfield or polarized light conditions, meeting the demands of various metallurgical analysis tasks.

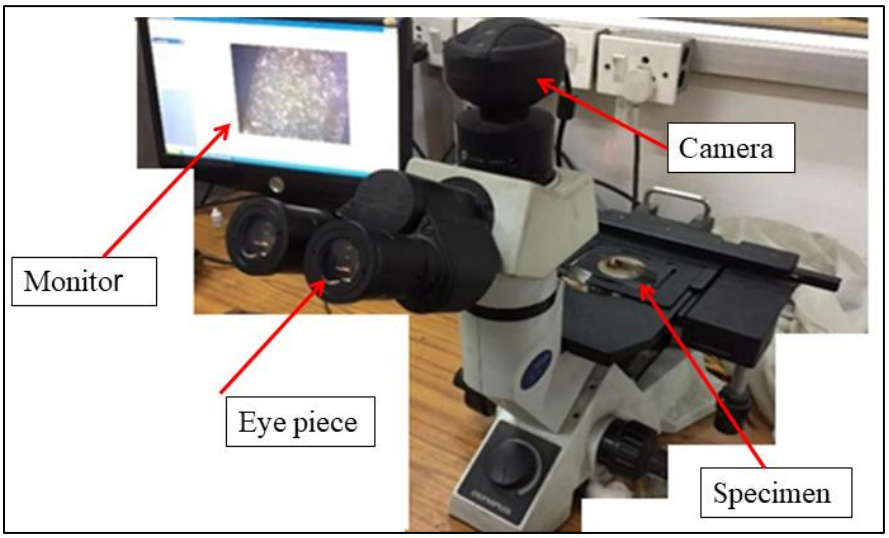

Figure 3.6 Olympus GX41 compact inverted metallurgical microscope

Table 3.6 Optical Microscope specifications

Optical System			UIS2 Optical System (Infinity-corrected)
Microscope Frame	Observation Method		BF/KPO
	Reflected/Transmitted		Reflected
	Illumination System	Reflected light	30W Halogen or Fiber Light Guide (Light source:100 W)
	Focus	Motorized/Manual	Manual Revolving Nosepiece Up/Down Movement (Stage Stationary Type)
		Stroke	9 mm
		Manual type	Quadruple for BF
Stage	Stroke		120(X)x78(Y) mm
Observation Tube	Standard Field (Field number 18)	Inverted Image	Tilting Binocular Observation Tube
Dimensions			236(W) x 624(D) x 407(H) mm
Weight			10 kg

3.3.5 Vision Inspection Machine

Visual inspection is conducted with the Sipcon multi-sensor inspection system, which is illustrated in Figure 3.7 and outlined in Table 3.7. This system is distinguished by its high performance and durable design, offering extended service life with minimal maintenance requirements and low power consumption. The Sipcon system integrates three distinct measurement technologies: vision, touch probe, and laser. The vision system excels in providing high-throughput, non-contact measurements for flat surfaces, enabling precise and rapid capture of even the finest details. The touch probe technology is ideal for three-dimensional measurements, making it suitable for assessing non-flexible components and detailed analysis of

metal parts, such as apertures and included angles. Meanwhile, the laser system offers exceptional accuracy in depth measurements and is particularly effective for surface contouring and scanning. It is well-suited for complex mold contouring and measuring soft or flexible components.

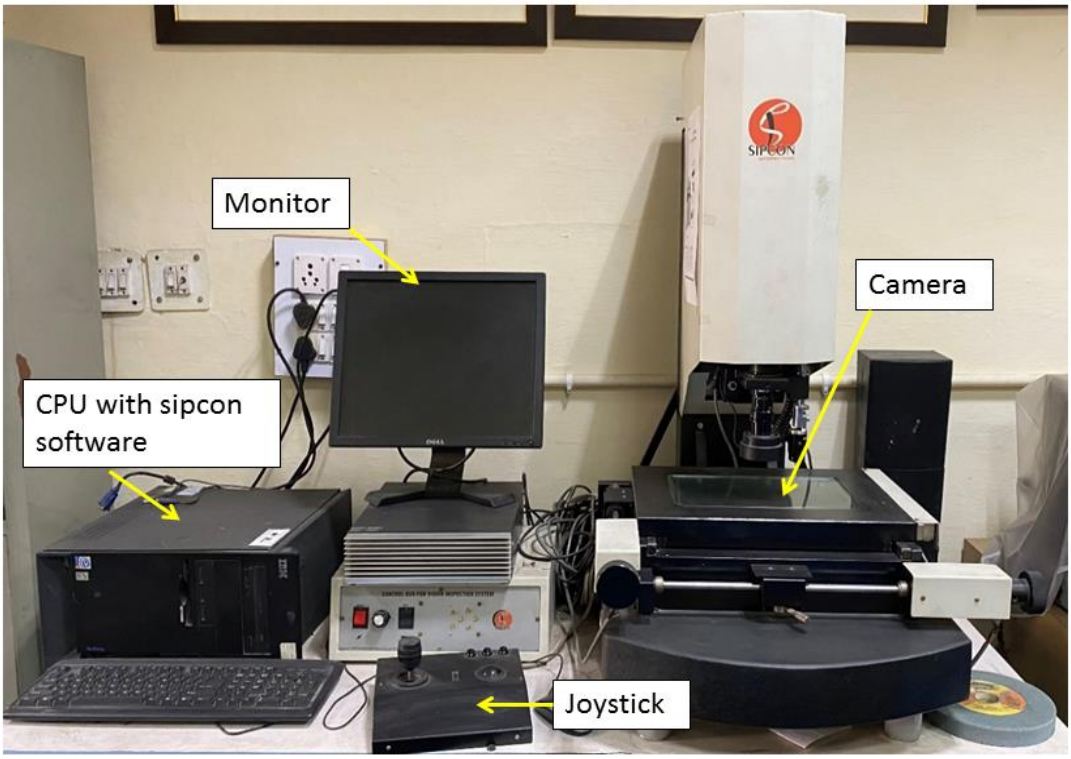

Figure 3.7 Sipcon multi sensor inspection system

Table 3.7 Vision Inspection Machine specifications

Feature	Specification
Model No.	SVI-5300-CNC-VT
Software	QC-5300-VED-CNC / MSU-25D-CNC
Operation	Manual with quick release knob & CNC
Base Platform and Column	Granite
Platform Load Capacity	30 Kg
Power Supply	220 – 240V, 50/60 Hz
Motion Control Through Joystick	Standard
Programmable Light Control	Optional
Autofocus	Optional
Touch	Renishaw TP-8
Measuring Range	200 x 150 x 100 mm
Resolution	0.005 / 0.001 / 0.0005 mm
Linear Accuracy	(3 + L/200) micron
Repeatability	+/- (0.002 mm)
Vision	1/3" High Resolution CCD Camera
Magnification	Optical Magnification 0.7x – 4.5x
Video Edge Detection	Standard
Optional Hardware	PC P4 + 17" TFT Monitor
Illumination Surface	Fibre Optic / LED
Illumination Contour	Halogen Lamp / LED

3.3.6 Field Emission Gun Scanning Electron Microscope

Field Emission Scanning Electron microscopy utilizes an electron-optical column, as illustrated in Figure 3.8 and detailed in Table 3.8. This technique involves directing an extremely fine electron beam, typically with a diameter of about 10 nm, to achieve high-resolution imaging. The diameter of the electron probe is critical because it significantly affects the resolution of the FESEM images. The imaging technique employs raster scanning, in which the electron probe methodically scans across the entire specimen. During this scanning process, accelerated electrons are directed at the specimen and interact with it, leading to various scattering

phenomena. These interactions can be classified into elastic and inelastic scattering. The resulting image brightness varies based on the type of electrons detected. Secondary electrons, which are emitted from the surface of the specimen, contribute to the surface structure's visibility and offer a topographical contrast. Conversely, backscattered electrons, which have higher kinetic energy and come from deeper within the specimen, provide information about the underlying structure. This allows for the assessment of deeper layers and reveals contrasts based on the specimen’s chemical composition.

Figure 3.8 Field Emission Scanning Electron Microscopy (FESEM) machine

Table 3.8 FESEM machine specifications

Feature	Specification
Electron Optics	High-resolution FESEM column for high brightness/high current
Ion Optics	Magnum ion column with Ga liquid metal ion source (1500 hours)
Electron Beam Resolution	1.2 nm @ 30 kV (high vacuum), 1.5 nm @ 30 kV (ESEM), 1.5 nm @ 3 kV (low vacuum)
Ion Beam Resolution	10 nm @ 30 kV @ 1pA
Accelerating Voltage	200V to 30 kV (electron beam), 5 to 30 kV (ion beam)
Detectors	Everhardt-Thornley SED, Low-vacuum SED, Gaseous SED, IR-CCD, EDS, Gaseous BSED
Specimen Stage	4-axis motorized eucentric goniometer stage
Stage Specifications	X: 50 mm, Y: 50 mm, T: -15° to +75° (manual), Z: 50 mm (25 mm motorized), Rotation: 360° continuous

3.3.7 X-Ray Diffraction machine

Diffraction patterns result from the scattering of light by a regularly arranged structure with long-range order, leading to constructive interference at specific angles. To interpret X-ray diffraction (XRD) data, researchers identify patterns that indicate the orientation of the crystal structure and further analyze these patterns using Miller indices related to the diffraction peaks. The wavelength of X-rays is similar in scale to the distances between atoms. As X-rays interact with these atoms, they scatter, producing a diffraction pattern that reveals information about the crystal's atomic structure. The Bruker D8 advanced XRD machine is utilized to capture these spectra, as shown in Figure 3.9, with its technical specifications listed in Table 3.9. The diffraction peaks observed in the XRD pattern correspond to atomic planes and are crucial for analyzing the atomic and microstructural arrangement. Bragg’s law is used to determine the

position of diffraction peaks. Bragg's law allows for identifying the angles at which diffraction peaks occur due to constructive interference from X-ray scattering by crystal planes. The intensity and position of these peaks are influenced by the crystal structure, specifically the periodic arrangement of atoms throughout the crystal.

Figure 3.9 X-Ray diffraction machine (Model: BRUKER D8 ADVANCED)

Table 3.9 XRD machine specifications

Feature	Specification
X-ray Source	2.2 kW Cu anode long fine focus ceramic tube
Running Condition	40 kV and 40 mA
Beam Shaping Optics	Collimated, compressed, and frequency filtered by Göbel mirror and V-Groove
Beam Dimensions	0.3 mm x 11 mm
Göbel Mirror	60 mm multilayer on high precision parabolic surface
Goniometer	
- Measurement Circle Diameter	250 mm (max), 100 mm (min)
- Smallest Angular Step Size	0.0001°
- Reproducibility	+/- 0.0001°
- Max Rotational Speed	1500°/min
- Angular Range (Theta)	-5° to 40°
- Angular Range (2Theta)	-10° to 60°
Reflectometry Sample Stage	
- Sample Size	200 mm diameter, 50 mm thick
Detector	
- Max Count Rate	2 x 10^6 s^{-1} (max), should not exceed 5 x 10^5 s^{-1} for more than 1 second
- Detector Electronics Count Rate	3 x 10^7 s^{-1}

3.4 OPTIMIZATION OF CMT WELDING PROCESS PARAMETERS

3.4.1 Process parameters

Welding Current (I): The welding current significantly affects both the weld bead width and penetration depth. Increasing the current results in a wider weld bead with deeper penetration. Conversely, decreasing the current produces a narrower weld bead with shallower penetration [Little, 1994]. The welding current significantly affects bead geometry, penetration, leg length, and toe angle due to its impact on heat input and metal deposition. It has a strong positive linear

relationship with all bead geometry properties [Lee et al., (2018)]. The short circuit between molten pools at low current significantly reduced spattering caused by electromagnetic repulsion during the initial short circuit [He et al., 2022]. To ensure a sound weld joint without lack of penetration, selecting the appropriate welding current is crucial. In this research, welding current is chosen as a key process parameter.

Welding speed (S): it denotes the rate at which the nozzle progresses over the welding plate. Faster welding speeds lead to reduced heat input, which can result in insufficient penetration of the weld. On the other hand, very slow welding speeds increase heat input, which may cause excessive melting of the base material.

Contact tip to work distance (CTWD): It is the distance between the contact tip of the electrode wire and the surface of the material being welded. An appropriate CTWD ensures a well-formed weld bead. Variations in CTWD affect the size and appearance of the weld bead, as well as its shape, which is influenced by the heat input [Rohe et al., 2024].

Voltage: Arc voltage directly affects the amount of heat introduced during the welding process. In this study, the welding current is treated as an independent parameter, meaning it is deliberately set and controlled. The arc voltage, however, is dependent on the welding current. As the welding current increases or decreases, the machine automatically adjusts the arc voltage to maintain the appropriate heat input. This automatic adjustment ensures consistent welding quality by accommodating fluctuations in the welding current and stabilizing the arc voltage accordingly.

Gas flow rate: It serves to protect the weld from contamination by atmospheric gases such as oxygen, hydrogen, and nitrogen during the solidification of the molten metal [Reddy et al.

(1998)]. It affects weld bead quality and penetration. A constant gas flow rate is maintained in this work.

Wire feed rate: The wire feed rate refers to how fast the welding wire moves from the spool through the nozzle. It directly affects how quickly weld metal is deposited and the shape of the weld bead. Increasing the wire feed rate enlarges bead width, penetration, fused base metal area, deposited weld metal area, and HAZ width and area [John et al., 2021].

Filler wire size: A 1.2 mm diameter filler wire is used in this work. Larger wire sizes result in shallower penetration and faster deposition rates, while smaller wire sizes lead to deeper penetration and slower deposition rates. According to a review of the literature and trial experiments, the main welding parameters affecting the weld bead are current, welding speed, CTWD, and shielding gas flow rate. Additionally, factors such as filler wire selection, size, shielding gas type, joint type, and pre-weld cleaning impact wettability, spreadability, and joint strength.

3.4.2 Taguchi design

Based on an extensive literature review and preliminary trials, key welding parameters like welding speed, welding current, and contact tip to work distance (CTWD) were identified and fixed for conducting CMT weld bead experiments. Other parameters, including shielding gas flow rate, wire feed rate, and arc correction factor, were kept constant throughout the experiments. To systematically investigate the effects of these variables, a Taguchi L9 orthogonal array design matrix was employed, encompassing nine parametric combinations using three levels each of welding current, welding speed, and CTWD. Table 3.10 presents the values of the welding parameters and their respective levels according to the Taguchi L_9 design.

Minitab software was utilized to determine the optimal parameters for achieving superior responses. The Taguchi L_9 method was applied specifically for weld-on-bead experiments to optimize the input parameters. Additionally, the CRITIC-ROV multicriteria decision-making method was utilized to determine the ideal input parameters for achieving the best combined weld-on-bead geometry in the AA2099-T86 alloy using both CMT and pulse MIG welding techniques. The flow process chart of the CRITIC and ROV-based Taguchi optimization approaches is shown in Figure 3.10. The CRITIC and ROV methods are explained in the following section.

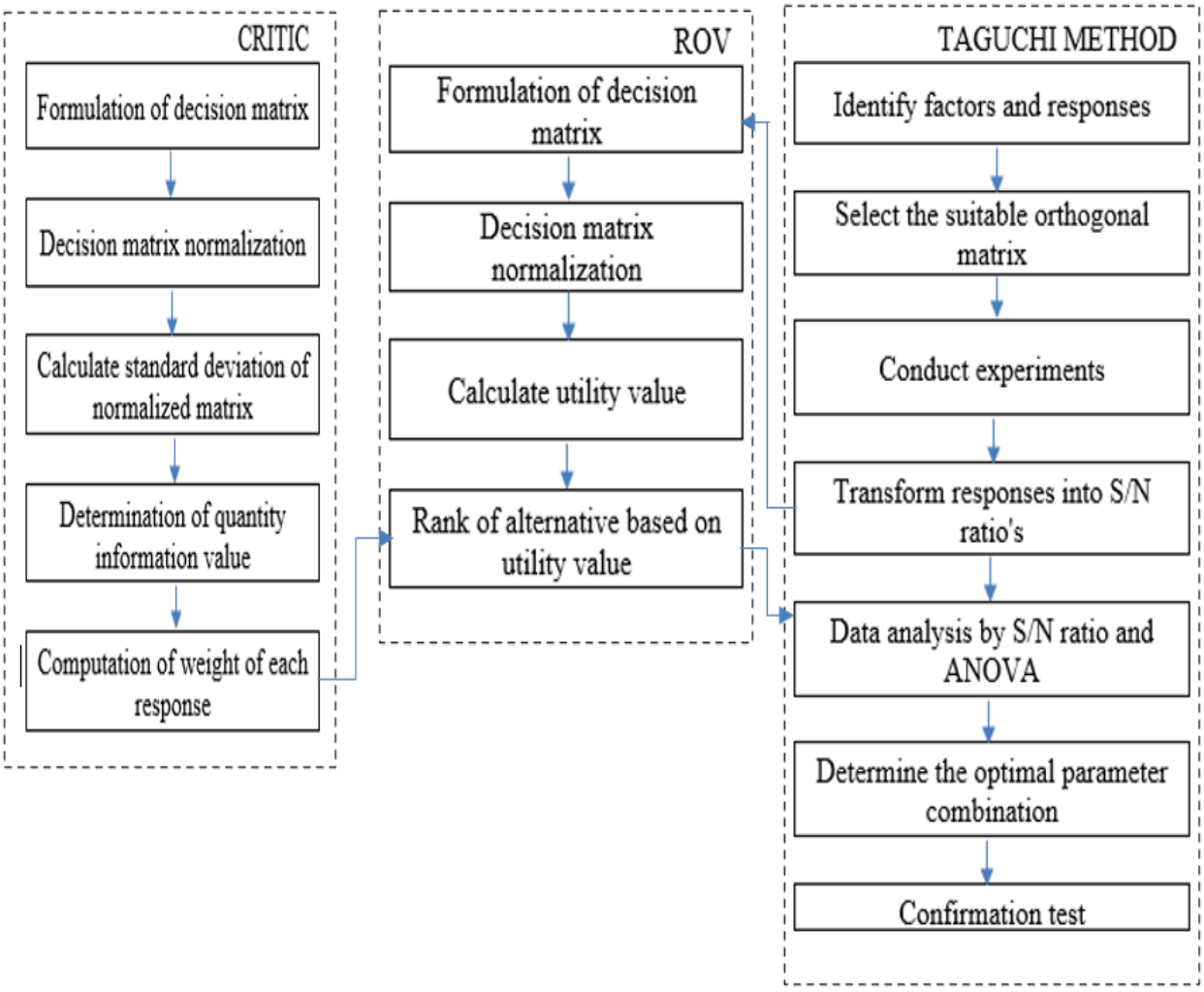

Figure 3.10 The flow process chart of CRITIC and ROV-based Taguchi method

Table 3.10 Welding parameters and their levels as per Taguchi L_9 design

Parameters	**Symbol**	**Unit**	**L_1**	**L_2**	**L_3**
Welding current	(I)	A	150	165	180
Welding speed	(S)	mm/s	6	8	10
CTWD	(D)	Mm	4	6	8

3.4.3 Criteria importance through intercriteria correlation (CRITIC) method

This method considers conflicting relationships and the contrast intensity between each criterion/output response. A criterion with a higher degree of conflict and contrast intensity with other criteria gets higher weight. It determines the objective weights of the criteria based on correlation analysis among them. The computational steps are explained below [Diakoulaki et al., 1995; Mukhametzyanov et al., 2021; Madic et al., 2015].

Step 1. Formulation of the decision matrix 'Z' where the number of experiments is arranged in rows and output responses are taken in columns, respectively, as given in Equation (1)

$$Z = [Z_{ij}]_{m\times n} = \begin{bmatrix} z_{11} & z_{12} & \dots & z_{1j} & \dots & z_{1n} \\ z_{21} & z_{22} & \dots & \dots & \dots & z_{2n} \\ \dots & \dots & \dots & \dots & \dots & \dots \\ z_{i1} & \dots & \dots & z_{ij} & \dots & z_{in} \\ \dots & \dots & \dots & \dots & \dots & \dots \\ z_{m1} & \dots & \dots & z_{mj} & \dots & z_{mn} \end{bmatrix} \text{……..(1)}$$

$where,\ \ i = 1, 2, \dots, m;\ j = 1, 2, \dots, n$

x_{ij} signifies the performance value of i^{th} experiment for j^{th} output response, m signifies the number of experiments, while n represents the number of output responses.

Step 2. Decision matrix normalization using Equation (2).

$$a_{ij} = \frac{z_{ij} - z_j^{worst}}{z_j^{best} - z_j^{worst}} \text{ …….. (2)}$$

Where, a_{ij} represents the normalized value of, z_{ij}, For beneficial output response, $z_j^{best} = \max(z_{ij}, i = 1, \dots m)$ and $z_j^{worst} = min(z_{ij}, i = 1, \dots m)$. For non-beneficial output response, $z_j^{best} = \min(z_{ij}, i = 1, \dots m)$ and $z_j^{worst} = max(z_{ij}, i = 1, \dots m)$.

Step 3. Determination of the standard deviation, σ_j value for each output response using Equation (3).

$$\sigma_j = \sqrt{\frac{\sum_{i=1}^{m}(z_{ij}-\mu_j)^2}{n-1}} \dots\dots\dots\dots (3)$$

Where, μ_j represents the mean value of the *j*th output response.

Step 4. Determination of the quantity of information value, q_j using Equation (4)

$$q_j = \sigma_j \times \sum_{i=1}^{m}(1 - p_{ij}) \dots\dots\dots\dots (4)$$

Where, σ_j = standard deviation and p_{ij} = correlation coefficient.

Step 5. Computation of the weight of each output response using Equation (5).

$$w_j = \frac{q_j}{\sum_{i=1}^{m} q_i} \dots\dots\dots\dots (5)$$

3.4.4 Range of value (ROV) method

The range of value (ROV) system was used to determine the ranks and select the best from the alternatives. The computational steps are explained below [Yakowitz et al., 1993; Milos et al., 2015; Hajkowicz et al., 2008].

Step 1. Similar to the CRITIC method

Step 2. Decision matrix (DM) normalization using Equation (6**)** for favourable output responses and Equation (7) for non-favorable output responses.

$$z'_{ij} = \frac{z_{ij}-z_j^{worst}}{z_j^{best}-z_j^{worst}} \dots\dots\dots\dots (6)$$

$$z'_{ij} = \frac{z_j^{worst} - z_{ij}}{z_j^{worst} - z_j^{best}} \text{ …….. (7)}$$

Step 3. The calculation for utility value:

To identify the optimal and least favorable outcomes of each experiment, we aimed to maximize and minimize the utility function, respectively. Let us consider a linear additive model in which ($U_{i,positive}$) indicates the best utility of *i*th experiment and ($U_{i,negative}$) indicates the worst utility of *i*th experiment, as found using Equations (8) and (9), respectively.

$$Maximize: U_{i,positive} = \sum_{j=1}^{q} z'_{ij} \cdot w_j \text{ …….. (8)}$$

$$Minimize: U_{i,negative} = \sum_{j=1}^{q} z'_{ij} \cdot w_j \text{…….. (9)}$$

Where, w_j is the weight of *j*th output response.

Step 4. The rank of the alternative based on utility value: Utility value is obtained by midpoint formula using Equation (10) [Athawale et al., (2011)].

$$U_i = \frac{U_{i,positive} + U_{i,negative}}{2} \text{ …….. (10)}$$

Experiments are ranked on the basis of the values of U_i such that '1' rank is given to the experiment showing the highest U_i value. The rank of the experiments decreases as U_i value decreases.

3.5 EXPERIMENTAL PROCEDURE

3.5.1 Bead-on-plate weld experiments

CMT and pulse MIG bead-on-plate experiments were conducted on AA2099-T86 plates. Preliminary experiments were conducted to establish the range of welding parameters. The chosen parameters and their respective levels are detailed in Table 3.10, in accordance with the Taguchi L_9 orthogonal array. The machine automatically adjusts the voltage within a range of

10V-22.6V, depending on the settings for current, welding speed, and contact tip-to-work distance (CTWD). Pure argon gas was used at a flow rate of 16 L/min throughout all experiments. Figure 3.11 shows the weld bead images of CMT and pulse MIG welding.

Table 3.11 Taguchi L_9 design matrix for CMT and Pulse MIG weld bead

Sr. No.	**Process Parameters**		
	Welding current (A)	**Welding Speed (mm/sec)**	**CTWD (mm)**
1	150	6	4
2	150	8	6
3	150	10	8
4	165	6	8
5	165	8	4
6	165	10	6
7	180	6	6
8	180	8	8
9	180	10	4

Figure 3.11 Weld bead images of (a) CMT and (b) pulse MIG welding

3.6 CMT BUTT WELD JOINT

Experimental trials were conducted on AA2099-T86 sheets. Prior to welding, each sample was thoroughly cleaned with acetone to remove any dirt, oxide films, or paint residues. The samples were firmly clamped to the welding fixtures to avoid any deformation or bending throughout the welding process. For all the experiments, pure argon gas (99.99%) served as the shielding gas. The welding parameters were selected on the basis of Taguchi L_9 design as shown in Table 3.11, which was used for conducting the CMT butt weld joint experiments. Throughout the welding process, the machine was configured to automatically regulate the voltage between 10V and 20.2V, according to the preset input parameters such as welding current, welding speed, and contact tip-to-work distance (CTWD). This ensured consistent and optimal welding conditions across all trials. Welded sample images as per design matrix are shown in Figure 3.12.

Figure 3.12 Welded samples images as per design matrix

Table 3.12 Welding parameters & their levels for CMT butt joints

Weld parameters (unit)	Symbols	Levels		
		L1	L2	L3
Welding speed (mm/s)	WS	6	8	10
Welding current (Ampere)	WC	150	165	180
Contact tip to workpiece distance (mm)	CTWD	4	6	8

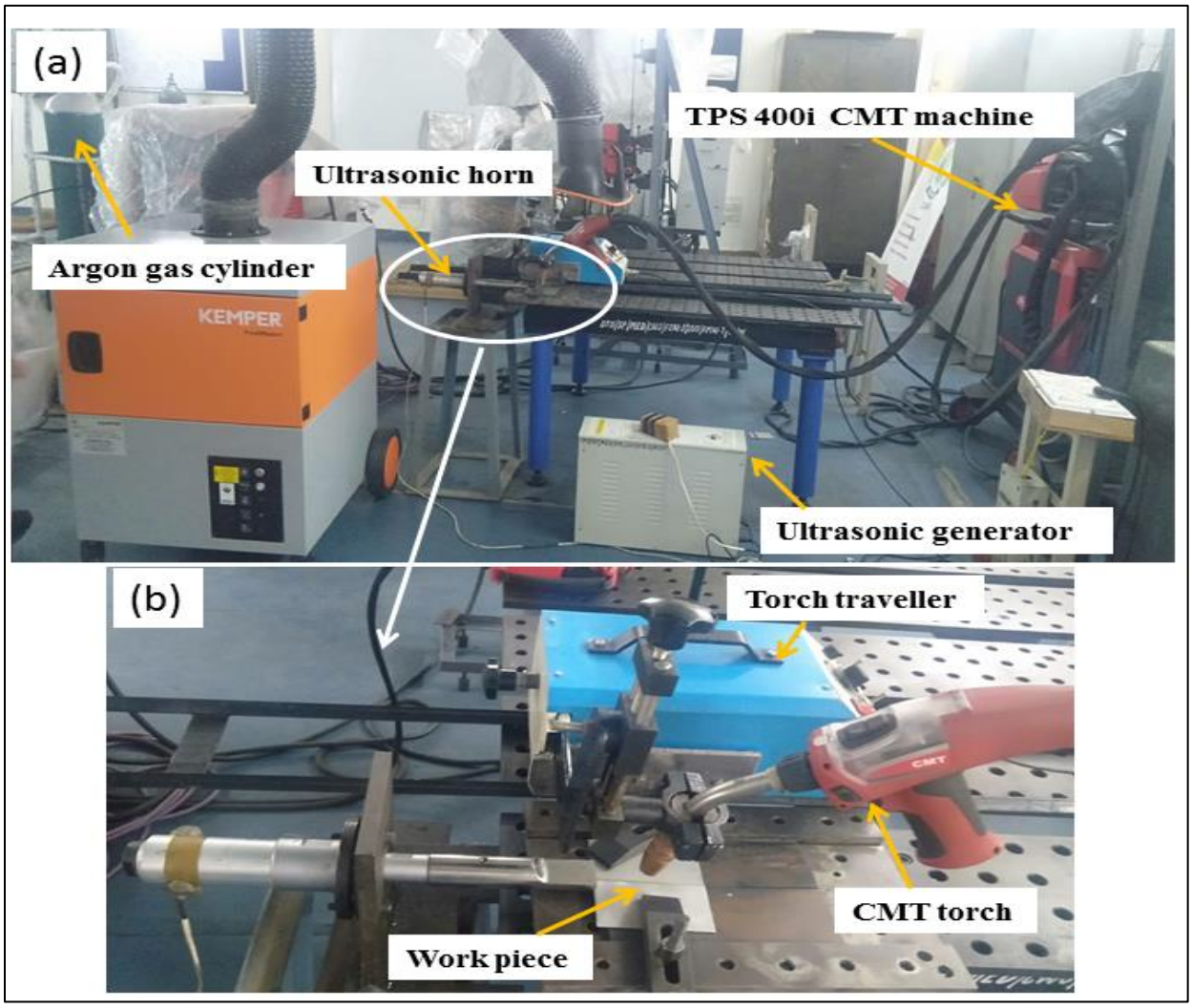

Figure 3.13 (a) CMT welding machine equipped with an ultrasonic attachment, and (b) ultrasonic horn/probe

3.7 CMT BUTT WELD JOINT UNDER DIFFERENT ENVIRONMENT CONDITIONS

The butt joints of the AA2099-T86 alloy were prepared using the CMT welding process under three distinct environments: conventional (C-CMT), liquid nitrogen (LN-CMT), and ultrasonic vibration welding (U-CMT). After conducting numerous trial experiments, the ideal welding parameters were established and set at a welding current of 165 A, a welding speed of 8 mm/sec, and a CTWD of 8 mm for all conditions. Figure 3.13 illustrates the experimental setup, which includes the CMT welding machine equipped with an ultrasonic attachment. The ultrasonic generator box was used to generate vibrations at consistent frequency and amplitude. These vibrations were transmitted to the workpiece via an ultrasonic probe, which made contact with the material, ensuring the effective transfer of ultrasonic energy from the generator to the workpiece. The schematic diagrams of C-CMT, LN-CMT, and U-CMT welding are shown in Figures 3.14, 3.15, and 3.16, respectively.

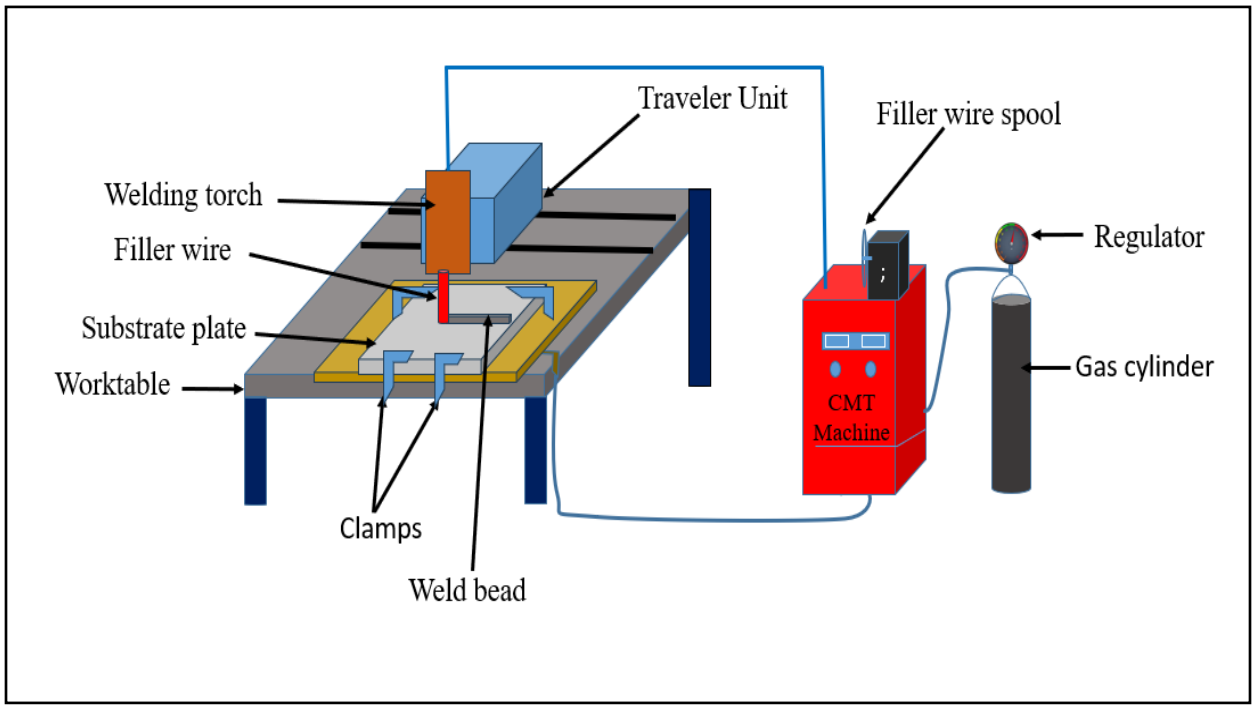

Figure 3.14 Schematic diagram of C-CMT setup

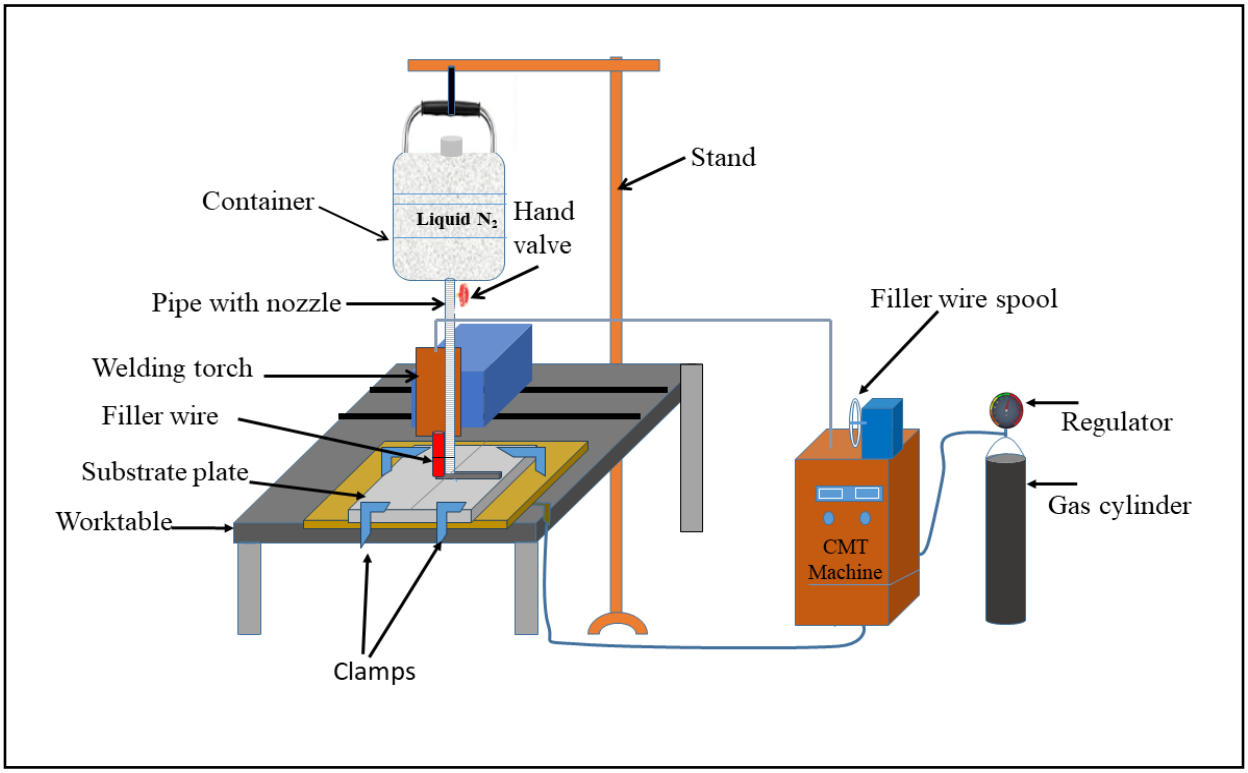

Figure 3.15 Schematic diagram of LN-CMT setup

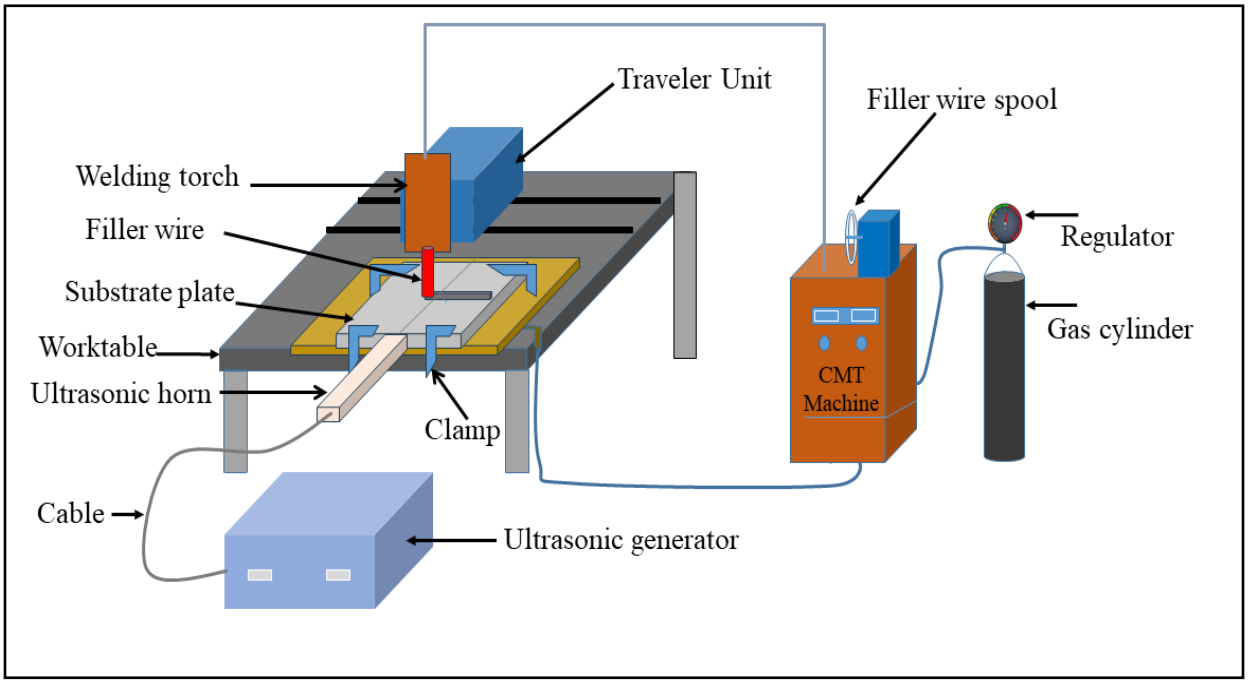

Figure 3.16 Schematic diagram of U-CMT setup

3.8 SUMMARY

This chapter outlined the selection of base material and filler materials, choosing AA2099-T86 and ER4047 (Al-Si alloy) filler wire based on their compatibility. It also outlined the methods for characterizing the material and provided a detailed, step-by-step procedure for preparing samples for various tests, including macrostructure and microstructure analysis, microhardness assessment, and tensile testing. The chapter also covered the various machines used in the experiments, providing detailed descriptions. The procedures for determining mechanical properties, including tensile and microhardness tests, were discussed. Metallurgical characterization methods, such as microstructure analysis, phase analysis, and elemental composition using field emission scanning electron microscopy (FESEM), optical microscopy (OM), and X-ray diffraction (XRD), were illustrated. All specimens were prepared according to standards. The experimental procedures for weld-on-bead and CMT butt welding under different environments were briefly explained. The Taguchi L_9 technique was applied to optimize input parameters for weld experiments, and the CRITIC-ROV multicriteria decision-making technique was utilized to identify optimal input parameters for the combined responses of weld bead geometry of A2099-T86 alloy using CMT and pulse MIG welding processes.

CHAPTER 4: EXPERIMENTAL RESULTS AND DISCUSSIONS ON WELD-BEAD

4.1 OPTIMIZATION OF WELD-BEAD PARAMETERS

4.1.1 Introduction

Weld bead analysis provides a comprehensive overview of the weld bead geometry, encompassing critical dimensions such as weld penetration (P), weld reinforcement (R), contact angle (θ), and weld width (W), as depicted in Figure 4.1. Assessing these dimensions is crucial for analyzing the internal structure of the weld bead, which significantly impacts the overall welding costs. Weld reinforcement (R) represents the additional metal on the weld bead's surface, essential for achieving the desired strength and integrity of the weld. Weld penetration (P) indicates how deeply the weld metal has fused with the base metal, which is vital for the strength and longevity of the weld. Weld width (W) measures the span of the weld bead across the base metal's surface, affecting both its appearance and stability. The contact angle (θ) is the angle between the weld bead and the base metal, influencing the smoothness and transition of the weld into the base material.

Accurate measurement of these weld bead dimensions allows for a detailed understanding of the weld quality, enabling optimization of welding parameters to achieve desired weld characteristics. This analysis also aids in predicting potential issues, such as undercutting or lack of fusion, and helps in implementing corrective measures to enhance weld performance and reduce costs. By thoroughly examining weld bead geometry, it ensures that the welding process meets the required standards and specifications, thereby improving efficiency and minimizing material waste. The evaluation of dilution (%) is given in equation 11 [Koli et al., (2019)].

Dilution (%) =Weld penetration area (P)/ (Weld penetration area (P) + Weld reinforcement area (R)) …….. (11).

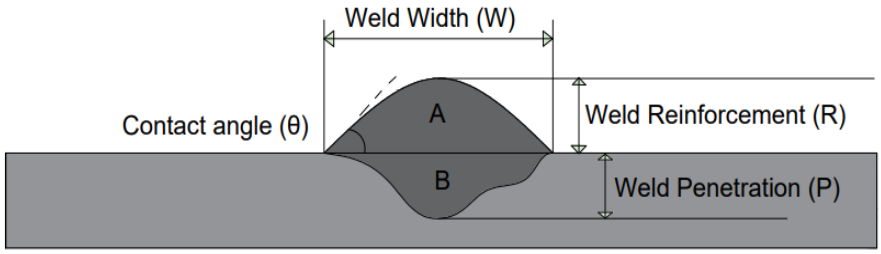

Figure 4.1 Weld bead geometry

The heat input during welding plays a significant role in forming welds on bead geometry. The heat input equation is given in equation (12) [Han et al., (2021)]. Weld penetration and reinforcement area were found with the help of Image J software.

$$\text{Heat input (H.I)} = (VxI)\,\eta/S \quad \ldots\ldots\ldots\ldots (12)$$

Where V= voltage (V),

I = current (A),

S = travel speed (mm/sec),

H.I = heat input (J/mm) and

η = thermal efficiency (%)

Selecting the suitable welding current and welding speed produces deeper weld penetration. Based on the thickness of the material, the welding speed is chosen for deeper weld penetration. The variation in heat input affects the width of the weld and penetration. Higher heat input increases the base material's melting, dilution percentage, and weld penetration. However, excess heat input greater than the required amount creates defects in the weld bead region. Appropriate heat is essential to produce sound weld beads [Yang et al., 2013]. In the CMT welding process, heat input is regulated by the rapid retraction of the filler wire during the short-circuit metal transfer phase.

4.1.2 Optimization of welding parameters

Many preliminary weld bead trials were performed to fix the upper and lower limits of welding parameters. The Taguchi L_9 technique was applied for weld-on-bead experiments to optimize input parameters. Further, the CRITIC-ROV multicriteria decision-making technique is utilized to identify input parameters for combined responses of weld-on-bead geometry of the A2099-T86 alloy using CMT and pulse MIG welding processes. Table 4.1 displays the chosen welding parameters and their responses according to the Taguchi L_9 orthogonal array.

Table 4.1 Welding parameters and their responses

Expt. No.	*I* (A)	*S* (mm/s)	*D* (mm)	CMT weld bead			Pulse MIG weld bead		
				Weld penetration (mm)	Dilution (%)	Heat input (J/mm)	Weld penetration (mm)	Dilution (%)	Heat input (J/mm)
1	150	6	4	3.58	56.28	374	5.0	54.65	416
2	150	8	6	2.96	61.12	280.5	3.0	56.23	312
3	150	10	8	3.74	66.62	224.4	5.86	71.21	249.6
4	165	6	8	3.40	60.08	429	0.61	46.31	481.8
5	165	8	4	3.31	56.51	321.8	1.2	47.37	359.7
6	165	10	6	4.69	72.35	257.4	4.2	64.56	287.8
7	180	6	6	4.86	62.30	402.5	5.25	65.22	501.8
8	180	8	8	4.16	57.12	363.6	3.0	31.69	406.8
9	180	10	4	6.46	84.99	290.9	4.0	52.38	325.4

For optimal input parameters, Taguchi's approach included computation of the (S/N) ratio and analysis of means. The decision matrix table for the CMT and pulse MIG welding processes is presented in Table 4.2. The weights of the three output responses were calculated using the steps of the CRITIC method explained in Section 3.4.3. The weld penetration and dilution are the beneficial criteria/output responses, as their maximum values are desired. However, heat input is a non-beneficial criterion/output response since its minimum value is preferred. The weights of the criteria/output responses are shown in Table 4.3. The heat input response weight is maximum, which is the most important, followed by weld penetration and dilution. The weights mentioned in Table 4.3 were used as inputs to the ROV methods.

Table 4.2 Decision matrix

	CMT weld bead			**Pulse MIG weld bead**		
Expt. No.	**Weld penetration (mm)**	**Dilution (%)**	**Heat input (J/mm)**	**Weld penetration (mm)**	**Dilution (%)**	**Heat input (J/mm)**
1	3.58	56.28	374.0	5.0	54.65	416
2	2.96	61.12	280.5	3.0	56.23	312
3	3.74	66.62	224.4	5.86	71.21	249.6
4	3.40	60.08	429.0	0.61	46.31	481.8
5	3.31	56.51	321.8	1.2	47.37	359.7
6	4.69	72.35	257.4	4.2	64.56	287.8
7	4.86	62.30	402.5	5.25	65.22	501.8
8	4.16	57.12	363.6	3.0	31.69	406.8
9	6.46	84.99	290.9	4.0	52.38	325.4

Table 4.3 Weights of the criteria/output responses

	Weight	
Output response	**CMT**	**Pulse MIG**
Weld penetration	0.3188	0.3226
Dilution	0.2162	0.2607
Heat input	0.4649	0.4167

Table 4.4 Normalized decision matrix

	CMT			Pulse MIG		
Expt. No.	**Weld penetration (mm)**	**Dilution (%)**	**Heat input (J/mm)**	**Weld penetration (mm)**	**Dilution (%)**	**Heat input (J/mm)**
1	0.1771	0.0000	0.2688	0.8362	0.5810	0.4317
2	0.0000	0.1686	0.7258	0.4552	0.6210	0.7869
3	0.2229	0.3602	1.0000	1.0000	1.0000	1.0000
4	0.1257	0.1324	0.0000	0.0000	0.3699	0.2070
5	0.1000	0.0080	0.5239	0.1124	0.3968	0.6240
6	0.4943	0.5597	0.8387	0.6838	0.8317	0.8695
7	0.5429	0.2097	0.1295	0.8552	0.9168	0.0000
8	0.3429	0.0293	0.3196	0.4552	0.0000	0.4631
9	1.0000	1.0000	0.6750	0.6457	0.5235	0.7411

The ranks of the experiments were derived. The decision matrix presented in Table 4.2 was normalized using Equations (6) and (7), which resulted from the normalized decision matrix in Table 4.4 for both welding processes. The best utility and worst utility were computed using Equations 8 and 9, respectively. The utility values of the experiments were ranked as per step 4, mentioned in section 3.4.4 of the ROV method. The utility values and rankings of the experiments for both the CMT and pulse MIG processes are detailed in Tables 4.5 and 4.6, respectively. According to Table 4.5, experiment number 9 holds the top rank, indicating that its set of input parameters is optimal for multiple responses in the CMT process. Similarly, Table 4.6 shows that experiment number 3 is ranked first, signifying that its parameters are the most effective for multiple responses in the pulse MIG process. However, these sets of input parameters may not necessarily be the optimal setting for optimum multiple responses. Hence, Taguchi's approach includes the computation of the S/N ratio and analysis of means.

Table 4.5 Ranks of experiments and signal to noise ratios for CMT process

Expt. No.	$U_{i,positive}$	$U_{i,negative}$	U_i	**Signal to noise ratio**	**Rank**
1.	0.0565	0.1250	0.0907	-20.8479	8
2.	0.0440	0.3374	0.1907	-14.3930	4
3.	0.1649	0.4649	0.3149	-10.0365	3
4.	0.0746	0.0000	0.0373	-28.5658	9
5.	0.0340	0.2436	0.1388	-17.1522	6
6.	0.3035	0.3899	0.3467	-9.2009	2
7.	0.2277	0.0602	0.1440	-16.8328	5
8.	0.1169	0.1486	0.1328	-17.5360	7
9.	0.5795	0.3138	0.4467	-6.9997	1

Table 4.6 Ranks of experiments and signal to noise ratios for Pulse MIG process

Expt. No.	$U_{i,positive}$	$U_{i,negative}$	U_i	Signal to noise ratio	Rank
1.	0.4327	0.1799	0.3063	-10.2771	5
2.	0.3210	0.3279	0.3244	-9.7784	4
3.	0.6030	0.4167	0.5098	-5.8520	1
4.	0.1037	0.0862	0.0950	-20.4455	9
5.	0.1475	0.2600	0.2037	-13.8202	7
6.	0.4538	0.3623	0.4081	-7.7847	2
7.	0.5330	0.0000	0.2665	-11.4861	6
8.	0.1469	0.1930	0.1699	-15.3961	8
9.	0.3551	0.3088	0.3320	-9.5772	3

The computation of the S/N ratio depends on the quality characteristic of the variable, whether it is lower, higher, or nominal. In this case, the quality characteristic of the variable, Ui, is higher and better as its maximum value is desired; therefore, the S/N ratio was computed using Equation (13).

$$(\mathrm{S/N})_i = -10log_{10}\frac{1}{n}\left(\sum_{r=1}^{n}\frac{1}{U_r^2}\right) \ldots\ldots\ldots\ldots (13)$$

The S/N ratio of the ith experiment is (S/N)i, where i denotes the experiment number, r represents the replication number, Ur indicates the utility value for rth replicate, and n means the number of replicates. The S/N ratios and weld bead responses of the CMT and pulse MIG are depicted in Table 4.7 and Table 4.8, respectively. The input parameter mean signal-to-noise ratio at each level was calculated. The best quality characteristics of input parameters represent the

maximum value of the S/N ratio. The optimum level of the input parameter is selected as the maximum S/N ratio. In addition, response graphs for the S/N ratio for CMT and pulse MIG are shown in Figures 4.2 and 4.3, respectively. According to Table 4.7 and Figure 4.2, the ideal input parameters for achieving the best multi-responses in the CMT process are $I_3S_3D_2$, which correspond to a current of 180 A, a welding speed of 10 mm/sec, and a CTWD of 6 mm.

Table 4.7 S/N ratio response table of CMT

Input parameter	**L_1**	**L_2**	**L_3**	**Δ = Max.-Min.**	**Rank**
Current (I)	-15.092	-18.306	-13.789	4.517	3
Welding speed (S)	-22.082	-16.360	-8.746	13.336	1
CTWD (D)	-15.000	-13.476	-18.713	5.237	2
Optimum setting parameters for CMT is $\boldsymbol{I_3S_3D_2}$					

Table 4.8 S/N ratio response table of Pulse MIG

Input parameter	**L_1**	**L_2**	**L_3**	**Δ = Max.-Min.**	**Rank**
Current (I)	-8.636	-14.017	-12.153	5.381	2
Welding speed (S)	-14.070	-12.998	-7.738	6.332	1
CTWD (D)	-11.225	-9.683	-13.898	4.215	3
Optimum setting parameters is $\boldsymbol{I_1S_3D_2}$					

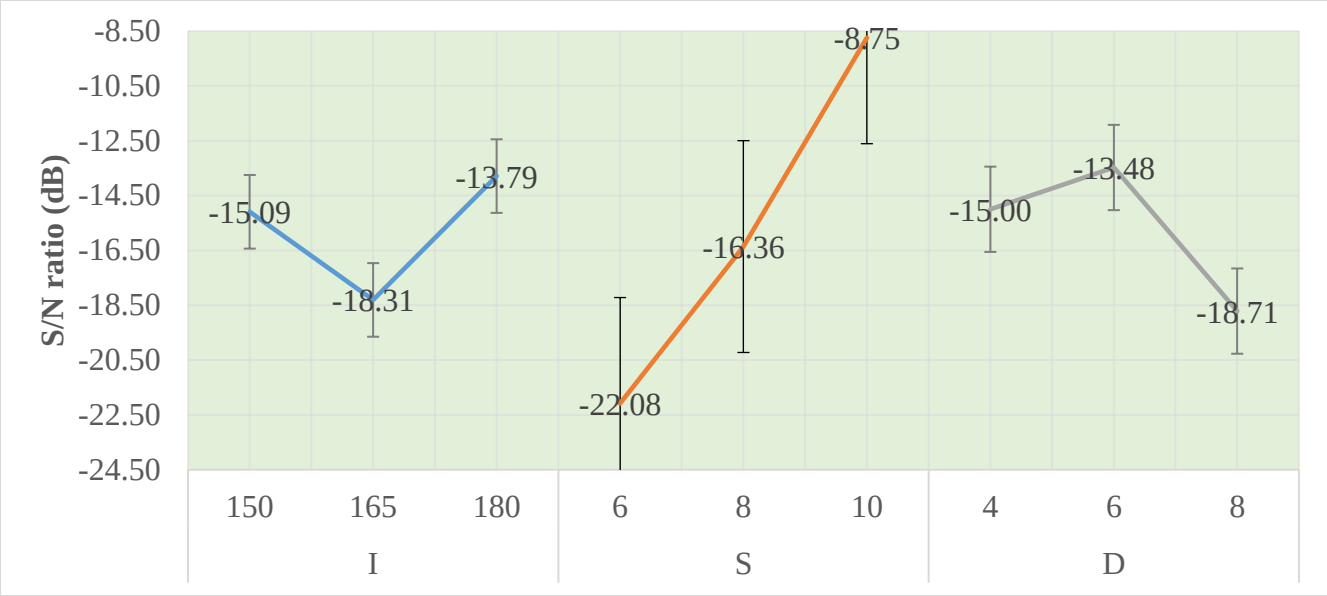

Figure 4.2 Response graph for S/N ratio for CMT welding

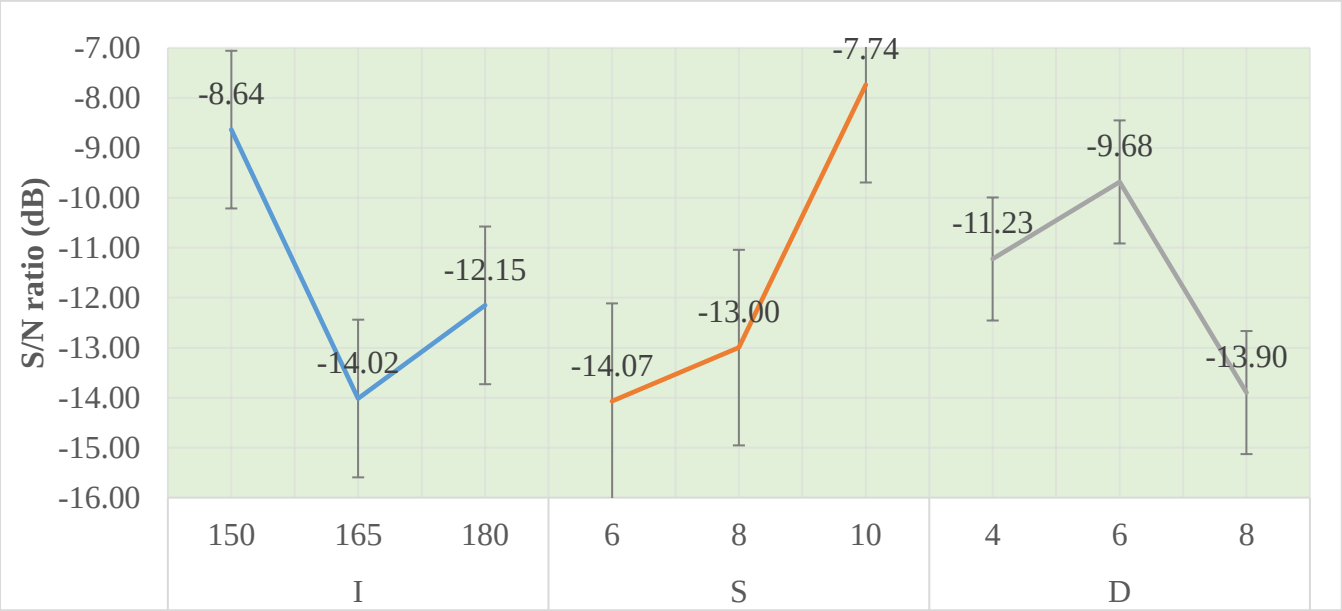

Figure 4.3 Response graph for S/N ratio for Pulse MIG welding

Likewise, Table 4.8 and Figure 4.3 indicate that for the pulse MIG process, the optimal input parameters for the best multi-responses are $I_1S_3D_2$, with a current of 150 A, a welding speed of 10 mm/sec, and a CTWD of 6 mm. A high current is required for CMT; for pulse MIG, a low

current is desired. CMT welding is based on low heat input compared to pulse MIG welding. With CMT welding, one-fourth of the total time was used in a short-circuit phase, which results in less energy consumption [Selvamani et al., 2022].

4.1.3 ANOVA for all the multi-responses

Analysis of variance (ANOVA) for the S/N ratio was performed at a 5% significance level, i.e., $\alpha = 0.05$, to determine which input process parameter significantly affects the multi-responses. ANOVA is a well-established statistical method extensively used by researchers, and its detailed procedure is available in the literature [Koilraj et al., 2012]. The ANOVA results for CMT and pulse MIG are presented in Tables 4.9 and 4.10, respectively. It can be perceived from Table 4.9 that within the reconnoitred range of the input parameters of the CMT welding process, only welding speed (S) significantly affects the multiple output responses taken simultaneously as its p-value is less than 0.05.

Table 4.9 ANOVA results for CMT

Source of variation	**Sum of square (S.S.)**	**Degrees of freedom (df)**	**Mean square (M.S.)**	**F-ratio**	**p-value**	**% Contribution**
I	32.428	2	16.214	5.45	0.155	9.25
S	268.582	2	134.291	45.12	0.022	76.63
D	43.538	2	21.769	7.31	0.120	12.42
Error	5.953	2	2.977	-	-	1.70
Total	350.502	8	-	-	-	100

Table 4.10 ANOVA results for Pulse MIG

Source of variation	**Sum of square (*S.S.*)**	**Degrees of freedom (*df*)**	**Mean square (*M.S.*)**	***F*-ratio**	***p*-value**	**% Contribution**
I	44.80	2	22.400	3.35	0.230	29.02
S	68.91	2	34.453	5.16	0.162	44.65
D	27.29	2	13.644	2.04	0.329	17.68
Error	13.36	2	6.679	-	-	8.66
Total	154.35	8	-	-	-	100

Nevertheless, according to the percentage contribution analysis, welding speed (S) is the most influential parameter, followed by contact tip-to-work distance (CTWD) and current (I). In contrast, Table 4.10 shows that, within the examined range of pulse MIG welding parameters, none were statistically significant, as all p-values exceed 0.05. However, based on % contribution values, welding speed (S) is the essential input parameter, followed by current (I) and CTWD. (D).

4.2 CONFIRMATION TEST

The last stage of Taguchi's analysis is the confirmation test, which is used to validate the optimization results obtained in the study. This procedure compares the predicted signal-to-noise ratio value at the optimum combination with the experimental value of the expected value at the optimum combination. Equation (14), as suggested by Taguchi, is used.

$$\eta_{pred} = \eta_{avg} + \sum_{k=1}^{n}(\eta_k - \eta_{avg}) \quad \text{..... (14)}$$

Where, η_{avg} be the average signal-to-noise ratio for input variable k at optimum level. The value of k ranges from 1 to the total number of input variables (n). Further, to obtain the experimental value of the signal-to-noise ratio at the optimum combination, a confirmation experiment is performed by setting the input parameters as an optimal combination. However, in this study, the experimental values of the S/N ratio cannot be directly computed from the experimental results. Hence, a regression model is developed to calculate the observed S/N ratio based on the output response. To confirm the predicted model, the weld-on-bead experiments were conducted at optimized CMT and pulse MIG welding values, as shown in Figure 4.4. The samples were free from weld defects and showed good weld bead quality. The actual and predicted values of output responses at optimized parameters for the CMT and MIG-Pulse processes are presented in Table 4.11. The actual and predicted values are within the 5% error range, which shows the designed model is accurate.

Table 4.11 Verification of experimental results

Weld process	**I (A)**	**S (mm/s)**	**D (mm)**	**Weld Penetration (mm)**			**Dilution (%)**			**Heat input (J/mm)**		
				A. V	**P. V**	**% E**	**A. V**	**P. V**	**% E**	**A. V**	**P. V**	**% E**
CMT	180	10	6	5.8	5.65	2.65	78.12	77.21	1.17	252.72	250.12	1.03
Pulse MIG	150	10	6	6.4	6.2	3.2	78.21	77.14	1.38	241.2	240.7	0.20
% E $= \frac{\text{Actual Value} - \text{Predicted value}}{\text{Predicted value}}$, where A.V= Actual value, P.V= Predicted value, %E= Percentage error												

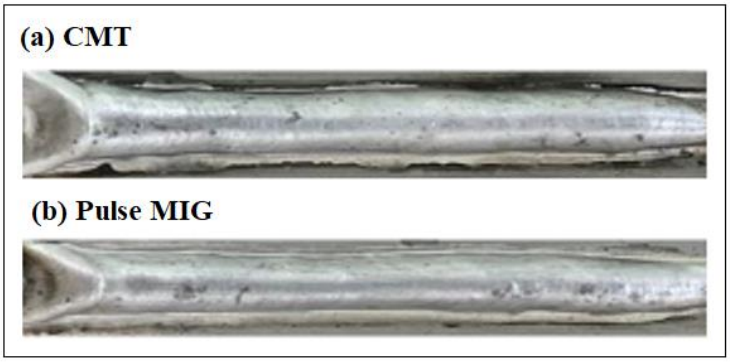

Figure 4.4 Weld bead images prepared at optimized process parameters

4.2.1 For CMT process

The predicted value of the signal-to-noise ratio for the CMT process was calculated using Equation (14), yielding a value of -4.552 dB. An experiment was then conducted using the optimal input parameters: 180 A current, 10 mm/sec welding speed, and 6 mm CTWD. The resulting output measurements were recorded, with weld penetration at 5.8 mm, dilution at 78.12%, and heat input at 252.72 J/mm. Subsequently, a regression between the S/N ratio and output responses was developed with R2 values of 95.65%, as given in Equation (15).

$$\eta_{exp} = 13.543 + 5.115 \times Weld\ Penetration - 0.314 \times Dilution - 0.093 \times Heat\ Input$$

……(15)

The experimental value of the S/N ratio at the optimal combination was established to be -4.673. Since the experimental and predicted values of the S/N ratio at the optimum combination are in close agreement, i.e., percentage error = 2.65%, the study results are validated.

4.2.2 For pulse MIG welding

The predicted signal-to-noise ratio value for the pulse MIG is computed using Equation (14) and is found to be -2.853 dB. Additionally, an experiment was conducted using the optimal input

parameters—150 A of current, 10 mm/sec welding speed, and 6 mm CTWD. The output responses were then measured, yielding experimental values of 6.4 mm for weld penetration, 78.21% for dilution, and 241.2 J/mm for heat input. Subsequently, a regression between the S/N ratio and output responses was developed with R2 values of 94.85%, as given in Equation (16).

$$\eta_{exp} = -10.373 + 1.333 \times Weld\ Penetration + 0.067 \times Dilution - 0.026 \times Heat\ Input$$

…….(16)

The experimental value of the S/N ratio at the optimal combination was found to be -2.944. Since the experimental and predicted values of the S/N ratio at the optimum combination are in close agreement, i.e., percentage error = 3.2%, the study's results are validated.

4.3 WELD BEAD MACROSTRUCTURE

A cross-sectional image of the weldment's macrostructure displays a number of significant features, including the base material (BM), reinforcement, penetration depth, pore distribution, and the HAZ. Penetration depth and reinforcement both were found out with the help of Image J software. Macro-images of the cross-sections of CMT and pulse MIG welds are shown in Figures 4.5 and 4.6, respectively. These images show that there are more pores in the pulse MIG weld bead than in the CMT weld bead. These pores are formed due to gas entrapment during the fusion process. The high heat inputs involved in pulse MIG welding make aluminum alloys particularly susceptible to gas solubility, primarily hydrogen, which results in porosity. Besides heat input, the alloying elements significantly influence hydrogen solubility. For example, Mg in aluminum alloys enhances hydrogen affinity, as the interactions between Mg and hydrogen atoms are stronger compared to those between aluminum and hydrogen atoms [Anyalebechi, 1995].

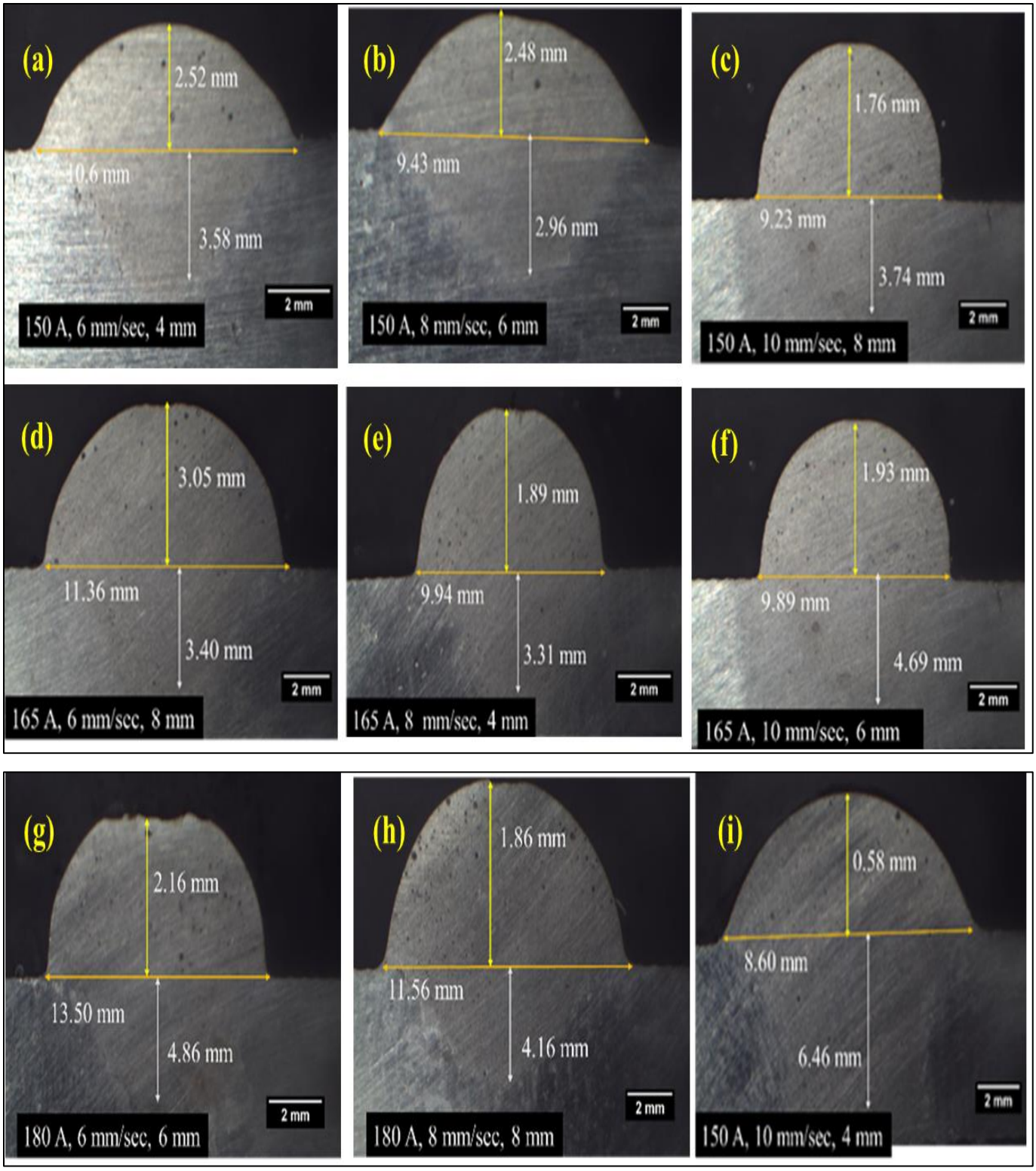

Figure 4.5 Macro-images of CMT weld bead

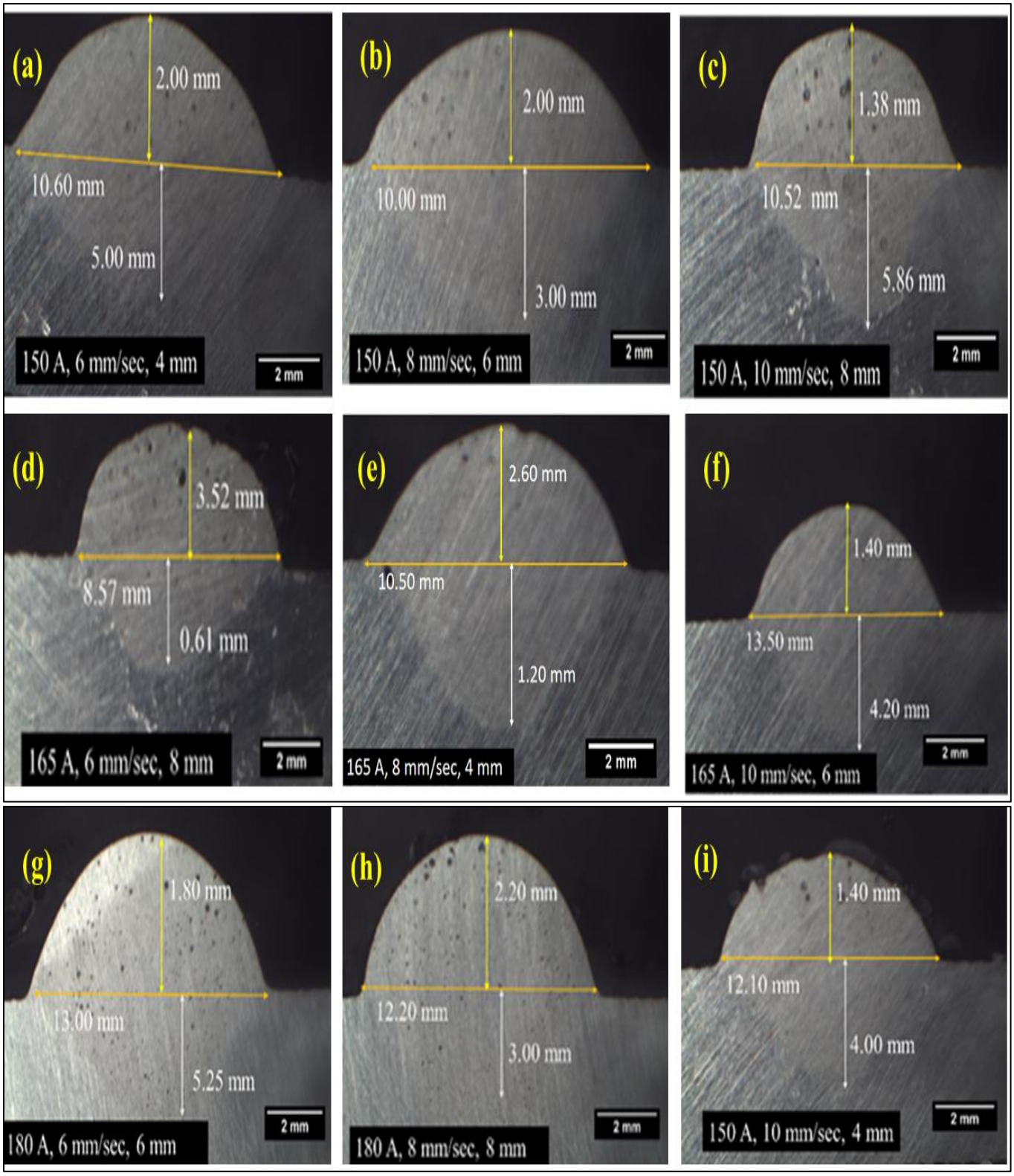

Figure 4.6 Macro-images of Pulse MIG weld bead

The CMT and pulse MIG weld bead experiments were performed at the same set of welding parameters: current (150 A, 165 A, and 180 A), welding speed (6, 8, and 10 mm/sec), and CTWD (4, 6, and 8 mm), and their results are presented in Table 4.1. The weld bead images of CMT and pulse MIG are shown in Figure 3.11. From this table, it can be revealed that crack formation occurs in pulse MIG at a heat input of 501.8 J/mm (180 A-6 mm/sec-6 mm), while no crack was seen in CMT at the same welding parameter and heat input recorded of 402.5 J/mm. This may be attributed to the fact that pulse MIG is a high heat input process and CMT is a low heat input process. It was also noticed that the thickness of the aluminium oxide (Al_2O_3) layer is higher in pulse MIG as compared to the CMT process. The aluminium oxide layer is basically a white layer found in the nearby regions of weld bead. Due to arc heat, a small amount of black dirt was observed at the starting end of the weld bead in CMT and pulse MIG at 180 A. This back dirt is basically magnesium oxide (MgO). The evaluation of dilution (%) is given in equation 11 (Koli et al. 2019).

4.4 EFFECT OF WELD PROCESS PARAMETERS

4.4.1 Effect of CTWD on weld penetration, dilution and heat input.

In CMT and pulse MIG welding processes, the term "contact tip to workpiece distance" refers to the measurement of the space between the contact tip and the surface of the workpiece to be welded, as illustrated in Figure 4.7. In the experiment, CTWD varied by 4, 6, and 8 mm, respectively, as shown in Table 3.10. The bead appearance varied with different values of CTWD, as shown in Figure 3.11. It was revealed that the bead appearance was not continuous and smooth when CTWD was 4 mm. A more continuous bead appearance was found when CTWD was 6 mm. When CTWD was 8 mm, the bead appearance turned out to be discontinuous and irregular, with some spatter found around it. Apart from the weld bead appearance, the bead size also altered with the CTWD increasing. The reinforcement height decreased gradually when the CTWD increased from 4 to 8 mm (Figure 4.5a to c). The bead width at CTWD of 4 mm was larger than CTWD of 6 or 8 mm (Figure 4.5a).

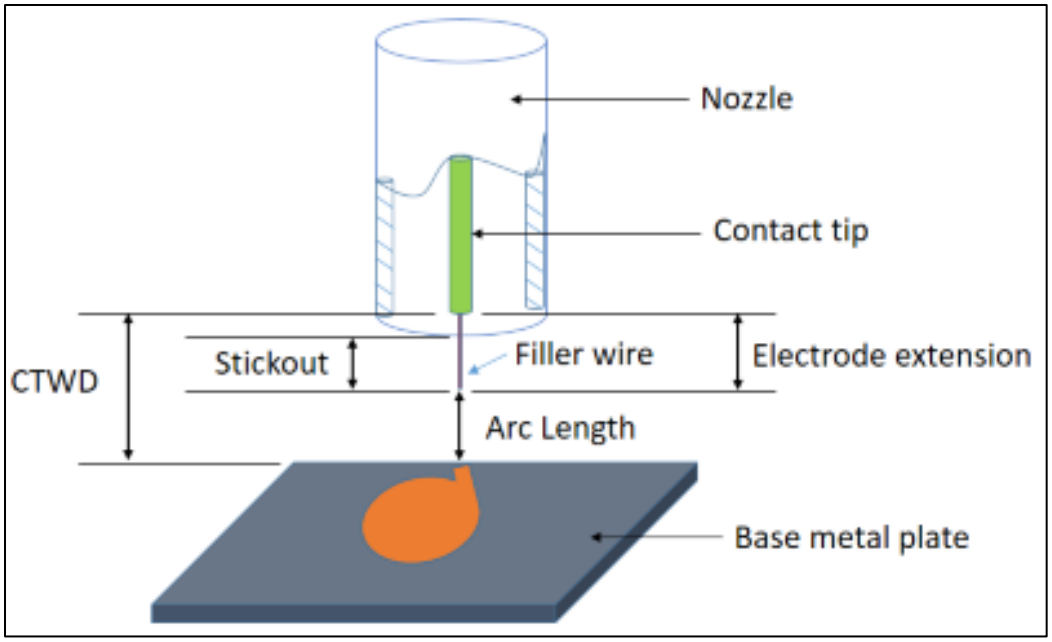

Figure 4.7 Schematic illustration of CTWD in welding

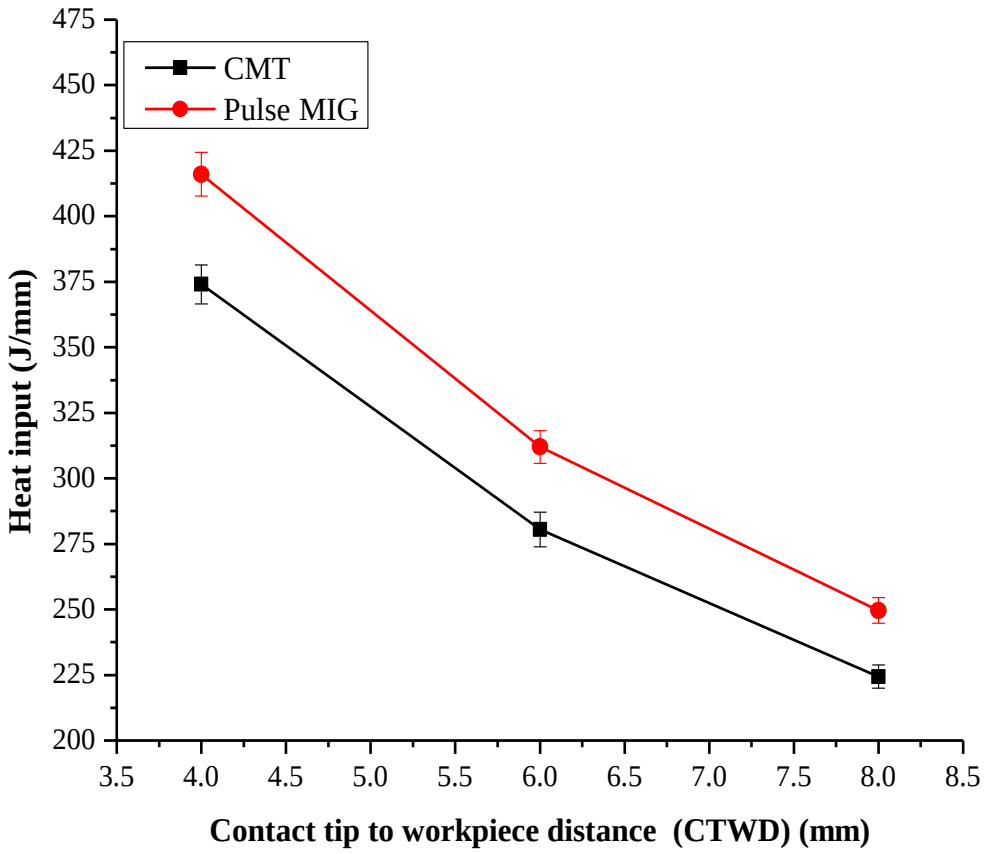

Figure 4.8 Effect of CTWD on heat input @ 150 A

The weld penetration reached a maximum value at the CTWD of 8 mm (Figure 4.5c) and then decreased with the decrease of the CTWD from 8 mm to 6 mm. At 4 mm CTWD, weld penetration, dilution, and heat input were found to be 3.58 mm (Figure 4.5a), 56.28 %, and 374 J/mm in the case of CMT, while at 5 mm (Figure 4.6a), 54.65% and 416 J/mm in the case of pulse MIG, respectively, at a constant current of 150 A. Figure 4.8 illustrates that increasing the CTWD from 6 to 8 mm resulted in a 10% reduction in heat input for CMT, a 4-36% decrease in weld penetration, and a 6.44% lower dilution compared to pulse MIG welding. This is due to the fact that any increase in the value of CTWD can lower the amperage and result in poor penetration. From these observations, we can say that contact tip-to-work plate distance had a significant influence on weld bead appearance, bead size, and heat input.

4.4.2 Effect of welding speed on weld penetration, dilution, and heat input

Weld bead production is directly correlated with both heat input and dilution. The amount of dilution rises as a result of more substrate metal melting when the heat input increases. In the experiment, welding speed varied with 6, 8, and 10 mm/sec. At 6 mm/sec of welding speed, weld penetration, dilution, and heat input were found to be 4.86 mm (Figure 4.5g), 62.30 %, and 402.5 J/mm in the case of CMT, while 5.25 mm (Figure 4.6g), 65.22 %, and 501.8 J/mm in the case of pulse MIG, respectively, at a constant current of 180 A. It was observed that the CMT heat input was 19.78% lesser, the weld penetration was 7.42% smaller, and the dilution was 4.47% lesser than the pulse MIG welding. There is approximately 4.47 percent less dilution during the CMT process than with pulse MIG due to the wire's oscillations. This wire's oscillating action keeps the arc length consistent and improves dilution control. Figure 4.9 illustrates how welding speed affects heat input in both the CMT and the pulse MIG processes at a constant current of 180 A.

Both the CMT and the pulse MIG processes showed a decrease in heat input with increasing welding speed. The maximum and minimum heat input recorded in CMT were 402.5 J/mm and 290.9 J/mm, while 501.8 J/mm and 325.4 J/mm were recorded in pulse MIG at welding speeds of 6 mm/sec and 10 mm/sec, respectively. This is due to the inversely proportional relationship between heat input and welding speed. The weld width in CMT is found to be 13.50 mm, 11.56 mm, and 8.60 mm at the welding speeds of 6, 8, and 10 mm/sec, respectively, as depicted in Figure 4.5g to Figure 4.5i. With a constant current, an increase in welding speed leads to a reduction in weld width because the CMT process provides less heat input.

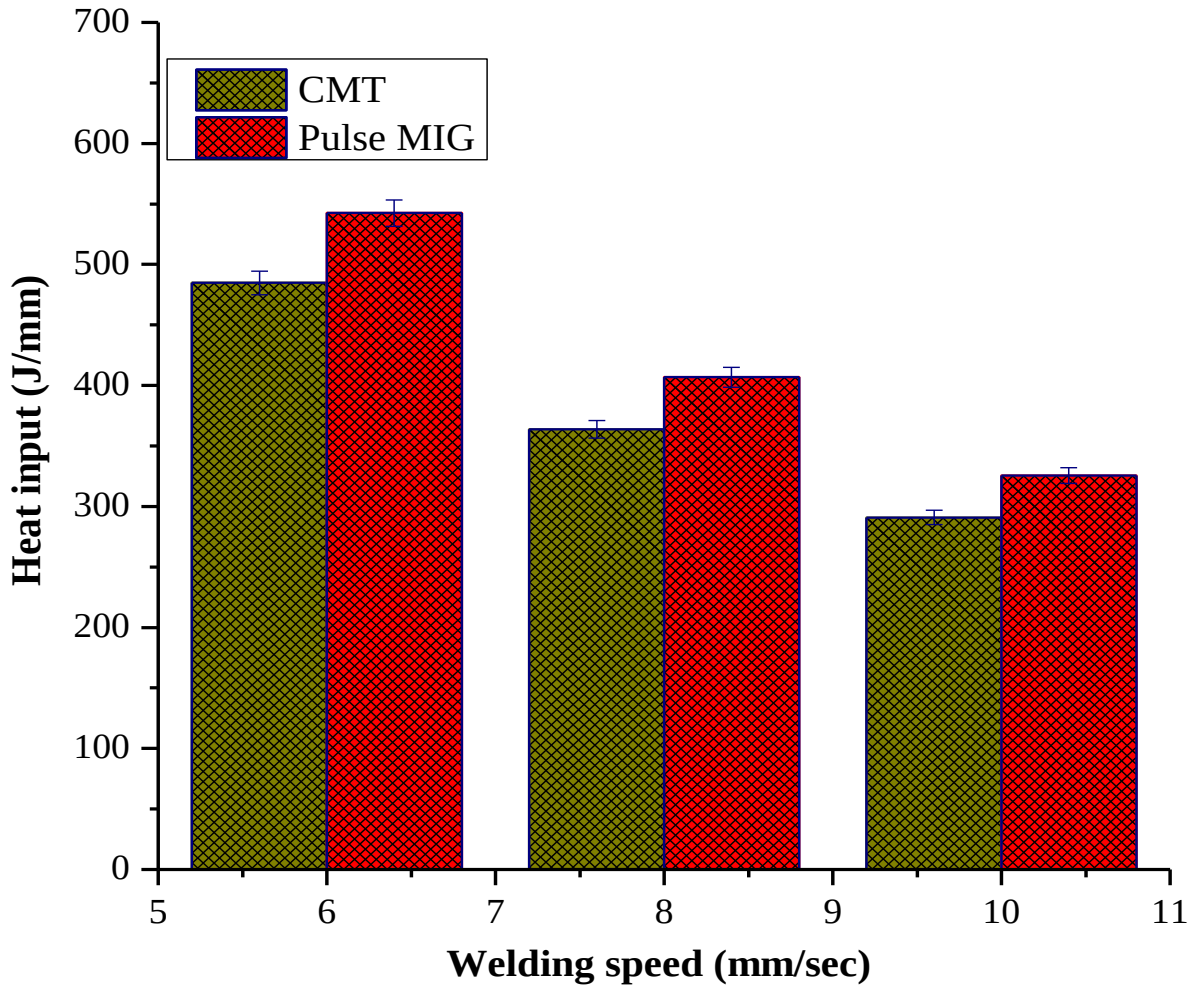

Figure 4.9 Effect of welding speed on heat input @ 180 A

4.4.3 Effect of welding current on weld geometry and dilution

Dilution and welding current are directly related; an increase in current results in more metal melting, which raises the dilution percentage. The dilution is defined as the ratio of the weld penetration area to the total weld area, which encompasses both penetration and reinforcement, as expressed in equation (11). Figure 4.10 shows the effect of welding current on dilution between CMT and pulse MIG at a constant CTWD of 4 mm. Heat input is an important response, has an inversely proportional relationship with welding speed, and varies directly with the welding current, as shown in equation (12). High welding currents can produce high heat input, causing more material to melt and resulting in an increase in dilution percentage. As can be perceived from Figure 4.10, dilution is found to be 56.28% and 54.5% in CMT and pulse MIG, respectively, at a welding current of 150 A and CTWD of 4 mm.

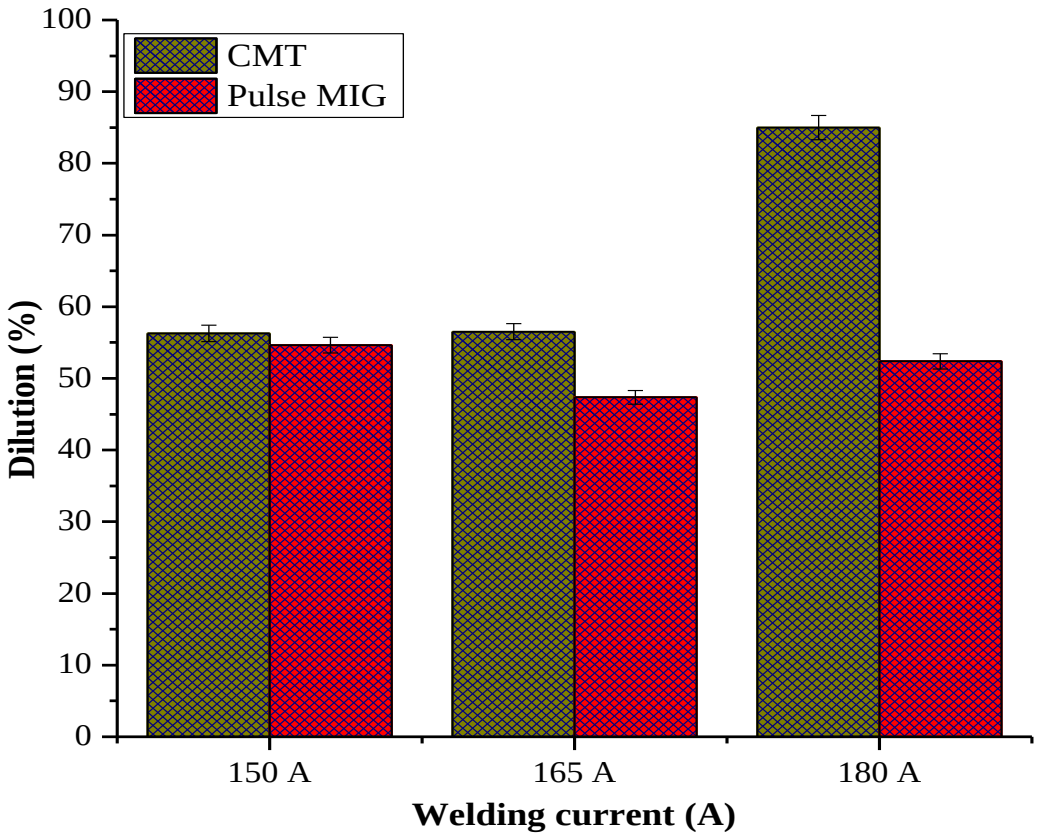

Figure 4.10 Effect of welding current on dilution

But when welding current rises from 165 A to 180 A, dilution increases from 56.51% to 84.99% in CMT and 47.37% to 52.38% in pulse MIG, respectively. An increase in current during welding can increase the weld penetration due to more droplet detachments. At a welding current of 150 A and CTWD of 4 mm, weld penetration is found to be 3.58 mm (Figure 4.5a) and 5.00 mm (Figure 4.6a) in CMT and pulse MIG, respectively. As the current rises from 165 A to 180 A, the penetration is recorded at 3.31 mm (Figure 4.5e) and 6.46 mm (Figure 4.5i) in CMT and 1.20 mm (Figure 4.6e) and 4.00 mm (Figure 4.6i) in pulse MIG. By increasing the welding current from 165 A to 180 A, the weld penetration rises 48.76% in CMT and 70% in pulse MIG. In comparison to CMT, pulse MIG shows 30.34% more weld penetration due to the high heat input process.

4.5 SUMMARY

This chapter discusses the weld bead geometry produced by two different welding processes: CMT and pulse MIG. The optimization of weld-bead experiments employs a multicriteria decision-making approach using CRITIC and ROV-based Taguchi methods, focusing on three responses: weld penetration, dilution, and heat input. This combined methodology provides a systematic and objective framework for analysis, which is validated by experimental results. Key findings reveal that welding speed is the most significant parameter in both CMT and pulse MIG processes, followed by current and CTWD. Response graphs for the S/N ratio are generated for both welding methods to identify optimal input parameters for achieving the best multiple responses. Additionally, macro-images of the weld beads for all design combinations are presented, along with an analysis of how welding speed, current, and CTWD affect penetration, dilution, and heat input across various welding parameters.

CHAPTER 5: RESULTS AND DISCUSSION ON FABRICATION OF CMT WELDED JOINT

5.1 INTRODUCTION

The butt joining of AA2099-T86 using ER4047 wire was performed across various welding parameter settings, as illustrated in Figure 3.12. It is evident that alterations in these parameters affect the geometry of the weld bead. Consequently, this leads to variations in the dimensions of weld reinforcement (R), weld width (W), and weld penetration (P), as shown in Figure 5.1.

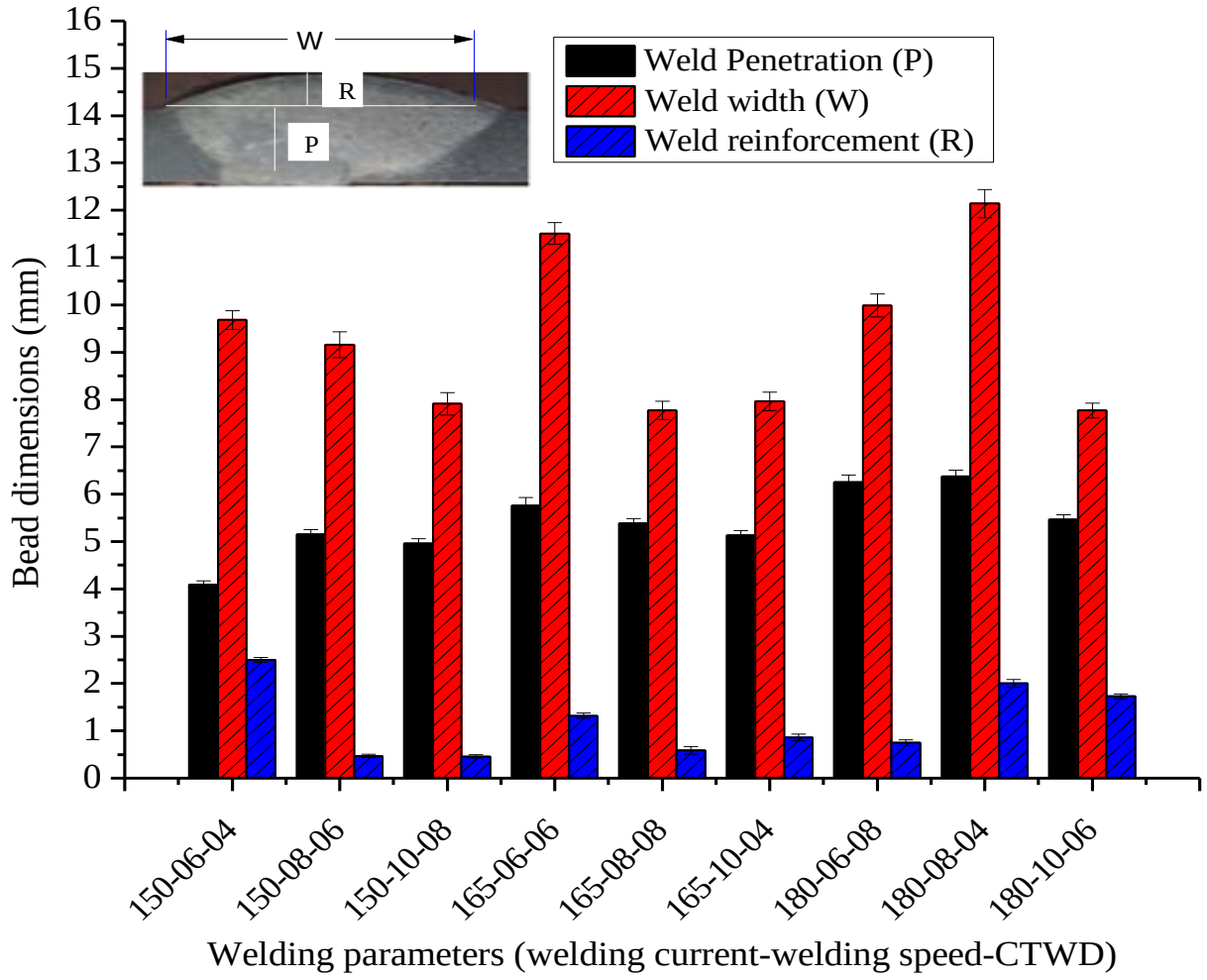

Figure 5.1 Bead dimensions of the welded joint

Using a vision inspection machine, the measured dimensions were confirmed to be within specified limits: weld width ranged from 7.7 mm to 12.14 mm, penetration depth varied between 4.09 mm and 6.38 mm, and reinforcement height was between 0.46 mm and 2.50 mm. In the CMT welding, a discernible correlation is evident: both weld width and penetration depth exhibit an upward trajectory in tandem with escalating heat input levels. This phenomenon is intrinsically linked to an enhanced arc-substrate interaction; as heat input intensifies, a greater volume of substrate material interfaces with the welding arc, consequently engendering increased width dimensions and more profound penetration depths. The weld reinforcement exhibits an upward trend, ranging between 0.46 mm and 2.50 mm. With an increase in heat input from 224.4 J/mm to 429 J/mm, the weld reinforcement height rises from 0.46 mm to 1.32 mm. Higher current values lead to deeper penetration and wider weld width due to the elevated heat input. A heat input of 402.5 J/mm (180 A, 8 mm/s, 4 mm) results in the deepest weld penetration of 6.38 mm and the widest weld width of 12.14 mm.

5.2 OPTIMIZATION OF PROCESS PARAMETERS FOR CMT WELDED JOINTS

5.2.1 Introduction

Various optimization and modeling techniques have been utilized to identify the optimal CMT welding parameters. Several authors have investigated that the combination of Response Surface Methodology (RSM) with Grey Relational Analysis (GRA) and Principal Component Analysis (PCA)—forming a hybrid model—produces better results with increased accuracy. Kumaran et al. (2020) investigated the mechanical properties of AA7475 alloy butt welded by pulsed CMT process and normal CMT process using ER5356 and ER4043 filler wires. The joint welded by the pulse CMT process with ER5356 filler wire has higher mechanical properties than the normal

CMT process due to more strengthening in the weld region. Xiang et al. (2023) found that the hydrogen percentage in the casting determines the porosity and distribution of pore formation during the CMT + pulse mode welding of the AA6082/A360 dissimilar joint. Xu et al. 2022 utilized the CMT cycle step welding method to weld Cu and AA5052 alloy using Al-12Si as a filler wire in diverse joint structures. The strength of the welded joint improved because of the advanced automation, precise control over droplet size, and reduced heat input. Nalajala et al. (2022) analyzed the effect of metal transfer characteristics in the CMT-Pulse process on a weld-on bead geometry of AA1050 alloy using $AlSi_{12}$ and $AlSi_5$ filler wires.

5.2.2 Select the feasible input welding parameters

After conducting numerous preliminary trials and optimizing the process parameters through weld bead on plate investigations, the range of selected CMT butt weld joint process parameters was depicted in Table 5.1. The determination of upper and lower limits for these parameters was guided by the evaluation of weld bead appearance and the resultant weld joint strength.

Table 5.1 Welding input parameters and their levels CMT welded joints

Parameters	**Symbol**	**Unit**	**L_1**	**L_2**	**L_3**
Welding current	(I)	A	150	165	180
Welding speed	(S)	mm/s	6	8	10
CTWD	(D)	mm	4	6	8

5.2.3 Welding parameter optimization

Three factors each of three levels, the Taguchi L_9 design matrix, was used for conducting the experiments, as this design matrix can give better optimization results by using a minimum

number of runs [Agrawal et al., 2020; Ghosh et al., 2016]. Test results are presented in Table 5.2 along with the signal-to-noise (S/N) ratio. The Minitab software is configured with a "larger the better" criterion to achieve the optimal values for the output responses. The highest value of the S/N ratio reflects the most optimal combination of input parameters, with the peak values of these parameters aligning with the maximum S/N ratio. For achieving maximum tensile strength and micro-hardness, the ideal input parameters are 180 A welding current, 6 mm/sec welding speed, and 4 mm CTWD, denoted as $WC_3WS_1CTWD_1$.

Table 5.2 Welding parameters as per design matrix and their results

S. No.	Welding current (A)	Welding speed (mm/s)	CTWD (mm)	Tensile strength (MPa)	Micro-hardness (HV)	Heat Input (J/mm)	Joint Efficiency (%)	S/N Ratio
1	150	6	4	250	98.65	374	81.69	41.7211
2	150	8	6	202	97	280.5	66.01	44.5245
3	150	10	8	200	95	224.4	65.36	41.4547
4	165	6	6	263	106.4	429	85.95	43.1417
5	165	8	8	228	110.11	321.75	74.5	44.3445
6	165	10	4	252	94.33	257.4	82.35	44.4114
7	180	6	8	296	121.75	484.8	96.73	43.7407
8	180	8	4	298	110.8	363.6	97.39	45.4175
9	180	10	6	262	115.37	290.88	85.62	43.1417

Table 5.3 Results of the ANOVA test for tensile strength

Source	DOF	Adj. SS	Adj. MS	F-Value	P-Value	% Contribution
WC	2	7033.6	3516.78	105.15	0.009	75.29
WS	2	1729.6	864.78	25.86	0.037	13.32
CTWD	2	1219.6	609.78	18.23	0.042	9.22
Error	2	66.9	33.44			2.17
Total	8	10049.6				100

Modal Summary

S	R-sq	R-sq(adj)	R-sq(pred)
5.78312	99.33%	97.34%	86.52%

Table 5.4 Results of the ANOVA test for micro-hardness

Source	DOF	Adj. SS	Adj. MS	F-Value	P-Value	% Contribution
WC	2	562.87	281.43	18.95	0.001	77.33
WS	2	83.23	41.61	2.8	0.002	12.32
CTWD	2	92.27	46.14	3.11	0.035	8.22
Error	2	29.7	14.85			2.13
Total	8	768.06				100

Modal Summary

S	R-sq	R-sq(adj)	R-sq(pred)
3.85325	96.13%	84.54%	21.71%

Figures 5.2(a) and 5.2(b) are used for illustrating the graphs of S/N ratios for tensile strength and microhardness. From Figure 5.2 (a), it can be inferred that the weld joint produced at 6 mm/s welding speed, 4 mm CTWD, and 180 A of current provides excellent tensile strength. From

Figure 5.2 (b), it can be inferred that the weld joint produced at 6 mm/s welding speed, 4 mm CTWD, and 180 A of current provides excellent microhardness. An analysis of variance (ANOVA) was performed on the welded samples to identify the parameters significantly affecting the output responses at a 0.05 significance level. Table 5.3 shows the results of the ANOVA for tensile strength, detailing the percentage contributions for input parameters. The most influential factor is welding current, accounting for 75.63%, followed by welding speed and CTWD. Results of the ANOVA test for micro-hardness are shown in Table 5.4, which illustrates the percentage contribution of input parameters to micro-hardness, revealing that welding current is the dominat input parameter, contributing 77.33%. Among the experimental samples in Table 5.2, Sample 8 (180A-8mm/s-4mm) exhibits the highest S/N ratio of 45.4175. Furthermore, the optimal parameter combination (180A-6mm/sec-4mm) yields S/N of 45.5301.

5.2.4 Confirmation test

Experiments were conducted to confirm the empirical correlation among selected parameters. Two experiments were carried out using identical experimental settings with process parameters optimized to their ideal values to check the adequacy of the model. The validation test outcomes are presented in Table 5.5. These results closely align with the predicted values, affirming the accuracy of the developed model. An improvement of 0.1137 is found in the signal-to-noise, which is very close to the value of the predicted test results.

Table 5.5 Conformity test results

Test details		Optimal input parameters	
	Initial condition	Predicted	Experiment
Level	$WC_3WS_2CTWD_1$	$WC_3WS_1CTWD_1$	$WC_3WS_1CTWD_1$
Tensile strength	298	294	302
Microhardness	110.8	116.5	118
S/N ratio	45.4175	45.5301	45.5312

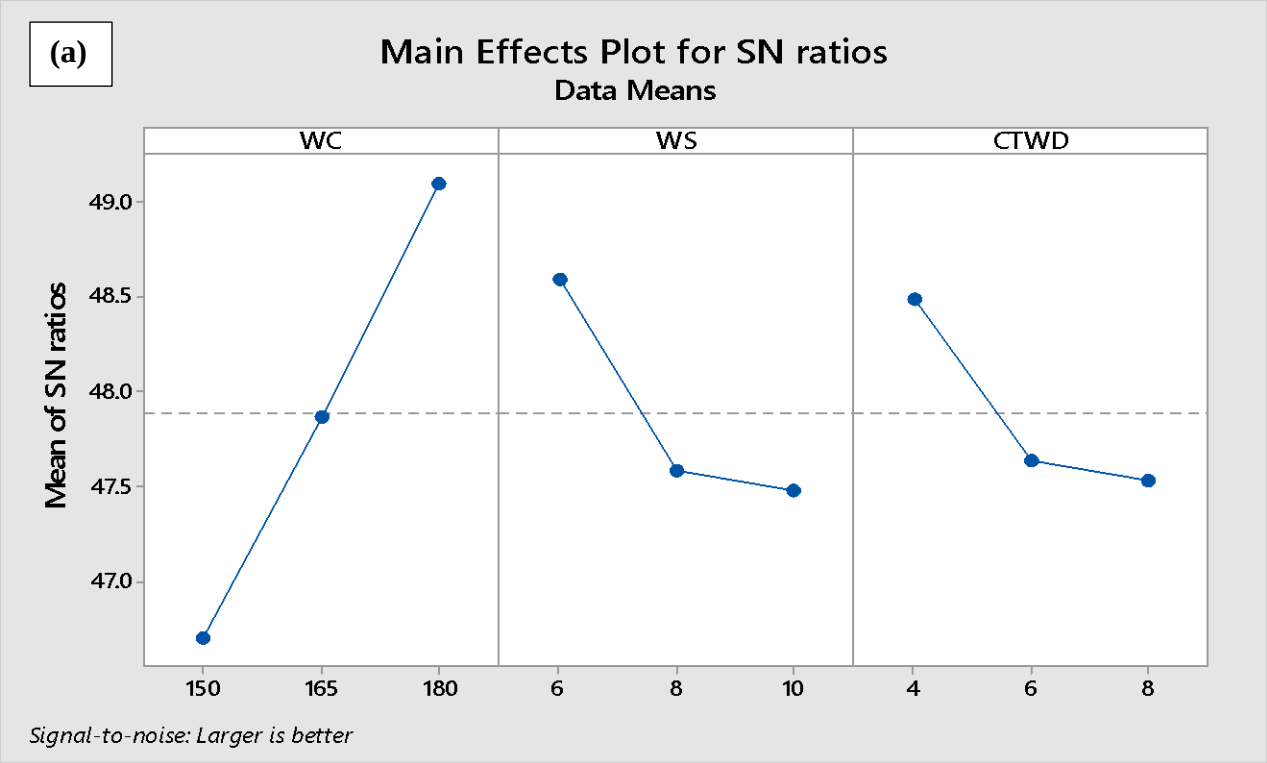

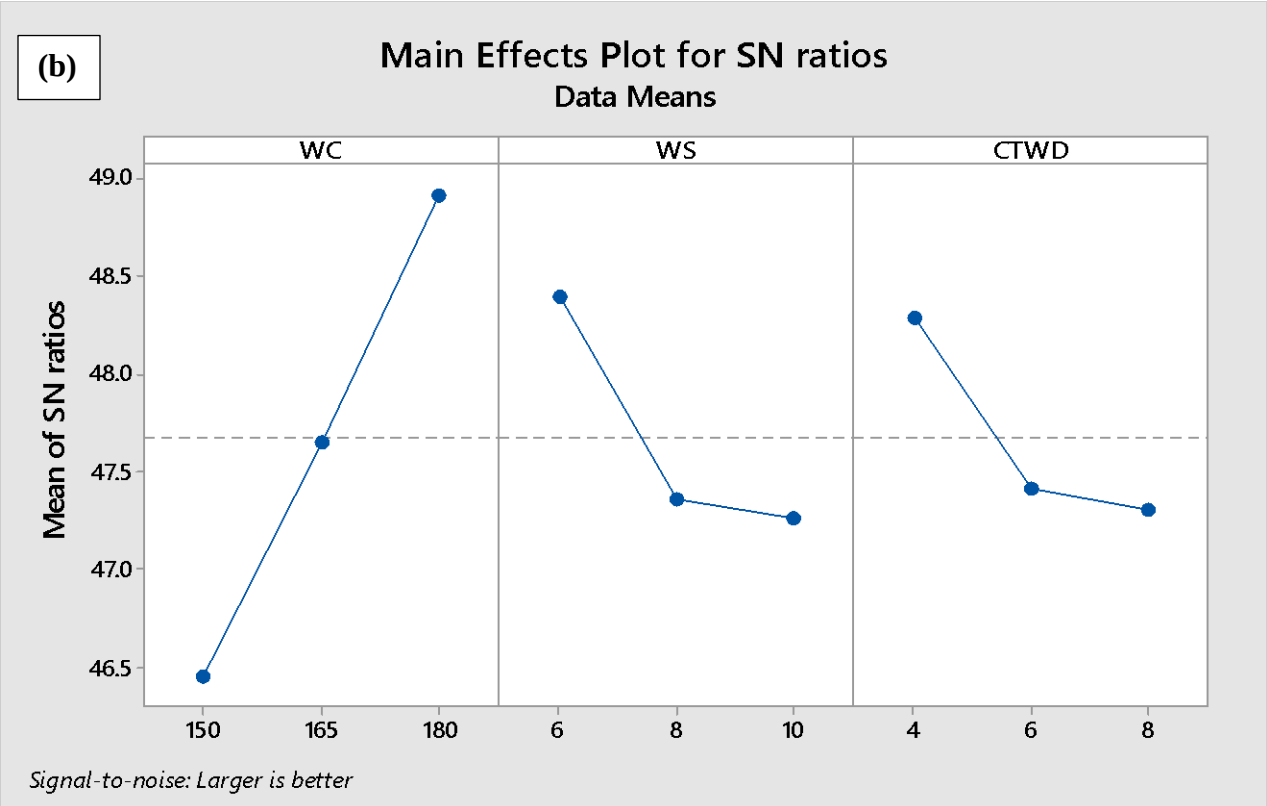

Figure 5.2 The main effects for Signal-to-Noise ratios: (a) for tensile strength and (b) for micro-hardness

5.3 MICROSTRUCTURE

Figure 5.4 shows microstructural pictures of the welded sample from different locations: the base metal zone, the weld bead zone, the interface, and the HAZ itself. The temperature during welding decides the type of grain formation in the weld joint [Cai et al., 2022]. During CMT welding, the filler wire undergoes fusion with the base metal, as illustrated in Figure 5.4(a). Figure 5.4(b) shows a clearly defined and sharp interface within the microstructural region of the weld joint. The grain size in HAZ has increased due to material softening, as illustrated in Figure 5.4(d), revealing an elongated dendritic grain structure in this area. The amount of gas flow rate during welding is also a measure of dendritic grain structure [Chen et al., (2024); Deng et al., (2022)]. Guo et al. (2021) reported that the resistance of recrystallization in the AA2099 alloy leads to the development of grains.

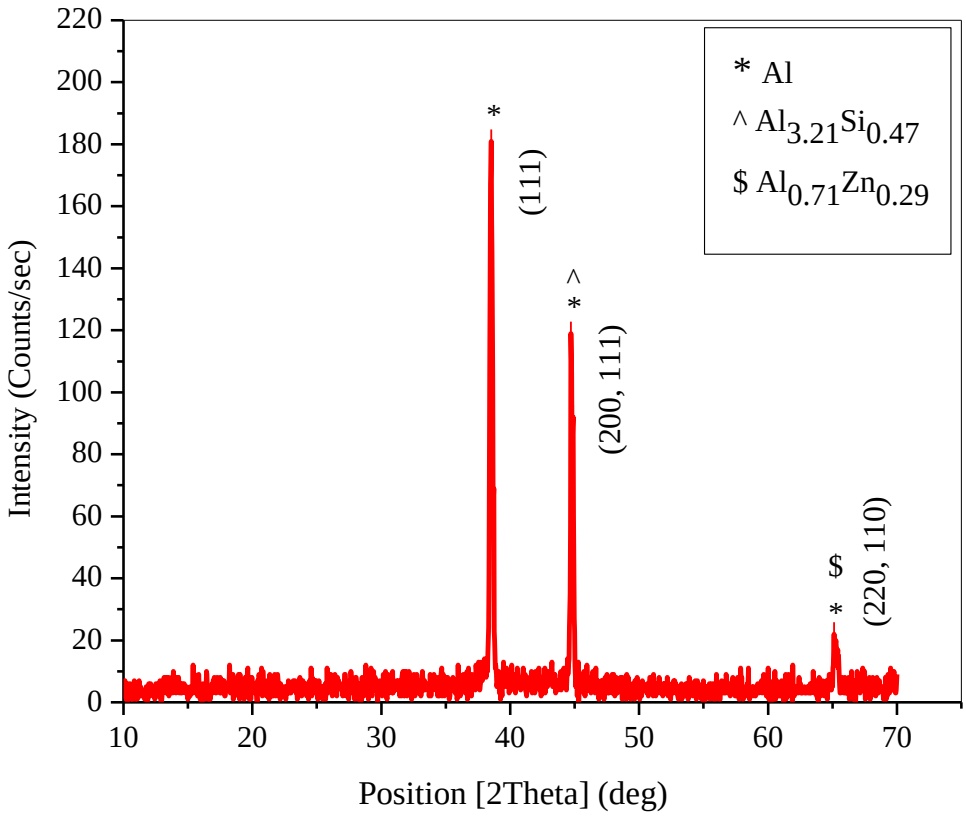

Figure 5.3 XRD plot of the welded sample

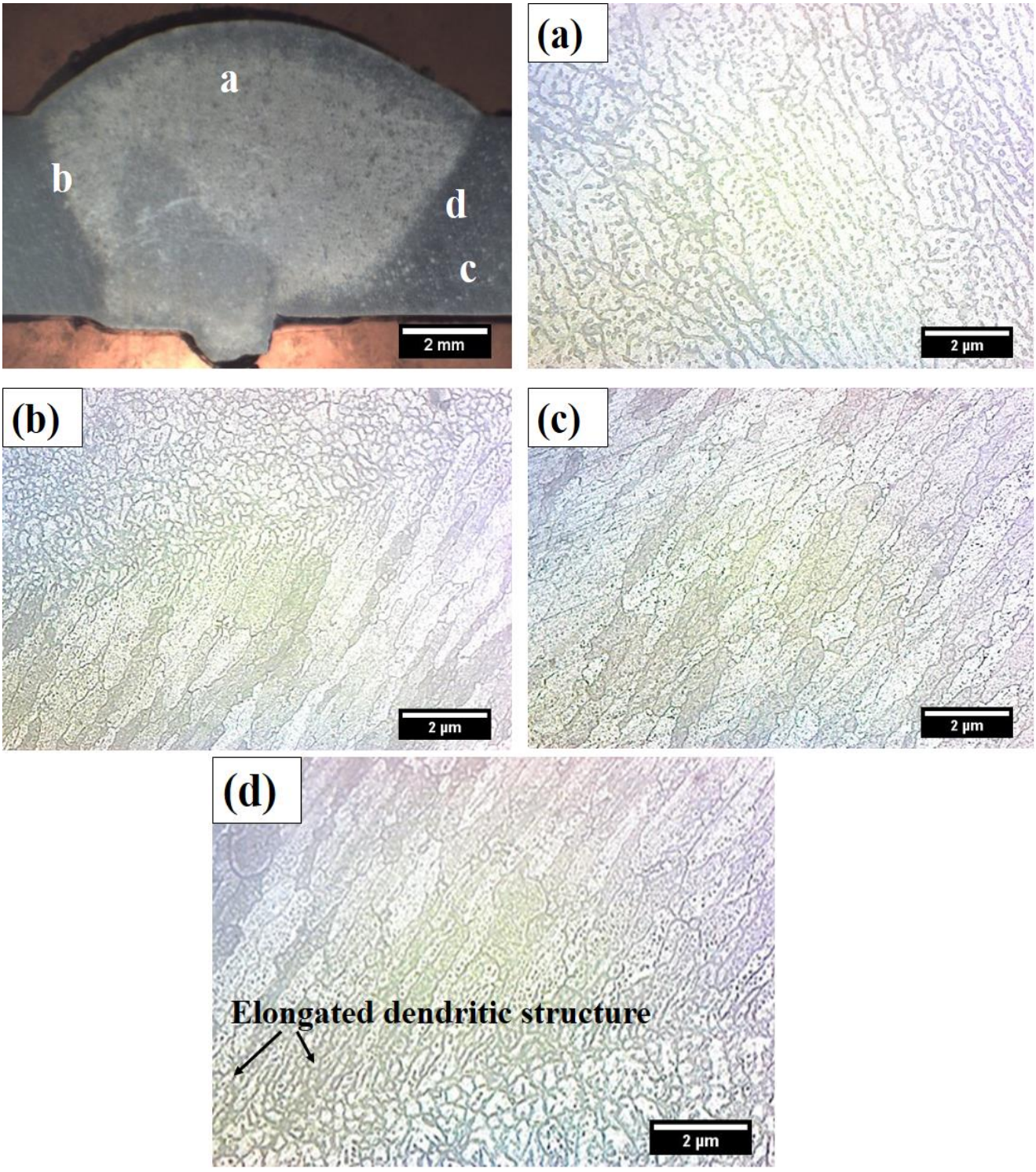

Figure 5.4 Microstructural images of welded sample were taken at various locations: (a) Weld bead, (b) Bead and HAZ interface, (c) Base metal zone, and (d) HAZ

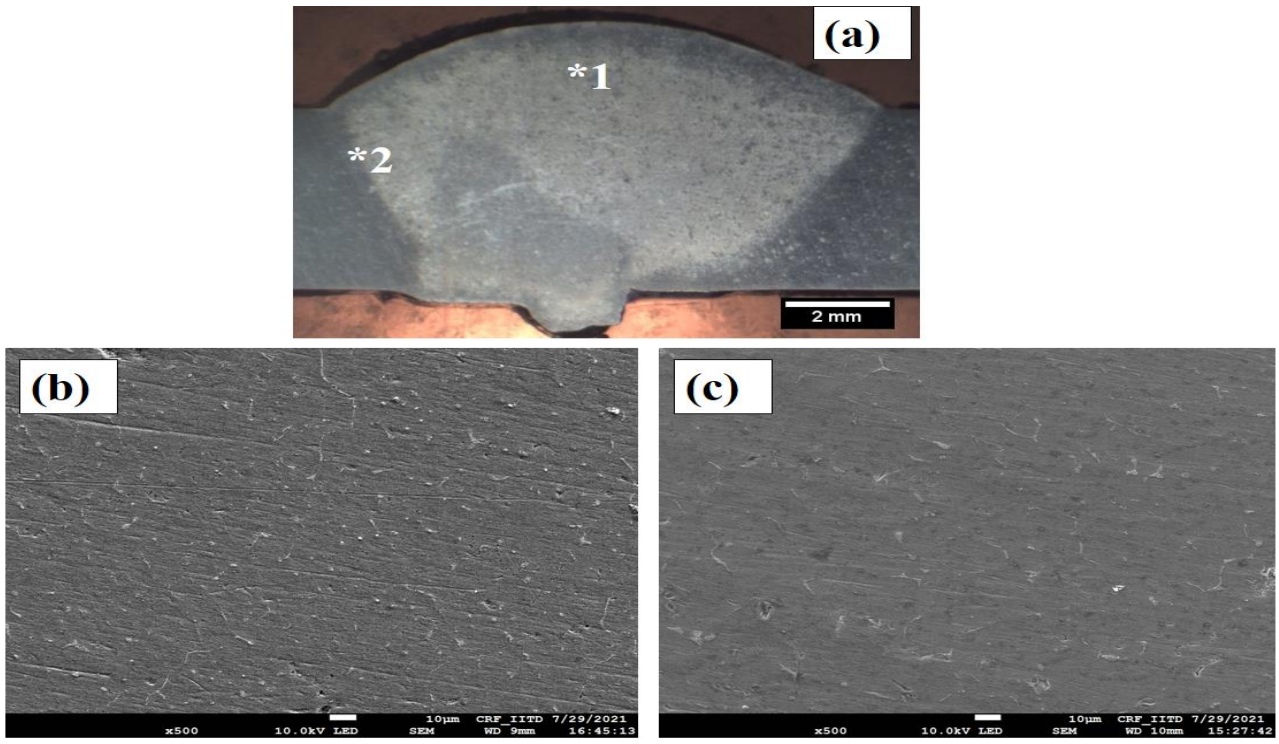

(e)

Element	Wt%	Atomic %
Mg K	0.34	0.39
Al K	94.91	97.54
Ti K	0.05	0.03
Mn K	0.13	0.07
Fe K	0.00	0.00
Ni K	0.00	0.00
Cu L	4.38	1.91
Zn L	0.09	0.04
Zr L	0.10	0.03
Total	100.00	100.00

(g)

Element	Wt%	Atomic %
Mg K	0.15	0.17
Al K	93.17	95.55
Si K	2.45	2.41
Ti K	0.17	0.10
Mn K	0.00	0.00
Fe K	0.15	0.07
Ni K	0.00	0.00
Cu L	3.46	1.51
Zn L	0.39	0.17
Zr L	0.05	0.01
Total	100.00	100.00

Figure 5.5 FESEM images of the weld bead (a) The points denote the location of the images (b) and (c), representing FESEM images of point 1 (weld bead region) and point 2 (HAZ region), respectively. (d) and (e) illustrate the EDX image of point 1 with atomic weights; (f) and (g) illustrate the EDX spectrum image of point 2 with atomic weights

The XRD analysis was employed to identify intermetallic phases within the samples. Since both the parent material and filler material are primarily composed of aluminium and silicon, the predominant peaks in the XRD plots, as depicted in Figure 5.3. The dimensions and morphology of individual weld beads predominantly influence key CMT process parameters [Koli et al., 2021]. Notably, the XRD patterns indicate a minimal presence of intermetallic phases, which is characteristic of the small heat input associated with this welding technique. It displays the presence of solely $Al_{3.21}Si_{0.47}$ and $Al_{10.71}Zn_{0.29}$ binary phases. This limited formation of intermetallic phases is crucial, as an excessive presence of such phases can detrimentally impact mechanical properties, leading to degradation in strength. Therefore, the observed low content of intermetallic phases in the XRD analysis aligns with the expected outcomes of CMT's low heat input characteristics, ensuring favorable mechanical properties in the welded samples. FESEM and EDX images of the weld bead are shown in Figure 5.5. The FESEM image unveils a finely dispersed precipitate within the weld bead zone. The confirmation of silicon and zinc elements in the weld bead zone is evidenced by the EDX plot, indicating a transformation influenced by the composition of the filler metal.

5.4 TENSILE PROPERTIES

In accordance with ASTM E8M standards, tensile test specimens were made from the welded plates. Figure 5.6 illustrates the tensile test specimens both before and after testing, while Figure 9 presents the corresponding stress versus strain graph. As shown in Table 5.2, the welded joint achieved its maximum tensile strength in sample 8, measuring 298 MPa, which represents 97.39% of the strength of the parent 2099-T86 metal. This sample also exhibited a percentage elongation of 17.9%. Notably, sample 8 demonstrated the highest tensile strength across all

tested samples, achieved with a heat input of 363.6 J/mm. In contrast, sample 3 recorded the lowest tensile strength at 200 MPa, along with the least elongation at 5.31%. The process parameters for sample 8 were 180 A current, 8 m/s welding speed, and 4 mm CTWD, while for sample 3, the process parameters taken were 150 A, 10 m/s, and 8 mm CTWD. Appropriate heat input during CMT welding helps to maintain maximum tensile strength and ductility. The heat input during CMT welding results in higher weld joint efficiency. The heat input mainly depends upon the range of process parameters during welding. Heat input and welding speed have an inverse connection; increasing welding speed causes heat input to decrease, while decreasing welding speed causes heat input to increase. The occurrence of bigger-size brittle intermetallic compounds in the fusion zone results in lower tensile strength, as observed in XRD and EDX plots of welded joint beads. The fracture morphology of the tensile sample was detected by FESEM observation at different magnifications and is shown in Figure 5.8.

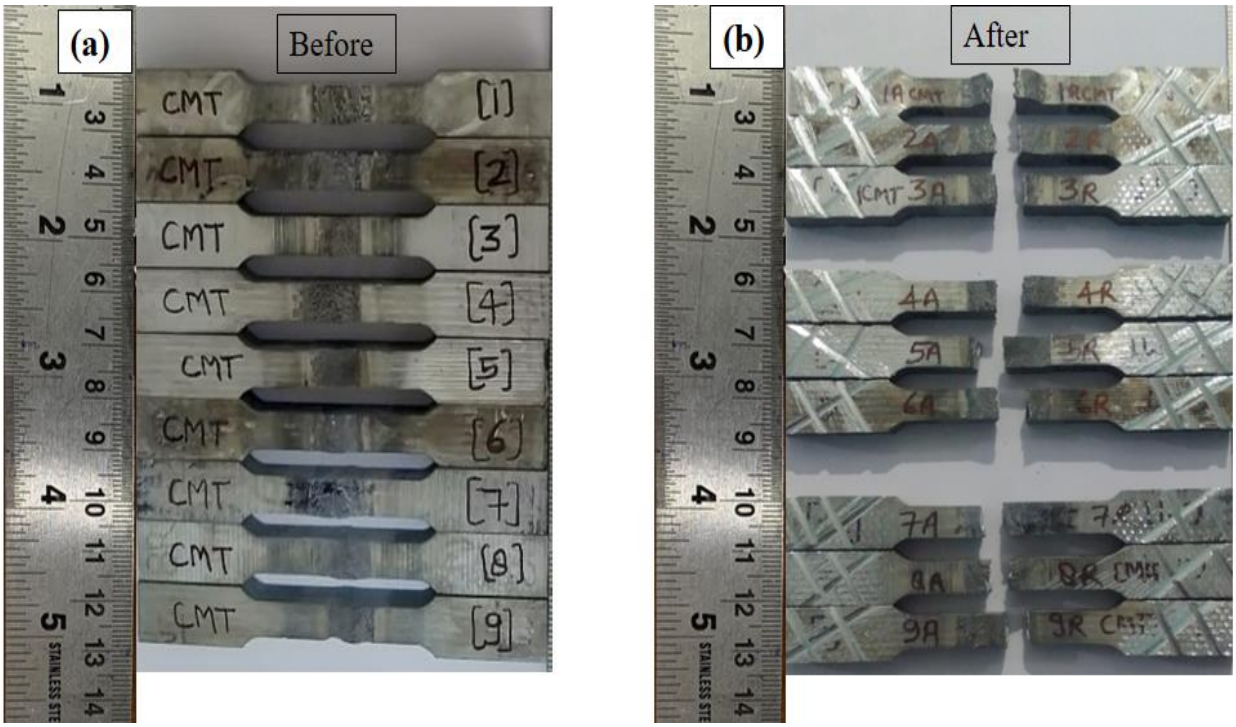

Figure 5.6 Tensile specimens (a) before and (b) after tensile testing

In the image, the dimpled morphology was without cracks, and the least precipitation was observed. Micropits of different sizes available in the fractography samples indicate very fine dimples. Figure 5.8(a), (b), and (c) reveal the presence of deep dimples, which result in the ductile mode of metal failure. A comparable finding was reported by Nagasai et al. (2023). The ductile material failure mode results in a higher percentage of elongation and weld efficiency [Roy et al., 2021]. Upon further examination of the micro pits, EDX analysis was conducted on the sample, specifically at spectrum points 3, 4, and 5, located on the tensile broken surfaces shown in Figure 5.8 (e) to (g). The results of this analysis reveal the presence of Al, Si, Cu, and Zn as the primary elements, along with a small quantity of precipitation in the secondary phase. The high amount of precipitation leads to the degradation of joint strength.

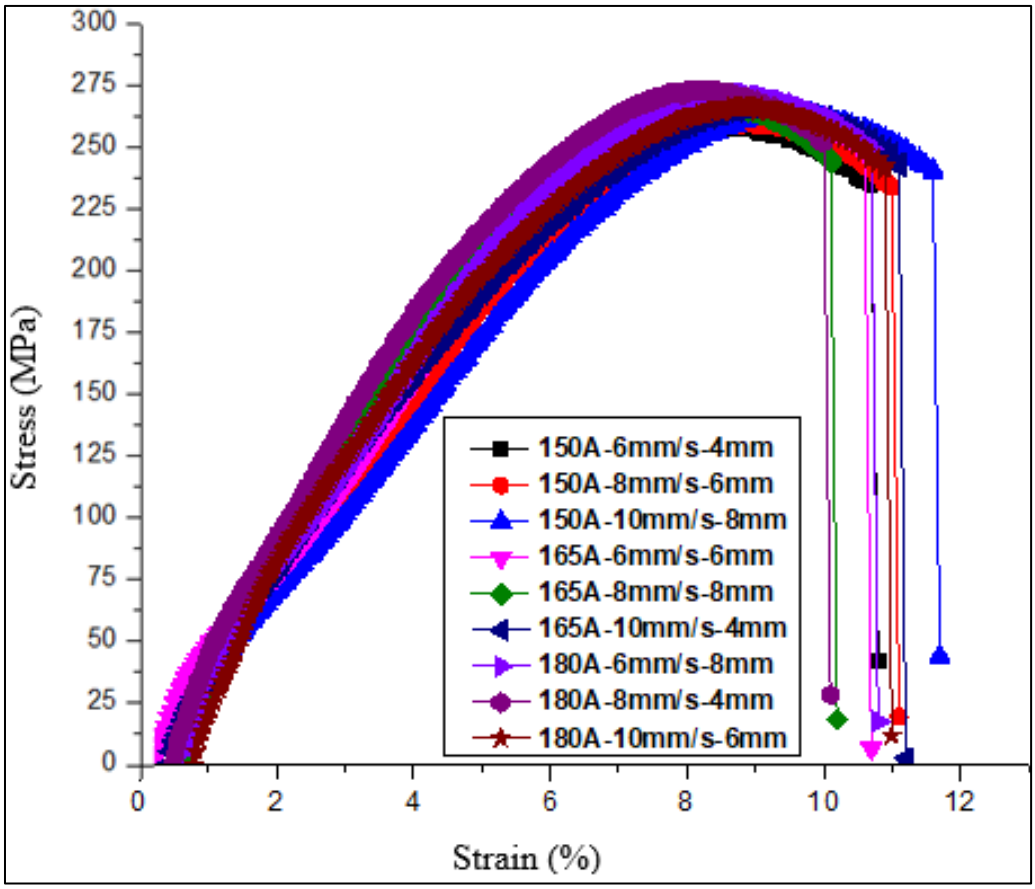

Figure 5.7 Stress vs. strain curve of welded samples

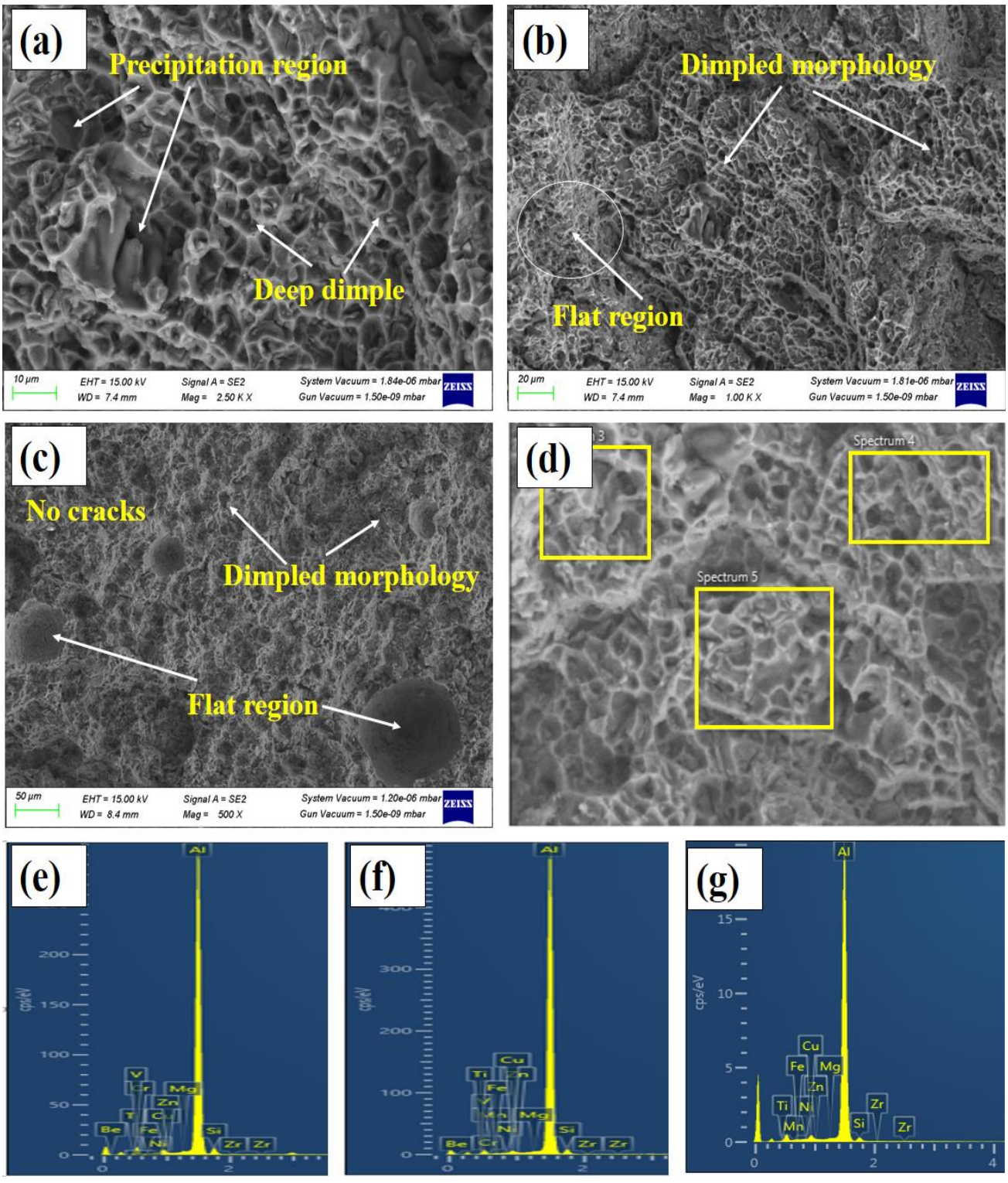

Figure 5.8 FESEM images taken at different magnifications of tensile fractography sample and EDX analysis conducted at points 3, 4, and 5 on the spectrum

5.5 MICRO-HARDNESS EVALUATION

Figures 5.9(a) and (b) depict the distribution of micro-hardness measurements taken along parallel (X_1X_2) and perpendicular (Y_1Y_2) directions, respectively. To illustrate the changes in micro-hardness along the Y_1Y_2 direction of the weld bead, a gap of 0.5 mm was provided for the initial measurement, while subsequent measurements were spaced 1 mm apart from the top of the bead (Y_1). Similarly, to demonstrate micro-hardness variations along the X_1X_2 direction of the weld bead, a 1 mm gap was left for both the initial and subsequent measurements. The micro-hardness values found in the HAZ and weld bead region are lower than the base metal. Compared to the base metal, the micro-hardness values in the HAZ and weld bead regions are lower. The micro-hardness values in the weld bead and HAZ zones exhibit reductions of nearly 8.35% and 1.22%, respectively, when compared to the base metal. This decrement in micro-hardness value in both the microstructural zones is owing to the creation of elongated dendrites, as seen in Figure 5.4(d). Figure 5.4(b) illustrates how the softening effect of the increasing heat input causes grain coarsening at the weld contact. The micro-hardness measurements at the top of the CMT-welded specimen range from 103.44 to 117.21 HV0.3. At the center zone of the CMT-welded samples, a small reduction in microhardness was seen as the samples moved from Y_1 to Y_2. The weld beads of aluminum alloys often undergo significant softening as they solidify in the molten pool, resulting in the weld zone exhibiting the lowest microhardness. During butt welding, the rapid solidification of the lower and upper surfaces of the weld occurs due to their exposure to atmospheric air.

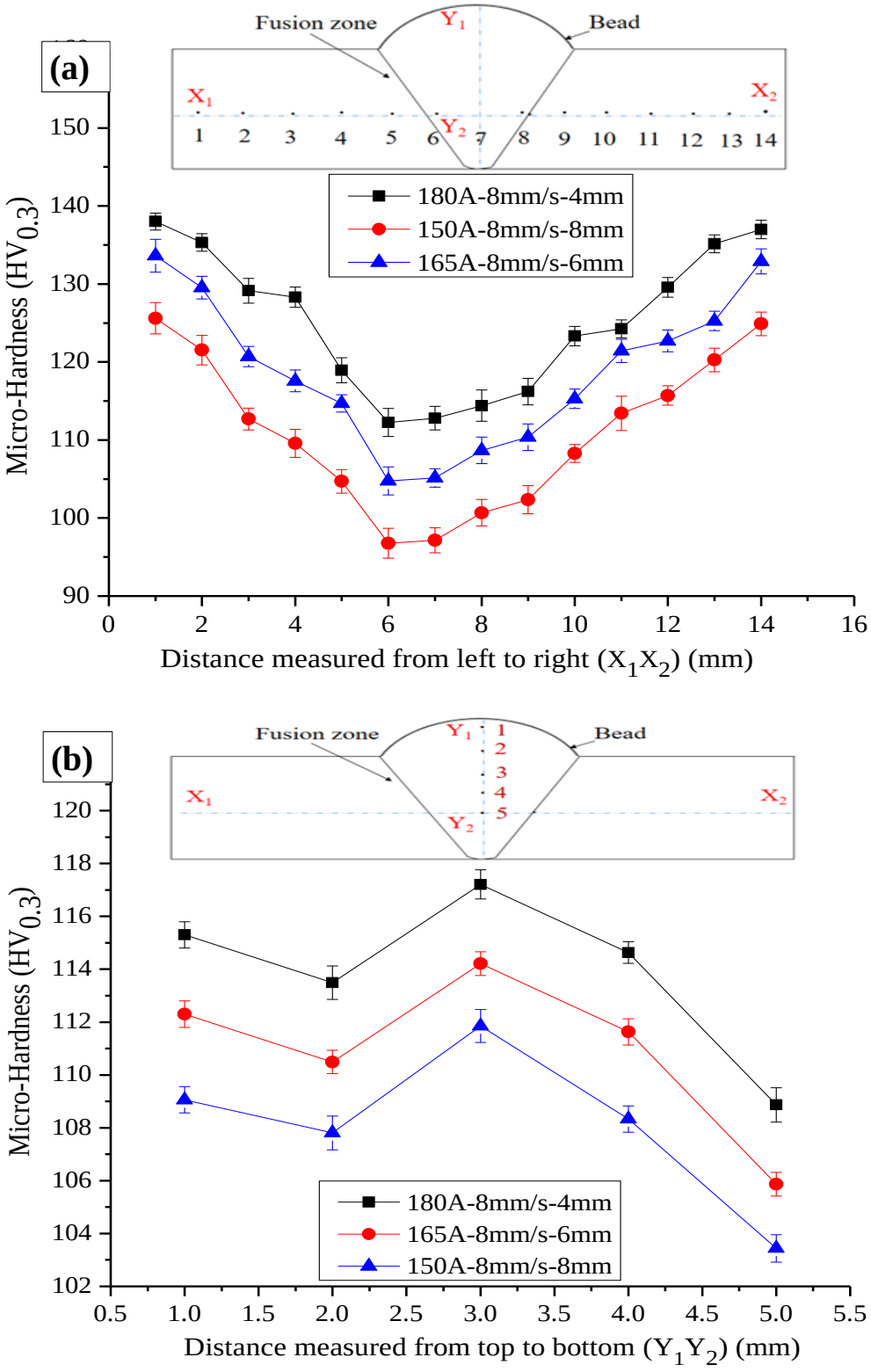

Figure 5.9 Microhardness variation across the welded joints: (a) Parallel (X_1X_2) and (b) Perpendicular (Y_1Y_2)

5.6 FABRICATION OF CMT WELDED JOINT UNDER DIFFERENT ENVIRONMENT CONDITIONS

5.6.1 Introduction

Environmental factors significantly influence the mechanical properties of welded joints during CMT welding. However, research on CMT welding of Al-Li alloys under different environmental conditions is limited. This study investigates the effects of cooling with liquid nitrogen and the use of ultrasonic vibrations on the mechanical properties of CMT-welded aluminium-lithium alloys. To evaluate performance, butt joints of the AA2099-T86 alloy were fabricated using the CMT process in three different environments, i.e., conventional (C-CMT), liquid nitrogen (LN-CMT), and ultrasonic vibration welding (U-CMT). Following multiple trial experiments, optimal welding parameters were determined, set at a current of 165 A, a speed of 8 mm/sec, and a CTWD of 8 mm for all conditions.

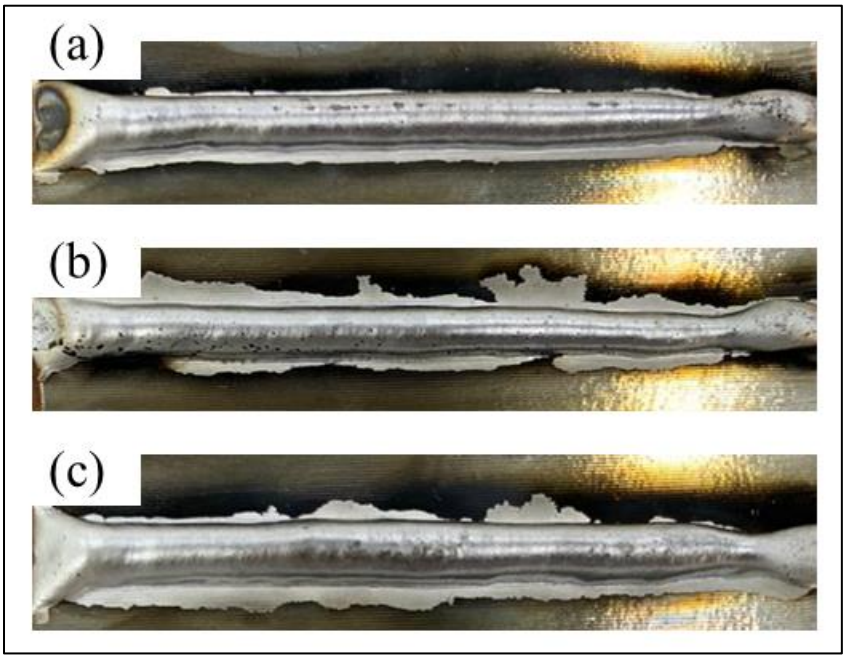

Figure 5.10 Weld bead images of (a) C-CMT, (b) LN-CMT, and (c) U-CMT welding

5.6.2 Microstructure evaluation

The weld bead images formed by C-CMT, LN-CMT, and U-CMT are shown in Figure 5.10. The base metal grain size is found to be 67 µm. The microstructure images of welded samples fabricated at different environmental conditions are shown in Figure 5.11. Table 5.6 reveals that the U-CMT joint exhibits the smallest grains, whereas the C-CMT joint displays the largest ones. The size of recrystallized grains is intricately linked to factors such as heat input, strain rate, and cooling rate. The temperature evolution during CMT welding also affects the microstructure characterization of the welded joints.

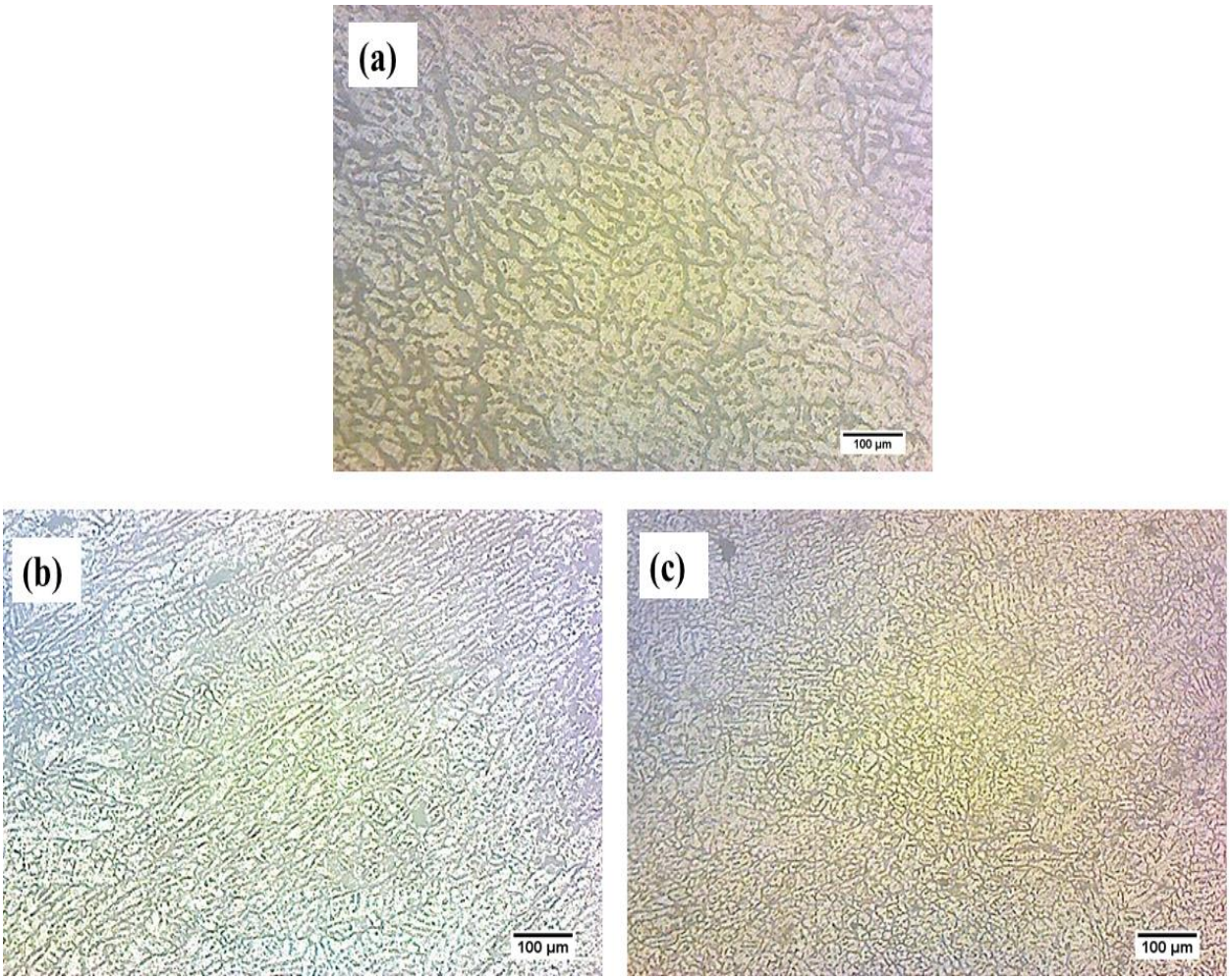

Figure 5.11 The microstructure images of welded samples fabricated at different environmental conditions (a) C-CMT, (b) LN-CMT, and (c) U-CMT welding

The grain size of the weld region is depicted with the help of ImageJ software and found to be 53.48 µm (Figure 5.13(a)), 47.71 µm (Figure 5.13(b)), and 42.88 µm (Figure 5.13(c)), respectively, for C-CMT, LN-CMT, and U-CMT welded joints. Using liquid nitrogen during the CMT process results in a reduction of the weldment's grain size to 47.71 µm. This decrease in grain size may be due to the effective cooling of liquid nitrogen, which restricted the grains to the finer grains [Ji et al. (2020), Sastry et al. (2019), and Reza et al. (2021)]. With the application of ultrasonic vibration during CMT, the grain size of the weldment is reduced to 42.88 µm due to the growth of columnar grains.

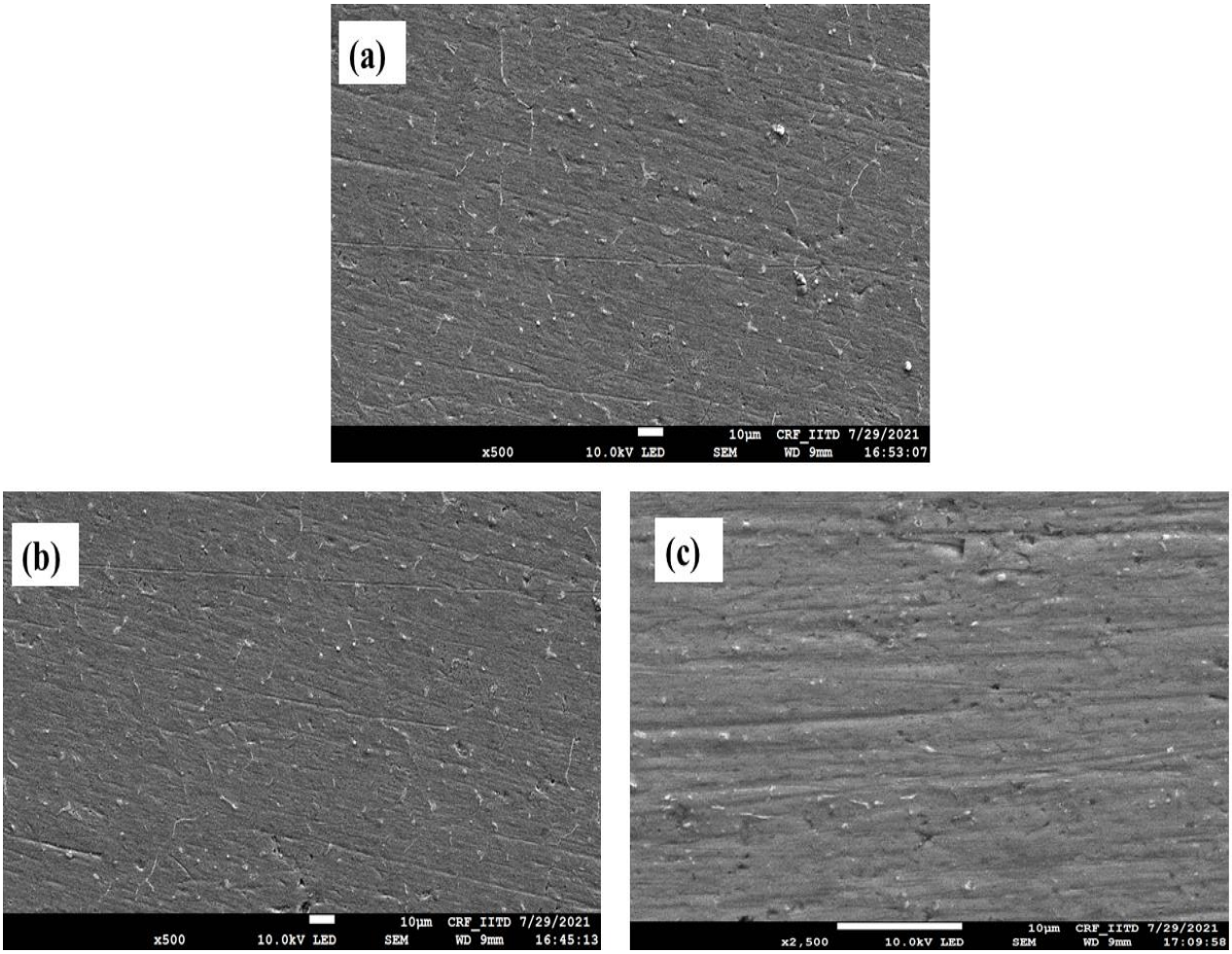

Figure 5.12 FESEM images of welded samples fabricated at different environmental conditions (a) C-CMT, (b) LN-CMT, and (c) U-CMT welding

Similar results were obtained by Zhao et al. (2020), who showed that ultrasonic vibration-welded joints had a significant improvement in grain refinement when compared to non-vibration-welded joints. As ultrasonic vibrations are present during CMT welding, the weld's grain size is reduced, which increases joint strength as compared to other welded joints. FESEM images of welded samples produced at different environmental conditions show the presence of precipitates in the weld region, as seen in Figure 5.12.

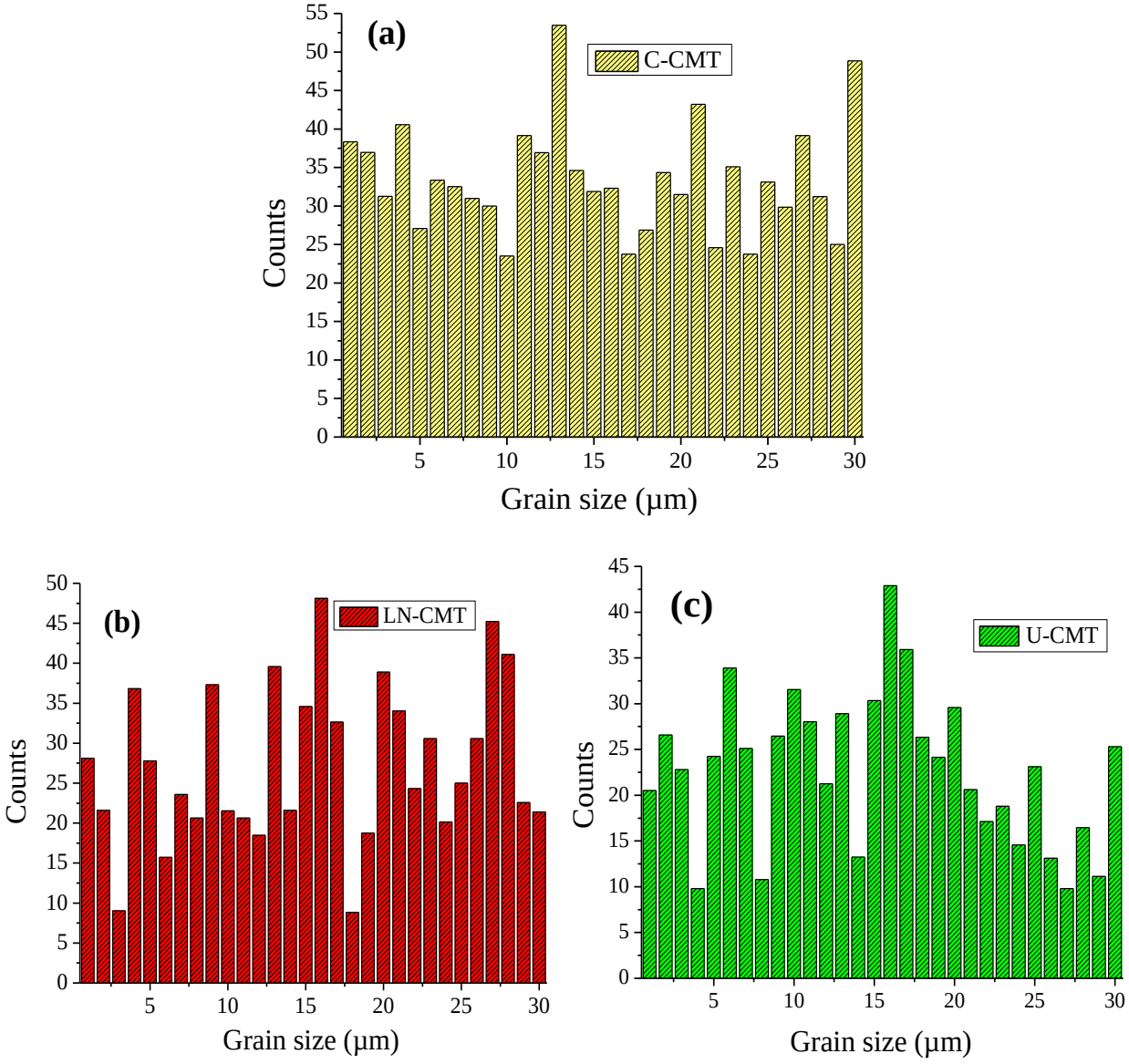

Figure 5.13 Grain size of (a) C-CMT, (b) LN-CMT, and (c) U-CMT welding

Similar results were reported by Urminsky et al. (2019) during the joining of AA2099 plates. Microstructural images of the U-CMT sample were taken at various locations: (a) weld bead, (b) at the interface, and (c) HAZ, as revealed in Figure 5.14. In the U-CMT welded sample, finer precipitates are formed as compared to other samples, decreasing grain size. Grain structure in the U-CMT welded joint is notably columnar, whereas the C-CMT welded joint has elongated strip-like grains.

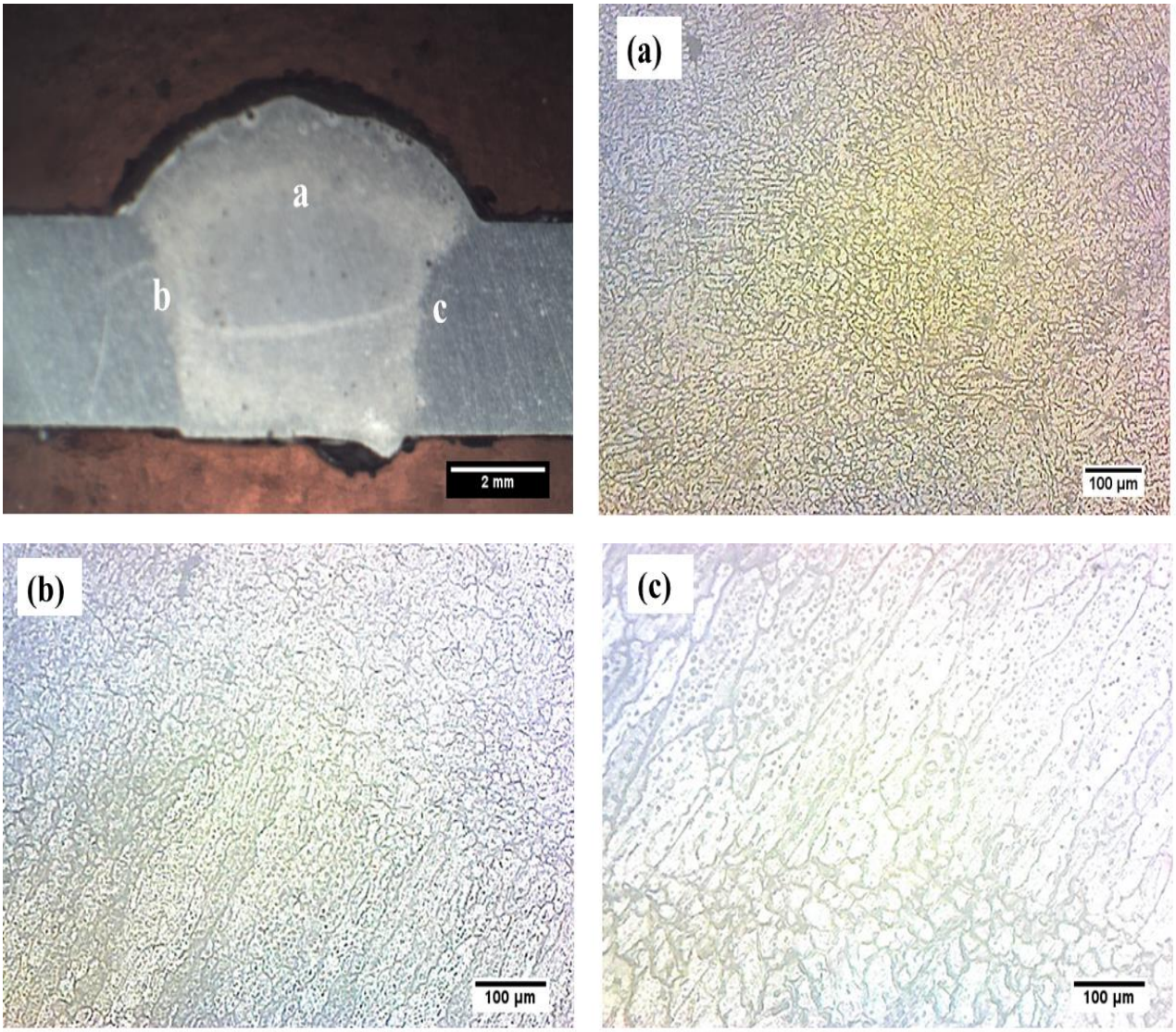

Figure 5.14 Microstructural images of U-CMT sample were taken at various locations: (a) weld bead, (b) at the interface, and (c) HAZ

5.6.3 Tensile properties

Figure 5.15 illustrates the samples of C-CMT, LN-CMT, and U-CMT welded joints both before and after tensile testing. Notably, the U-CMT tensile specimen (S1) exhibits fracture at the heat-affected zone, whereas the C-CMT (S2) and LN-CMT (S3) tensile specimens fracture at the weld zone. The tensile test results of fabricated welded samples under different environmental conditions are exhibited in Table 5.6. The application of ultrasonic vibration during welding significantly enhances the UTS, reaching a peak value of 252 MPa, marking a 10.52% increase compared to C-CMT and a 2.02% increase in the LN-CMT welded joint devoid of ultrasonic vibration. This enhancement is attributed to the finer grain size of 42.88 μm, as depicted in Figure 5.13(c).

Table 5.6 Tensile test results of welded joints

Weld Sample	Welding Process	Welding current (Ampere)	Welding speed (mm/s)	CTWD (mm)	Ultimate tensile strength (MPa)	Micro-hardness (HV)	Grain size (μm)	Weld joint strength (%)
S1	U-CMT	165	8	8	252	115.96	42.88	79.54
S2	C-CMT	165	8	8	228	106.14	53.48	71.96
S3	LN-CMT	165	8	8	247	110.91	47.71	77.96

Ultrasonic frequency = 20 kHz

Amplitude of ultrasonic vibration = 60 μm

Flow rate of shielding gas = 16 Litres/min

Current = Direct current reverse polarity (DCRP)

The grain sizes obtained in the C-CMT-welded sample (S2) and LN-CMT-welded sample (S3) are 53.48 µm and 47.71 µm, respectively, as shown in Figures 5.13(a) and 5.13(b). This refining of grain size is due to the Hall-Petch relationship [Du et al., 2019].

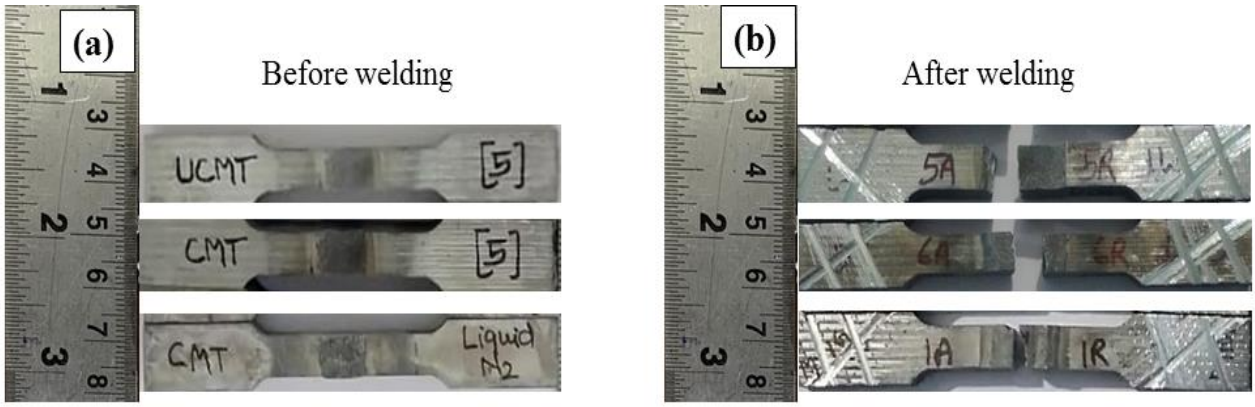

Figure 5.15 Tensile test samples (a) Before and (b) After tensile testing

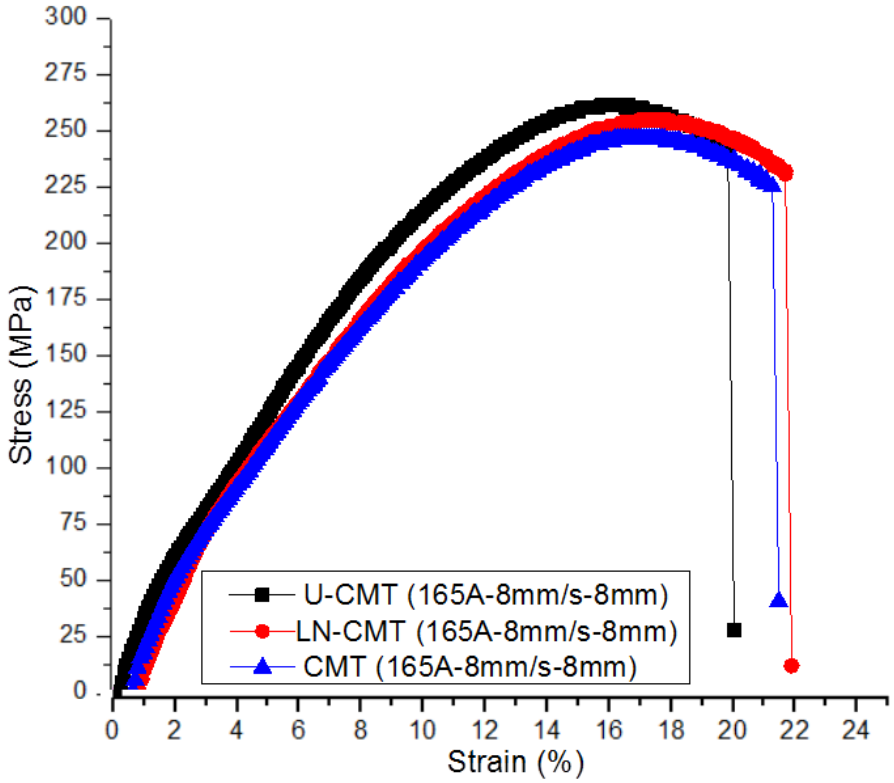

Figure 5.16 Stress-strain curve for C-CMT, LN-CMT and U-CMT welded joints

The stress-strain plot is shown in Figure 5.16. The percentage elongation of the U-CMT sample, the C-CMT sample, and the LN-CMT sample were found to be 23.55%, 20.6%, and 17.4%, respectively. The base metal elongation is 14.9%, which is 14.32% higher than the C-CMT sample and 35.34% higher than the LN-CMT sample, respectively. Liu et al. (2023) utilized liquid CO2 in the friction stir welding (FSW) of AA1050-H24 alloy. They noted that although the cooling effect increased the tensile strength of the welded joint, it also resulted in reduced elongation due to contraction in the weld area. The welding joint strengths of the U-CMT, C-CMT, and LN-CMT samples were found to be 79.54%, 71.96%, and 77.96%, respectively.

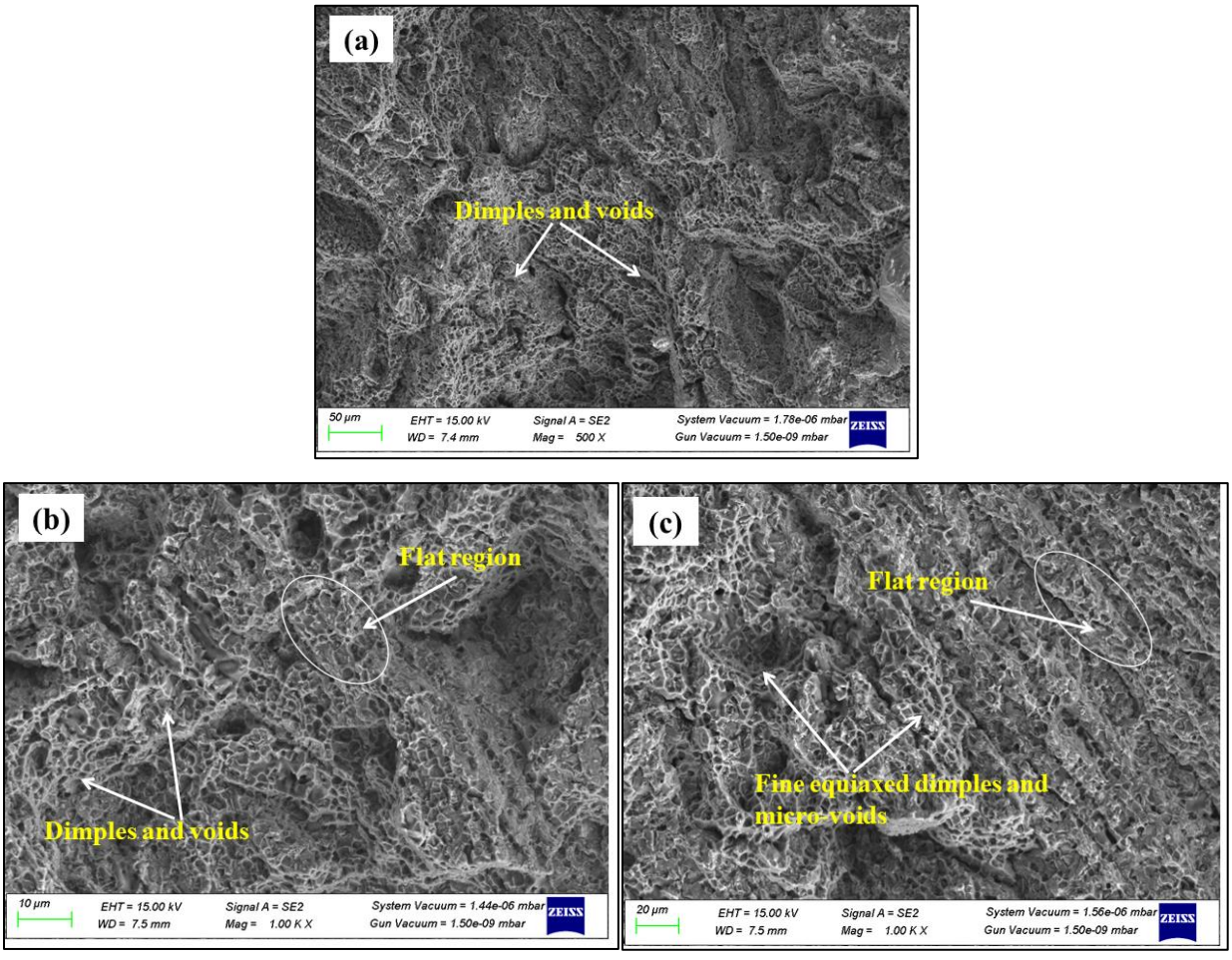

Figure 5.17 FESEM images of the tensile fracture surface of (a) C-CMT, (b) LN-CMT, and (c) U-CMT-welded joints

It was revealed that the weld joint strength of the U-CMT sample is 10.53% higher than C-CMT and 2.02% higher than the LN-CMT welded joint. Figure 5.17 presents FESEM images of the tensile fracture surfaces of welded joints. Dimples and voids are seen in the tensile fracture surface of the C-CMT sample as per Figure 5.17(a). Some flat regions are observed in the LN-CMT sample along with dimples and voids, as per Figure 5.17(b). Figure 5.17(c) shows the tensile fracture surface of the U-CMT sample, where micro-voids and finely equiaxed dimples result from grain refinement. A similar type of observation was confirmed by Koli et al., (2021). The ductile mode of failure results in a higher percentage of elongation and weld joint efficiency [Roy et al. 2021].

5.6.4 Micro-hardness study

The micro-hardness measurements of welded samples were taken along the crosssection of weld bead depicted in Figure 5.18. The average microhardness values for the U-CMT, C-CMT, and LN-CMT samples were around 115.96 HV, 106.14 HV, and 110.91 HV, respectively, whereas the base metal microhardness was 106 HV. The variations in microhardness are attributed to factors like precipitate formation, softening of the HAZ, coarse grain structure, and brittle intermetallic compounds. It was found that the U-CMT welded sample had higher microhardness than the C-CMT and LN-CMT samples, due to its smaller grain size. This finding is consistent with Singh et al. (2016), who reported that ultrasonic vibrations during CMT welding significantly increase microhardness. Specifically, the U-CMT sample showed an average increase in microhardness of 9.25% and 4.55% compared to the CMT and LN-CMT samples, respectively. Similarly, Koli et al. (2021) observed an 18.5% higher average microhardness in ultrasonic assisted joints in comparison with conventional CMT weld joints.

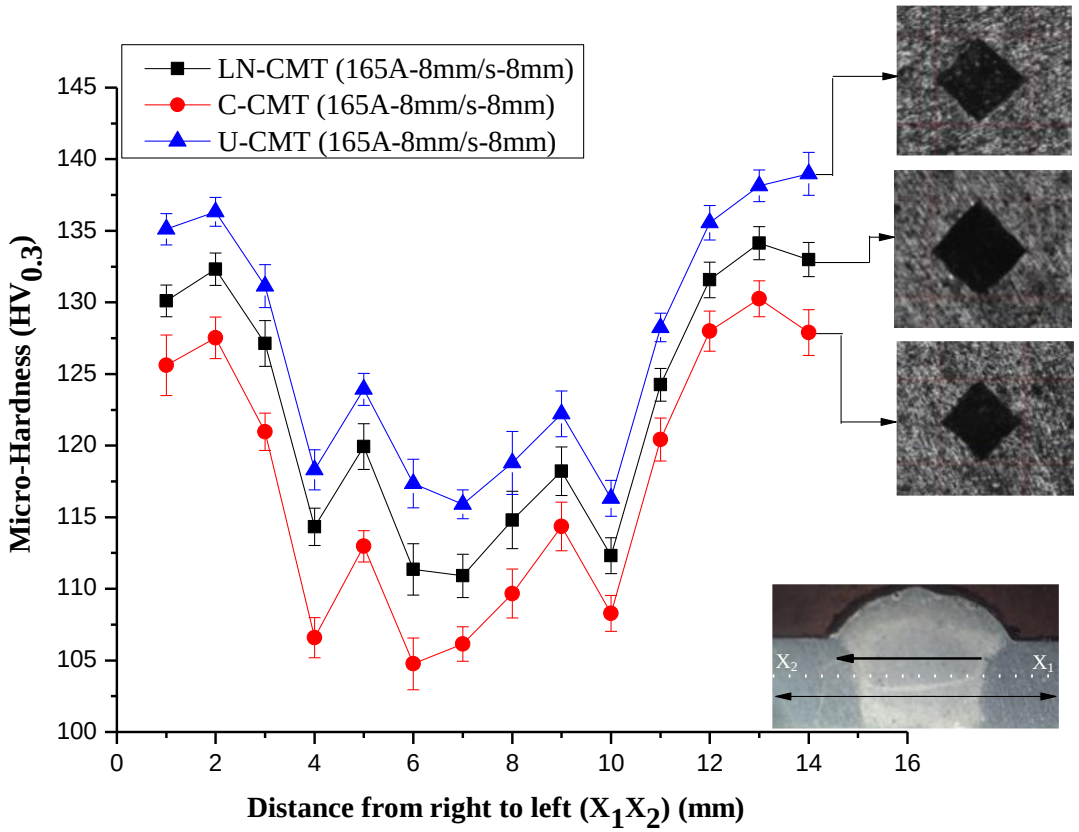

Figure 5.18 Micro-hardness profile of C-CMT, LN-CMT, and U-CMT samples w.r.t. weld positions

Various researchers have reported that the finer grain size of the weld region has enhanced micro-hardness. Masumura et al. (1998) noted that finer grain sizes generally lead to increased hardness in welded materials. Cui et al. (2024) suggested that grain refinement in the weld microstructure results in increased microhardness. According to Xiang et al. (2024), ultrasonic vibrations can enhance the recrystallization process during welding. Yang et al. (2024) investigated the effects of ultrasonic vibration and deep cryogenic treatment on the residual stress, mechanical properties, and microstructures of HR-2 austenitic stainless steel, finding that these treatments led to the highest hardness values due to grain size reduction and the strengthening effect of precipitates.

5.7 SUMMARY

This chapter focuses on the CMT butt joining of AA2099-T86 alloy with uniform thickness across a range of welding input parameters outlined in the design matrix. It briefly discusses the dimensions of the weld bead, including weld reinforcement, weld width, and weld penetration. To evaluate the mechanical properties of the CMT welded joints, welding current, speed, and contact tip-to-work distance were selected as input parameters. The optimization of these welding parameters for the processed joints was performed using the Taguchi L9 method, with tensile strength and micro-hardness as the key responses. The chapter also includes microstructural analysis of the CMT butt welds at various locations and discusses the fabrication of CMT welded joints under different environmental conditions. To compare performance, butt joints of the AA2099-T86 alloy were created using the CMT process in three environments: conventional (C-CMT), liquid nitrogen (LN-CMT), and ultrasonic vibration welding (U-CMT). The comparison was based on microstructural evaluations, micro-hardness measurements, and ultimate tensile strength, including fractography. Results indicated that CMT-welded joints produced in the ultrasonic vibration environment exhibited improved mechanical properties compared to the other conditions studied, with notable grain refinement observed in U-CMT-welded joints.

CHAPTER 6: CONCLUSIONS AND SCOPE FOR FUTURE WORK

6.1 CONCLUSIONS

This chapter summarizes the main conclusions derived from the findings and discussions presented in the previous chapters.

AA2099-T86 alloy with 5 mm thickness base material and 1.2 mm diameter ER4047 filler wire were chosen in the present research. CMT and pulse MIG welding processes are used for the study of weld on bead geometry. The optimization of weld-bead experiments employs a multicriteria decision-making approach using CRITIC and ROV-based Taguchi methods. To compare the mechanical and microstructural properties, butt joints of the AA2099-T86 alloy were fabricated using the CMT welding in three environments: conventional (C-CMT), liquid nitrogen (LN-CMT), and ultrasonic vibration welding (U-CMT).

6.1.1 Optimization of weld-bead

- The shape of the weld bead is significantly affected by various process parameters such as welding current, welding speed, and CTWD.
- CMT heat input was 10% smaller, the weld penetration was 14% smaller, and the dilution was 6.44% lower than the pulse MIG welding by increasing the value of CTWD from 6 to 8 mm. This is due to the fact that any increase in the value of CTWD can lower the amperage and result in poor penetration.
- The weld bead is closely linked to heat input and dilution, with higher heat input leading to increased dilution from melting more substrate metal. The CMT process results in approximately 4.47% less dilution compared to pulse MIG, attributed to the oscillating action of the wire, which maintains a consistent arc length and enhances dilution control.

- In the CMT process, welding speed is the most influential input parameter, with CTWD and current being secondary factors. In contrast, for the pulse MIG process, welding speed is also the key parameter, but it is followed in importance by welding current and CTWD.
- The ideal configuration of input parameters for achieving optimal multi-responses in CMT welding is $I_3S_3D_2$, which corresponds to a current of 180 A, a welding speed of 10 mm/sec, and a CTWD of 6 mm. For pulse MIG welding, the optimal settings are $I_1S_3D_2$, which equate to a current of 150 A, a welding speed of 10 mm/sec, and a CTWD of 6 mm.
- With the optimal set of input parameters, the optimal welding penetrations are 5.8 mm for CMT and 6.4 mm for pulse MIG, respectively. Dilutions are 78.12% for CMT and 78.21% for pulse MIG, respectively. Heat inputs are 252.72 J/mm for CMT and 241.2 J/mm for pulse MIG, respectively.
- Optimization results are validated as the experimental and predicted values of the S/N ratio at the optimum combination are in close agreement, i.e., percentage error = 2.65% and 3.2% for CMT and pulse MIG, respectively.

6.1.2 CMT Butt-weld joint

- The optimal welding conditions of 180 A of current, 8 mm/s of welding speed, and 4 mm CTWD resulted in a maximum tensile strength of 298 MPa for CMT-welded 2099-T86 alloy joints. The primary reasons for this exceptional strength are the controlled heat input during the welding process and the minimal intermetallic phase formation.

- The tensile fracture surface has deep dimples, indicating that the ductile failure mode occurs in the welded joint. The ductile mode of material failure results in a higher percentage of elongation and weld joint efficiency.
- Weld bead zone and heat-affected zone (HAZ) microhardness values dropped by around 8.35% and 1.22%, respectively, mostly as a result of elongated dendrite development and the resulting material softening impact.
- The Taguchi methodology was utilized to identify the optimal welding parameters, resulting in the settings of WC3-WS1-CTWD1. The optimal responses achieved were a tensile strength of 302 MPa and a microhardness of 118 HV. The results of the ANOVA analysis showed that the welding current of 180 A, the welding speed of 6 mm/s, and the CTWD of 4 mm were the most significant parameters. Their p-values were all less than 0.05.

6.1.3 Fabrication of CMT welded joint under different environment conditions

- Comparative analysis of joint efficiencies showed that the U-CMT-welded sample achieved a notable efficiency of approximately 79.54%, whereas C-CMT and LN-CMT exhibited efficiencies of about 71.96% and 77.96%, respectively.
- The FESEM images of the tensile fracture surfaces of LN-CMT, C-CMT, and U-CMT welded joints revealed distinct features. The C-CMT-welded joint showed dimples and voids, while the LN-CMT-welded sample exhibited both flat areas and dimples alongside voids. On the fracture surface of the U-CMT-welded joint, micro-voids and finely equiaxed dimples were observed, attributed to grain refinement.

- The welded joint fabricated without ultrasonic vibration manifests a relatively lower ultimate tensile strength (UTS), typically at 228 MPa and 247 MPa, respectively. Conversely, the application of ultrasonic vibration during welding significantly enhances the UTS, reaching a peak value of 252 MPa, marking a 10.52% increase compared to C-CMT and a 2.02% increase in the LN-CMT welded joint devoid of ultrasonic vibration. This enhancement is attributed to the finer grain size of the U-CMT-welded sample (42.88 μm). The grain sizes obtained in the C-CMT-welded sample and LN-CMT-welded sample are 53.48 μm and 47.71 μm, respectively.
- The U-CMT welded sample had higher microhardness than the C-CMT and LN-CMT samples, likely due to its smaller grain size. Specifically, the U-CMT sample showed an average increase in microhardness of 9.25% and 4.55% compared to the CMT and LN-CMT samples, respectively. The average grain sizes for the C-CMT and LN-CMT samples were 53.48μm and 47.71μm, respectively, while the U-CMT sample had a finer grain size of approximately 42.88μm.

6.2 SCOPE FOR FUTURE WORK

- The setup can be further optimized by adjusting various other process parameters, including gas flow rate, wire size, type of filler wire, wire feed rate, and arc correction factor, to enhance the mechanical properties of the welded joints.
- A robotic CMT setup can be used for the fabrication of different geometry-shaped joints of AA2099-T86 alloy-welded joints with high precision and accuracy.
- Spin arc welding can be used for joining thicker materials with deeper weld penetration.

- Artificial neural networks (ANN) can be used for the optimization of welding parameters and get more precise results.
- AI and ML techniques can be used for the precise prediction of the output response of a CMT welded joint.
- Industrial welding applications can easily be scaled up using the easy and highly effective ultrasonic assisted CMT and ultrasonic assisted CMT with liquid nitrogen.

REFERENCES

1) Satyanarayana, V. V., Reddy, G. M., & Mohandas, T. (2005). Dissimilar metal friction welding of austenitic–ferritic stainless steels. Journal of Materials Processing Technology, 160(2), 128-137.
2) Ibrahim, I. A., Mohamat, S. A., Amir, A., & Ghalib, A. (2012). The Effect of Gas Metal Arc Welding (GMAW) processes on different welding parameters. Procedia Engineering, 41, 1502-1506.
3) Chacon-Fernandez, S., Garcia, A. P., & Labanda, G. R. (2022). Influence of parameters on the microstructure of a duplex stainless steel joint welded by a GMAW welding process. Progress in Natural Science: Materials International, 32(4), 415-423.
4) Kumar, N. P., Vendan, S. A., & Shanmugam, N. S. (2016). Investigations on the parametric effects of cold metal transfer process on the microstructural aspects in AA6061. Journal of Alloys and Compounds, 658, 255-264.
5) Evangeline, A., & Sathiya, P. (2019). Cold metal arc transfer (CMT) metal deposition of Inconel 625 superalloy on 316L austenitic stainless steel: microstructural evaluation, corrosion and wear resistance properties. Materials Research Express, 6(6), 066516.
6) Pickin, C. G., Williams, S. W., & Lunt, M. (2011). Characterisation of the cold metal transfer (CMT) process and its application for low dilution cladding. Journal of Materials Processing Technology, 211(3), 496-502.
7) Irizalp, A. O., Durmus, H., Yuksel, N., & Turkmen, I. (2016). Cold metal transfer welding of AA1050 aluminum thin sheets. Materia (Rio de Janeiro), 21, 615-622.

8) Kumar, N. P., Chinnadurai, T., Vendan, S. A., & Sivashanmugam, N. (2018). Techno economical evaluation for energy analysis in AA6061 during cold metal transfer welding. Materials Today: Proceedings, 5(11), 23375-23383.

9) Meena, R. P., Yuvaraj, N., & Vipin. (2024). Optimization of process parameters of cold metal transfer welding-based wire arc additive manufacturing of super Duplex stainless steel using response surface methodology. Proceedings of the Institution of Mechanical Engineers, Part E: Journal of Process Mechanical Engineering, 09544089241230878.

10) Feng, J., Zhang, H., & He, P. (2009). The CMT short-circuiting metal transfer process and its use in thin aluminium sheets welding. Materials & Design, 30(5), 1850-1852.

11) Prasad, N. E., Gokhale, A., & Wanhill, R. J. (Eds.). (2013). Aluminum-lithium alloys: processing, properties, and applications. Butterworth-Heinemann.

12) Ma, Y., Zhou, X., Huang, W., Liao, Y., Chen, X., Zhang, X., & Thompson, G. E. (2015). Crystallographic defects induced localised corrosion in AA2099-T8 aluminium alloy. Corrosion Engineering, Science and Technology, 50(6), 420-424.

13) De Sousa Araujo, J. V., Donatus, U., Queiroz, F. M., Terada, M., Milagre, M. X., de Alencar, M. C., & Costa, I. (2018). On the severe localized corrosion susceptibility of the AA2198-T851 alloy. Corrosion science, 133, 132-140.

14) Alexopoulos, N. D., Proiou, A., Dietzel, W., Blawert, C., Heitmann, V., Zheludkevich, M., & Kourkoulis, S. K. (2016). Mechanical properties degradation of (Al-Cu-Li) 2198 alloy due to corrosion exposure. Procedia Structural Integrity, 2, 597-603.

15) Warner, T. (2006, July). Recently-developed aluminium solutions for aerospace applications. In Materials Science Forum (Vol. 519, pp. 1271-1278). Trans Tech Publications Ltd.

16) Buchheit, R. G., Moran, J. P., & Stoner, G. E. (1994). Electrochemical behavior of the T1 (Al2CuLi) intermetallic compound and its role in localized corrosion of Al-2% Li-3% Cu alloys. Corrosion, 50(2), 120-130.

17) Prasad, N. E., Gokhale, A. A., & Rao, P. R. (2003). Mechanical behaviour of aluminium-lithium alloys. Sadhana, 28, 209-246.

18) Saha, A., & Mondal, S. C. (2015). Optimization of process parameters in submerged arc welding using multi-objectives Taguchi method. In Advances in Material Forming and Joining: 5th International and 26th All India Manufacturing Technology, Design and Research Conference, AIMTDR 2014 (pp. 221-232). Springer India.

19) Yang, S., Zhang, J., Lian, J., & Lei, Y. (2013). Welding of aluminum alloy to zinc coated steel by cold metal transfer. Materials & Design, 49, 602-612.

20) Kang, M., & Kim, C. (2015). Joining Al 5052 alloy to aluminized steel sheet using cold metal transfer process. Materials & Design, 81, 95-103.

21) Cao, R., Yu, G., Chen, J. H., & Wang, P. C. (2013). Cold metal transfer joining aluminum alloys-to-galvanized mild steel. Journal of materials processing technology, 213(10), 1753-1763.

22) Babu, S., Panigrahi, S. K., Ram, G. J., Venkitakrishnan, P. V., & Kumar, R. S. (2019). Cold metal transfer welding of aluminium alloy AA 2219 to austenitic stainless steel AISI 321. Journal of Materials Processing Technology, 266, 155-164.

23) Lin, J., Ma, N., Lei, Y., & Murakawa, H. (2013). Shear strength of CMT brazed lap joints between aluminum and zinc-coated steel. Journal of materials processing technology, 213(8), 1303-1310.

24) Wang, P., Hu, S. S., Shen, J. Q., & Liang, Y. (2017). Microstructure and mechanical behaviour of cold metal transfer welded Mg/Al dissimilar joint using wire AZ31 as filler metal. Science and Technology of Welding and Joining, 22(4), 353-361.

25) Shang, J., Wang, K., Zhou, Q., Zhang, D., Huang, J., & Li, G. (2012). Microstructure characteristics and mechanical properties of cold metal transfer welding Mg/Al dissimilar metals. Materials & Design, 34, 559-565.

26) Madhavan, S., Kamaraj, M., Vijayaraghavan, L., & Srinivasa Rao, K. (2017). Cold metal transfer welding of dissimilar A6061 aluminium alloy-AZ31B magnesium alloy: effect of heat input on microstructure, residual stress and corrosion behavior. Transactions of the Indian Institute of Metals, 70, 1047-1054.

27) Cao, R., Wen, B. F., Chen, J. H., & Wang, P. C. (2013). Cold metal transfer joining of magnesium AZ31B-to-aluminum A6061-T6. Materials Science and Engineering: A, 560, 256-266.

28) Jing, S., Kehong, W., Qi, Z., Deku, Z., Jun, H., & Guangle, L. (2013). Microstructure characteristics and properties of Mg/Al dissimilar metals made by cold metal transfer welding with ER4043 filler metal. Rare Metal Materials and Engineering, 42(7), 1337-1341.

29) He, H., Liu, Z., Zhang, L., Zhao, W., Fu, A., & Yi, X. (2023). Dissimilar CMT joining of aluminum to Ti–Ni–Hfs shape memory alloy with Al–Si filler. Journal of Materials Research and Technology, 24, 8635-8643.

30) Sun, Q. J., Li, J. Z., Liu, Y. B., Li, B. P., Xu, P. W., & Feng, J. C. (2017). Microstructural characterization and mechanical properties of Al/Ti joint welded by CMT method—assisted hybrid magnetic field. Materials & Design, 116, 316-324.

31) Cao, R., Wang, T., Wang, C., Feng, Z., Lin, Q., & Chen, J. H. (2014). Cold metal transfer welding–brazing of pure titanium TA2 to magnesium alloy AZ31B. Journal of alloys and compounds, 605, 12-20.

32) Li, J., Sun, Q., Liu, Y., Cai, C., & Feng, J. (2017). Cold Metal Transfer Welding–Brazing of Pure Titanium TA2 to Aluminum Alloy 6061-T6. Advanced Engineering Materials, 19(2), 1600494.

33) Liu, X., Frankel, G. S., Zoofan, B., & Rokhlin, S. I. (2007). In-situ observation of intergranular stress corrosion cracking in AA2024-T3 under constant load conditions. Corrosion Science, 49(1), 139-148.

34) Selvamani, S. T. (2021). Microstructure and stress corrosion behaviour of CMT welded AA6061 T-6 aluminium alloy joints. Journal of Materials Research and Technology, 15, 315-326.

35) Dutra, J. C., e Silva, R. H. G., Savi, B. M., Marques, C., & Alarcon, O. E. (2015). Metallurgical characterization of the 5083H116 aluminum alloy welded with the cold metal transfer process and two different wire-electrodes (5183 and 5087). Welding in the World, 59, 797-807.

36) Irizalp, A. O., Durmuş, H., Yuksel, N., & Turkmen, I. (2016). Cold metal transfer welding of AA1050 aluminum thin sheets. Materia (Rio de Janeiro), 21, 615-622.

37) Huang, L., Chen, X., Konovalov, S., Wang, M., Su, C., Han, L., & Wang, Y. (2022). Modeling and optimization of solidification cracking of 4043 aluminum alloys produced by cold metal transfer welding. Journal of Materials Engineering and Performance, 31(6), 4746-4760.

38) Pinto, H., Pyzalla, A., Hackl, H., & Bruckner, J. (2006, September). A comparative study of microstructure and residual stresses of CMT-, MIG- and laser-hybrid welds. In Materials science forum (Vol. 524, pp. 627-632). Trans Tech Publications Ltd.

39) Wilhelm, G., Gott, G., Schopp, H., & Uhrlandt, D. (2010). Study of the welding gas influence on a controlled short-arc GMAW process by optical emission spectroscopy. Journal of Physics D: Applied Physics, 43(43), 434004.

40) Babu, N., Karunakaran, N., & Balasubramanian, V. (2017). A study to estimate the tensile strength of friction stir welded AA 5059 aluminium alloy joints. The International Journal of Advanced Manufacturing Technology, 93, 1-9.

41) Dutra, J. C., e Silva, R. H. G., Savi, B. M., Marques, C., & Alarcon, O. E. (2015). Metallurgical characterization of the 5083H116 aluminum alloy welded with the cold metal transfer process and two different wire-electrodes (5183 and 5087). Welding in the World, 59, 797-807.

42) Cornacchia, G., Cecchel, S., Tocci, M., & Mazzu, A. (2020). Metal Inert Gas (MIG)–Cold Metal Transfer (CMT) and Fiber Laser–MIG Hybrid Welds for 6005A T6: Experimental and Numerical Comparison. Metallography, Microstructure, and Analysis, 9, 511-528.

43) Afolalu, S. A., Ohwofa, A. O., Ongbali, S. O., Ajayi, O. O., & Abioye, A. A. (2019, November). Microstructural and Mechanical Properties of Welded Joints in TIG, MIG and Friction Stir Welding–Review. In IOP Conference Series: Materials Science and Engineering (Vol. 640, No. 1, p. 012068). IOP Publishing.

44) Yin, L., Wang, J., Hu, H., Han, S., & Zhang, Y. (2019). Prediction of weld formation in 5083 aluminum alloy by twin-wire CMT welding based on deep learning. Welding in the World, 63, 947-955.

45) Cornacchia, G., & Cecchel, S. (2020). Study and characterization of EN AW 6181/6082-T6 and EN AC 42100-T6 aluminum alloy welding of structural applications: Metal inert gas (MIG), cold metal transfer (CMT), and fiber laser-MIG hybrid comparison. Metals, 10(4), 441.

46) Huan, P. C., Wang, X. N., Zhang, J., Hu, Z. R., Chen, W. G., Nagaumi, H., & Di, H. S. (2020). Effect of wire composition on microstructure and properties of 6063 aluminium alloy hybrid synchronous pulse CMT welded joints. *Materials Science and Engineering: A*, *790*, 139713.

47) Pramod, R., Shanmugam, N. S., & Krishnadasan, C. K. (2020). Studies on cold metal transfer welding of aluminium alloy 6061-T6 using ER 4043. Proceedings of the Institution of Mechanical Engineers, Part L: Journal of Materials: Design and Applications, 234(7), 924-937.

48) Gungor, B., Kaluc, E., Taban, E., & Aydin, S. I. K. (2014). Mechanical and microstructural properties of robotic Cold Metal Transfer (CMT) welded 5083-H111 and 6082-T651 aluminum alloys. Materials & Design (1980-2015), 54, 207-211.

49) Chen, H., Tianli, Z., Zhu, Z., Xu, L., Lin, S., Yang, S., & Kou, S. (2024). Study on the effect of Ar–He shielding gas on the weld formation, microstructure and mechanical properties of 5083 aluminum alloy weld. Journal of Materials Research and Technology, 28, 683-694.

50) Xie, C., Yang, S., Liu, H., Zhang, Q., Wang, Y., & Zou, Y. (2018). Microstructure and mechanical properties of robot cold metal transfer Al5. 5Zn2. 5Mg2. 2Cu aluminium alloy joints. Journal of Materials Processing Technology, 255, 507-515.

51) Girinath, B., Shanmugam, N. S., & Sathiyanarayanan, C. (2020). Studies on influence of torch orientation on microstructure, mechanical properties and formability of AA5052 CMT welded blanks. Archives of Civil and Mechanical Engineering, 20, 1-22.

52) Comez, N., & Durmuş, H. (2020). Corrosion behavior and mechanical properties of cold metal transfer welded dissimilar AA7075-AA5754 alloys. Journal of Central South University, 27(1), 18-26.

53) Selvamani, S. T. (2021). Microstructure and stress corrosion behaviour of CMT welded AA6061 T-6 aluminium alloy joints. Journal of Materials Research and Technology, 15, 315-326.

54) Chen, C., Sun, G., Zhao, Y., Chen, F., Zhang, H., & Liu, J. (2022). Microstructure and mechanical properties of 2A12 aluminum alloy welded joint through CMT double side welding. CIRP Journal of Manufacturing Science and Technology, 37, 258-266.

55) Wang, Q. T., Wang, X. N., Chen, X. M., Huan, P. C., Dong, Q. P., Zhang, Q. Y., & Nagaumi, H. (2022). Interactive effects of porosity and microstructure on strength of 6063 aluminum alloy CMT MIX+ Synchropulse welded joint. Transactions of Nonferrous Metals Society of China, 32(3), 801-811.

56) Shanker, H., & Wattal, R. (2023). Comparative study of microstructural and mechanical properties of robotic CMT and GMAW welded 7475-T7351 aluminium alloy joints. Materials Today Communications, 37, 106994.

57) Nagasai, B. P., Ramaswamy, A., Malarvizhi, S., Balasubramanian, V., & Dwivedy, M. (2024). Optimization of Process Parameters of Cold Metal Transfer Arc Welding of AA 6061 Aluminium Alloy-AZ31B Magnesium Alloy Dissimilar Joints Using Response Surface Methodology. International Journal of Lightweight Materials and Manufacture.

58) Tian, Y., Shen, J., Hu, S., Wang, Z., & Gou, J. (2018). Effects of ultrasonic vibration in the CMT process on welded joints of Al alloy. Journal of Materials Processing Technology, 259, 282-291.

59) Fattahi, M., Ghaheri, A., Arabian, N., Amirkhanlu, F., & Moayedi, H. (2020). Applying the ultrasonic vibration during TIG welding as a promising approach for the development of nanoparticle dispersion strengthened aluminum weldments. Journal of Materials Processing Technology, 282, 116672.

60) Kumar, S., Wu, C. S., Padhy, G. K., & Ding, W. (2017). Application of ultrasonic vibrations in welding and metal processing: A status review. Journal of manufacturing processes, 26, 295-322.

61) Chen, Q. H., Lin, S. B., Yang, C. L., Fan, C. L., & Ge, H. L. (2016). Effect of ultrasound on heterogeneous nucleation in TIG welding of Al–Li alloy. Acta Metallurgica Sinica (English Letters), 29, 1081-1088.

62) Meena, R. P., Yuvaraj, N., & Vipin, V. (2024). Investigations and Optimization of Cold Metal Transfer-based WAAM Process Parameters for Fabrication of Inconel 718 Samples using Response Surface Methodology. Arabian Journal for Science and Engineering, 1-15.

63) Koli, Y., Yuvaraj, N., Aravindan, S., & Vipin. (2021). Enhancement of mechanical properties of 6061/6082 dissimilar aluminium alloys through ultrasonic-assisted cold

metal transfer welding. Arabian Journal for Science and Engineering, 46(12), 12089-12104.

64) Wang, S., Dong, P., Chai, F., Gao, L., Zhang, S., & Zhang, C. (2024). Microstructure and Mechanical Properties Ultrasonic Assistance Laser Welded Joints of Beta Titanium Alloy with Multiple Vibrators. Metals, 14(4), 422.

65) Xia, Y., Dong, B., Cai, X., & Lin, S. (2024). Ultrasonic vibration assisted gas tungsten arc welding of Inconel 690 alloy: Ultrasonic effect to refine grains and improve mechanical properties. Ultrasonics Sonochemistry, 106950.

66) Guo, J., Wang, J., Cheng, L., Duan, Y., & Zhan, X. (2024). Unravelling the mechanism of columnar-to-equiaxed transition and grain refinement in ultrasonic vibration assisted laser welding of Ti6Al4V titanium alloy. Ultrasonics, 141, 107342.

67) Zhang, G., Gao, J., & Wu, C. (2023). Revealing the acoustic effects on heat transfer and material flow in ultrasonic assisted friction stir welding of dissimilar Al/Mg alloys. Journal of Materials Research and Technology, 26, 1882-1902.

68) Xiang, D. A. I., Lei, S. H. I., TIAN, C. Y., WU, C. S., & Song, G. A. O. (2024). Effect of ultrasonic vibration on microstructures and mechanical properties of friction stir welded 2195 Al− Li alloy. Transactions of Nonferrous Metals Society of China, 34(1), 80-93.

69) Chen, D. et al. (2021). Effect of porosity morphology and elements characteristics on mechanical property in T-joints during dual laser-beam bilateral synchronous welding of 2060/2099 Al-Li alloys. Optics & Laser Technology, 140, 107019.

70) Chen, X. et al. (2019). Nano-indentation and in-situ investigations of double-sided laser beam welded 2060-T8/2099-T83 Al-Li alloys T-joints. Materials Science and Engineering: A, 756, 291-301.

71) Han, B. et al. (2017). Microstructural evolution and interfacial crack corrosion behavior of double-sided laser beam welded 2060/2099 Al-Li alloys T-joints. Materials & Design, 135, 353-365.

72) Zhao, G., Wang, Z., Hu, S., Duan, S., & Chen, Y. (2020). Effect of ultrasonic vibration of molten pool on microstructure and mechanical properties of Ti-6Al-4V joints prepared via CMT+ P welding. Journal of Manufacturing Processes, 52, 193-202.

73) Ilman, M. N., Widodo, A., & Triwibowo, N. A. (2022). Metallurgical, mechanical and corrosion characteristics of vibration assisted gas metal arc AA6061-T6 welded joints. Journal of Advanced Joining Processes, 6, 100129.

74) He, Y., Cong, M., Lei, W., Ding, Y., Xv, T., & Han, Z. (2023). Microstructure, mechanical and corrosion properties of FeCrNiCoMnSi0. 1 high-entropy alloy coating via TIG arc melting technology and high-frequency ultrasonic impact with welding. Materials Today Advances, 20, 100443.

75) Kuang, X., Qi, B., & Zheng, H. (2022). Effect of pulse mode and frequency on microstructure and properties of 2219 aluminum alloy by ultrahigh-frequency pulse Metal-Inert Gas Welding. Journal of Materials Research and Technology, 20, 3391-3407.

76) Little, R.L., (1994). Welding and welding technology. Tata McGraw Hill, 198-242.

77) Lee, H., Ji, C., & Yu, J. (2018). Effects of welding current and torch position parameters on bead geometry in cold metal transfer welding. Journal of Mechanical Science and Technology, 32, 4335-4343.

78) He, S., Yang, D., Huang, Y., & Wang, K. (2022). Effect of the current waveform on the droplet transfer in CMT welding high-nitrogen steel. Journal of Manufacturing Processes, 75, 41-48.

79) Rohe, M., Knester, M., Hildebrand, J., & Bergmann, J. P. (2024). Development of an indirect measurement method for the Contact Tube to Workpiece Distance (CTDW) in the Direct Energy Deposition–Arc (DED-ARC) process for different arc types. Journal of Advanced Joining Processes, 9, 100228.

80) Reddy, A. C., Gokul, K., Mahesh, P., Reddy, G. S., & Surcsh, C. R. (1998). Effect of shielding gases on the performance of weld bead in MIG welding. Modern trends in manufacturing technology, 273.

81) John, M., Kumar, P. A., & Bhat, K. U. (2021). Effect of wire feed rate on microstructure development during bead on plate welding of microalloyed steel using P-GMAW. Materials Today: Proceedings, 42, 423-428.

82) Diakoulaki, D., Mavrotas, G. and Papayannakis, L. (1995). Determining objective weights in multiple criteria problems: The critic method. Computers & Operations Research, Vol. 22, No. 7, pp. 763–770.

83) Mukhametzyanov, I. (2021). Specific character of objective methods for determining weights of criteria in MCDM problems: Entropy, CRITIC and SD. Decision Making. Applications in Management and Engineering, Vol. 4, No. 2, pp. 76–105.

84) Madic, M. and Radovanovic, M. (2015). Ranking of some most commonly used nontraditional machining processes using ROV and CRITIC methods. UPB Sci. Bull. Series D, Vol. 77, No. 2, pp. 193–204.

85) Yakowitz, D. S., Lane, L.J. and Szidarovszky, F. (1993). Multi-attribute decision making: dominance with respect to an importance order of the attributes. Applied Mathematics and Computation, Vol. 54, No.2-3, pp.167- 181.

86) Milos M. et al. (2015). Multi-objective optimization of laser cutting using ROV- based Taguchi Methodology. Applied Mechanics and Materials, Vol. 809-810, pp. 405-410.

87) Hajkowicz, S., and Higgins, A. (2008). A comparison of multiple criteria analysis techniques for water resource management. European Journal of Operational Research, Vol. 184, No. 1, pp. 255-265.

88) Athawale, V.M., and Chakraborty, S. (2011). A comparative study on the ranking performance of some multicriteria decision-making methods for industrial robot selection. International Journal of Industrial Engineering Computations, Vol. 2, No. 4, pp. 831-850.

89) Koli, Y., et al. (2019). Investigations on weld bead geometry and microstructure in CMT, MIG, pulse synergic and MIG welding of AA6061-T6. Materials Research Express, Vol. 6, No. 12, pp. 1-25.

90) Han, L., et al. (2021). Influence of heat input on microstructure, hardness and pitting corrosion of weld metal in duplex stainless steel welded by keyhole-TIG. Materials Characterization, Vol. 175, pp. 111052.

91) Yang, S., et al. (2013). Welding of aluminum alloy to zinc coated steel by cold metal transfer. Materials & Design, Vol. 49, pp. 602-612.

92) Selvamani, S., et al. (2022). Investigation of heat input effects on the joint characteristics of CMT welded AA6061 sheets. Proceedings of the Institution of Mechanical Engineers, Part C: Journal of Mechanical Engineering Science. doi:10.1177/09544062221138839.

93) Koilraj, M., et al. (2012). Friction stir welding of dissimilar aluminum alloys AA2219 to AA5083—Optimization of process parameters using Taguchi technique. Materials and Design, Vol. 42, pp. 1–7.

94) Anyalebechi, P. N. (1995). Analysis of the effects of alloying elements on hydrogen solubility in liquid aluminum alloys. Scripta metallurgica et materialia, 33(8), 1209-1216.

95) Escribano-García, R., Rodriguez, N., Zubiri, O., Piccini, J., & Setien, I. (2022). 3D numerical simulation of GMAW Cold Metal Transfer using response surface methodology. Journal of Manufacturing Processes, 76, 656-665.

96) De Paula, N. O., dos Santos, M., Gomes, C. F., & Baldini, F. (2022). CRITIC-MOORA-3N Application on a Selection of AHTS Ships for Offshore Operations. Procedia Computer Science, 214, 187-194.

97) Akram, M. et al. (2024). Enhanced CRITIC-REGIME method for decision making based on Pythagorean fuzzy rough number. Expert Systems with Applications, Vol. 238, Part D, 122014.

98) Kumari, A. and Acherjee, B. (2022). Selection of non-conventional machining process using CRITIC-CODAS method. Materials Today: Proceedings, Vol. 56, pp. 66-71.

99) Khan, S.A. et al. (2022). Numerical investigation and implementation of the Taguchi based entropy-ROV method for optimization of the operating and geometrical parameters during natural convection of hybrid nanofluid in annuli. International Journal of Thermal Sciences, Vol. 172, pp. 107317.

100) Khan, S. A. et al. (2023). CFD simulation and optimization of natural convection in a vertical annulus with nanofluids. International Journal of Thermal Sciences, 185, 108079, pp. 1-18.

101) Lee, J. S., Chun, W., Roh, K., Heo, S., & Lee, J. H. (2023). Applying real options with reinforcement learning to assess commercial CCU deployment. Journal of CO2 Utilization, 77, 102613.

102) Prajapati, V. et al. (2020). Study of parametric influence and welding performance optimization during regulated metal deposition (RMD™) using grey integrated with fuzzy Taguchi approach. Journal of Manufacturing Processes, Vol. 54, pp. 286-300.

103) Vinoth, V. et al. (2021). Optimization of mechanical behaviour of TIG welded 316 stainless steel using Taguchi based grey relational analysis method. Materials Today: Proceedings, Vol. 45, pp. 7986-7993.

104) Saeheaw, T. (2022). Application of integrated CRITIC and GRA-based Taguchi method for multiple quality characteristics optimization in laser-welded blanks. Heliyon, Vol. 8 No. 11, pp. e11349.

105) Kumaran, V.V.A. et al. (2020). Development of Pulsed Cold Metal Transfer and Gas Metal Arc Welding Techniques on High-Strength Aerospace-Grade AA7475-T761. Journal of Materials Engineering and Performance, Vol. 29, pp. 7270-7290.

106) Xiang, H. et al. (2023). Influence of Metal Transfer Modes on Pore Formation during the Welding Process of AA6082/A360 Dissimilar Aluminum Alloys. Journal of Materials Engineering and Performance, https://doi.org/10.1007/s11665-022-07757-6.

107) Nalajala, D., Mookara, R.K. and Amirthalingam, M. (2022). Analysis of Metal Transfer Characteristics in Low-Heat Input Gas Metal Arc Welding of Aluminum Using Aluminum–Silicon Alloy Fillers, Metallurgical and Materials Transactions B, Vol. 53 No. 5, pp. 2914-2924.

108) Agrawal, T., Gautam, R., Agrawal, S., Singh, V., Kumar, M., & Kumar, S. (2020). Optimization of engine performance parameters and exhaust emissions in compression ignition engine fueled with biodiesel-alcohol blends using Taguchi method, multiple regression, and artificial neural network. Sustainable Futures, 2, 100039.

109) Ghosh, N., Pal, P. K., & Nandi, G. (2016). Parametric optimization of MIG welding on 316L austenitic stainless steel by grey-based Taguchi method. Procedia Technology, 25, 1038-1048.

110) Koli, Y., Yuvaraj, N., Aravindan, S., & Vipin. (2021). CMT joining of AA6061-T6 and AA6082-T6 and examining mechanical properties and microstructural characterization. Transactions of the Indian Institute of Metals, 74, 313-329.

111) Nagasai, B. P., Ramaswamy, A., & Mani, J. (2023). Tensile properties and microstructure of surface tension transfer (STT) arc welded AA 6061-T6 aluminum alloy joints. Materials Today: Proceedings.

112) Roy, J. G., Yuvaraj, N., & Vipin. (2021). Effect of Welding Parameters on Mechanical Properties of Cold Metal Transfer Welded Thin AISI 304 Stainless-Steel Sheets. Transactions of the Indian Institute of Metals, 74, 2397-2408.

113) Cai, H., Xu, L., Zhao, L., Han, Y., Pang, H., & Chen, W. (2022). Cold metal transfer plus pulse (CMT+ P) welding of G115 steel: Mechanisms, microstructure, and mechanical properties. Materials Science and Engineering: A, 843, 143156.

114) Goebel, J., Ghidini, T., & Graham, A. J. (2016). Stress-corrosion cracking characterisation of the advanced aerospace Al–Li 2099-T86 alloy. Materials Science and Engineering: A, 673, 16-23.

115) Abd El-Aty, A., Guo, X., Lee, M. G., Tao, J., Hou, Y., Hu, S.... & Yang, Q. (2023). A review on flexibility of free bending forming technology for manufacturing thin-walled complex-shaped metallic tubes. International Journal of Lightweight Materials and Manufacture, 6(2), 165-188.

116) Hou, Y., Myung, D., Park, J. K., Min, J., Lee, H. R., El-Aty, A. A., & Lee, M. G. (2023). A review of characterization and modelling approaches for sheet metal forming of lightweight metallic materials. Materials, 16(2), 836.

117) Singh, S., Yuvaraj, N., & Wattal, R. (2024). Measurement of Mechanical Properties of Friction Stir Welding of Al–Li alloy under different environmental conditions. MAPAN, 1-10.

118) Hwang, L. R., Gung, C. H., & Shih, T. S. (2001). A study on the qualities of GTA-welded squeeze-cast A356 alloy. Journal of Materials Processing Technology, 116(2-3), 101-113.

119) Singh, S., Yuvaraj, N., & Wattal, R. (2024). Multicriteria decision-making for optimization of welding parameters in cold metal transfer and pulse metal-inert gas weld bead of AA2099-T86 alloy using CRITIC and ROV methods. Multidiscipline Modeling in Materials and Structures.

120) Dai, W. L. (2003). Effects of high-intensity ultrasonic-wave emission on the weldability of aluminum alloy 7075-T6. Materials Letters, 57(16-17), 2447-2454.

121) Du, C., Wang, X., Pan, Q., Xue, K., Ni, M., & Liu, J. (2019). Correlation between microstructure and mechanical properties of 6061-T6 double-side FSW joint. Journal of Manufacturing Processes, 38, 122-134.

122) Ji, H., Deng, Y., Xu, H., Lin, S., Wang, W., & Dong, H. (2020). The mechanism of rotational and non-rotational shoulder affecting the microstructure and mechanical properties of Al-Mg-Si alloy friction stir welded joint. Materials & Design, 192, 108729.

123) Sastry, C. C., Hariharan, P., Pradeep Kumar, M., & Muthu Manickam, M. A. (2019). Experimental investigation on boring of HSLA ASTM A36 steel under dry, wet, and cryogenic environments. Materials and Manufacturing Processes, 34(12), 1352-1379.

124) Reza-E-Rabby, M., Olszta, M. J., Overman, N. R., McDonnell, M., & Whalen, S. A. (2021). Frictions stir dovetailing of AA7099 to steel with AA6061 interlayer for reduced Zn embrittlement at dissimilar interface. Journal of Manufacturing Processes, 61, 25-34.

125) Urminsky, J., Maronek, M., Barta, J., Sahul, M., Jurina, F., & Pasak, M. (2020). Electron beam welding of aluminium alloy AW2099. In Materials Science Forum (Vol. 994, pp. 28-35). Trans Tech Publications Ltd.

126) Liu, X. C., Li, W. T., Zhou, Y. Q., Li, Y. Z., Pei, X. J., Shen, Z. K., & Wang, Q. H. (2023). Multiple effects of forced cooling on joint quality in coolant-assisted friction stir welding. Journal of Materials Research and Technology, 25, 4264-4276.

127) Masumura, R. A., Hazzledine, P. M., & Pande, C. S. (1998). Yield stress of fine grained materials. Acta Materialia, 46(13), 4527-4534.

128) Cui, B., Chen, K., Yang, Y., Lv, Y., Zhang, F., & Liu, S. (2024). Effect of ultrasonic vibration on the pores and properties of the laser-arc hybrid welding joint of high nitrogen steel. Materials Chemistry and Physics, 318, 129297.

129) Yang, Q., Dong, Z., Kang, R., & Wei, Z. (2024). Effect of ultrasonic vibration and deep cryogenic treatment on the residual stress, mechanical properties, and microstructures of HR-2 austenitic stainless steel. Materials Science and Engineering: A, 900, 146502.

LIST OF PUBLICATIONS

➢ **List of papers published in SCI/SCIE journals**

- Satyaveer Singh, N. Yuvaraj, Reeta Wattal (2024). Multicriteria decision-making for optimization of welding parameters in cold metal transfer and pulse metal-inert gas weld bead of AA2099-T86 alloy using CRITIC and ROV methods. Multidiscipline Modeling in Materials and Structures, 20(3), 466-485. **(Impact factor-1.7)**

  DOI- https://doi.org/10.1108/MMMS-07-2023-0250

- Satyaveer Singh, N. Yuvaraj, Reeta Wattal (2024). Measurement of Mechanical Properties of welding of Al–Li alloy under different environmental conditions. MAPAN, 1-10. **(Impact factor-1.0)**

  DOI: https://doi.org/10.1007/s12647-024-00736-3

➢ **List of papers published in International Conferences**

- Satyaveer Singh, "Comparative study on mechanical properties of CMT and MIG-Pulse welded 2099-T86 aluminum alloy sheet", International Conference of Advance Research and Innovation. ICARI, ISSN 2347-3258.
- Satyaveer Singh, "Investigation on the effect of ultrasonic vibration on the joint quality of CMT welded AA2099-T86 alloy", International Conference of Advance Research and Innovation. ICARI, ISSN 2347-3258

CURRICULUM VITAE

Mr. Satyaveer Singh has obtained his Bachelor's Degree (B.E) in Mechanical engineering (2006-2010) and Master's Degree (M.Tech) in Production & Industrial engineering (2011-2013), both from Jamia Millia Islamia, New Delhi, India. His main area of research includes gas metal arc welding (GMAW), cold metal transfer welding (CMT), pulse metal-Inert gas **(**MIG) welding and optimization techniques. He has published 2 SCI/SCIE, 2 conference papers at an international level.